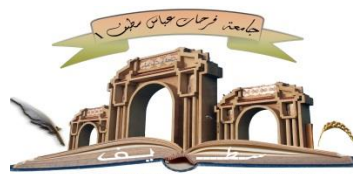


الجمهورية الجزائرية الديمقراطية

PEOPLE'S DEMOCRATIC REPUBLIC OF ALGERIA  
THE MINISTRY OF HIGHER EDUCATION AND SCIENTIFIC RESEARCH



Université Ferhat ABBAS Sétif 1  
FERHAT ABBAS UNIVERSITY – SETIF 1  
FACULTY OF TECHNOLOGY

## **THESIS**

**Presented in the Department of Electrical engineering**

**To obtain the diploma of**

## **DOCTORATE OF SCIENCES**

**Option: Electric Networks**

By

**ALTI Nadjim**

## **THEME**

# **Contribution to the study and analysis of the metal oxide surge arresters failure**

**Presented publically in: ..../...../2021 in front of the Jury:**

<b>GHERBI Ahmed</b>	Prof. at Ferhat ABBAS university of Setif 1	President
<b>BAYADI Abdelhafid</b>	Prof. at Ferhat ABBAS university of Setif 1	Supervisor
<b>HAMOU Nouri</b>	Prof. at Ferhat ABBAS university of Setif 1	Examiner
<b>MOULAI Hocine</b>	Prof.at Houari Boumediene university Algiers	Examiner
<b>MEKHALDI Abdelouahab</b>	Prof.at the National Polytechnic School, Algiers	Examiner
<b>TEGUAR Madjid</b>	Prof.at the National Polytechnic School, Algiers	Examiner

## DECLARATION

This work has not previously been accepted in substance for any degree and is not concurrently submitted in candidature for any degree.

Signed : .....  ..... (ALTI Nadjim)

Date:.....

## STATEMENT 1

This thesis is being submitted in partial fulfilment of the requirements for the degree of PhD

Signed : .....  ..... (ALTI Nadjim)

Date:.....

## STATEMENT 2

This thesis is the result of my own work/investigation, except where otherwise stated. Other sources are acknowledged by explicit references.

Signed : .....  ..... (ALTI Nadjim)

Date:.....

## STATEMENT 3

I hereby give consent for my thesis, if accepted, to be available for photocopying and for inter-library loan, and for the title and summary to be made available to outside organisations.

Signed : .....  ..... (ALTI Nadjim)

Date:.....

# PUBLICATIONS

## Journal:

**Alti N, Bayadi A, Belhouchet K.** Grading ring parameters optimization for 220 kV metal-oxide arrester using 3D-FEM method and bat algorithm. *IET Sci Meas Technol.* 2021; 15: 14–24. <https://doi.org/10.1049/smt2.12002>

**Khaled Belhouchet, Abdelhafid Bayadi, Nadjim Alti, Lyamine Ouchen.** Effects analysis of the pollution layer parameters on a high voltage porcelain cylindrical insulator using response surface methodology. *DIAGNOSTYKA.* 2021; 22(2): 21–28. <https://doi.org/10.29354/diag/134114>

## Conference:

**Nadjim. Alti,** Abdelhafid. Bayadi, “Behaviour of the Metal Oxide Surge Arrester under Pollution”. 9ème Conférence Nationale sur la Haute Tension (CNHT), 2013.

**Nadjim. Alti,** Abdelhafid. Bayadi, “Electrical performance of polluted polymeric surge arresters AC voltage”. 8ème Conférence sur le Génie Électrique (CGE'08), 2013.

**Nadjim. Alti,** Abdelhafid. Bayadi, “Behaviour of the polymeric surge arrester under pollution taking into account the presence of dry bands”. The 9th international conference on electrical engineering and first workshop on robotics and controls (CEE), 2016.

## ملخص:

يهدف الجزء الأول من هذه الرسالة إلى تحسين توزيع الجهد والمجال الكهربائي على طول مانعة الصواعق البوليميرية 220 كيلو فولط عن طريق تحسين تصميم حلقة تدرج المجال الكهربائي. تم اختيار طريقة مدمجة تعتمد على طريقة العناصر المتناهية ثلاثية الأبعاد وتصميم تاجوتشي من أجل الحصول على دالة الهدف. يتم تحقيق التصميم الأمثل لحلقة تدرج المجال الكهربائي من خلال تقليل المجال الكهربائي على طول العمود النشط للمتغيرات باستخدام عدد أقل من عمليات المحاكاة بناءً على تصميم تاجوتشي وخوارزمية الخفافيش. باستخدام التصميم الأمثل للحلقة الواحدة، يتم تقليل المجال الكهربائي بنسبة 42% في الجزء العلوي من مانعة الصواعق 220 كيلو فولط. بعد ذلك، تم اقتراح تركيب حلقة إضافية في الجزء العلوي من مانعة الصواعق من أجل الحصول على توزيع أفضل للجهد والمجال الكهربائي على طول العمود النشط. هذه الحلقة الإضافية المقترحة لها بعد هندسي كبير مقارنة بالحلقة الأولى. تظهر نتائج المحاكاة أنه باستخدام التصميم الأمثل للحلقات المزدوجة، يمكن جعل توزيع الجهد منتظماً قدر الإمكان ويتم تقليل المجال الكهربائي بنسبة 53% لتجنب تلف المتغيرات.

يتعلق الجزء الثاني من الأطروحة بالنمذجة الكهروحرارية لموانع الصواعق أكسيد المعادن التي تسمح بالحصول على تغير درجة حرارة مانعة الصواعق المدروس. سيسمح لنا ذلك بمراقبة حالة مانعة الصواعق وكذلك تجنب فشلها.

لهذا الغرض، تم استخدام نموذج الدوائر الكهروحرارية. تم تنفيذ هذا الأخير في برنامج ATP / EMTP من أجل محاكاة درجات الحرارة الداخلية للمتغيرات ودرجات الحرارة الخارجية لغلاف مانعة الصواعق. تم الحصول على نتائج مرضية .

**الكلمات المفتاحية:** مانعة الصواعق البوليميرية، حلقة تدرج المجال الكهربائي ، المجال الكهربائي، طريقة العناصر المتناهية ثلاثية الأبعاد، تصميم تاجوتشي، خوارزمية الخفافيش، النمذجة الكهروحرارية، ATP / EMTP، درجة الحرارة.

## **Abstract**

The first part of this thesis is aimed to improve the distribution of the potential and the electric field along a 220 kV polymeric surge arrester by optimizing the design of the grading ring. A combined method based on 3D-FEM and Taguchi design is opted in order to obtain the objective function. The optimal design of grading ring is achieved by minimizing the electric field along the active column of varistors using a reduced number of simulations based on the Taguchi design and a bat algorithm. By the use of an optimal design of the single ring, the electric field is reduced by 42% in the top of the 220 kV metal oxide surge arrester. Then, it was proposed to install an additional ring at the top of the metal oxide surge arrester in order to obtain a better distribution of the potential and the electric field along the active column. This proposed additional ring has a large geometric dimension compared to the first ring. Simulation results show that using an optimal design of double rings, the potential distribution can be made as uniform as possible and the electric field is reduced by 53% to avoid failure of varistors.

The second part of the thesis concerns the electro-thermal modeling of metal oxide surge arresters which allows the temperature variation of the studied arrester. This would allow us to monitor the condition of the surge arrester as well as to avoid its failure.

For this purpose, a circuit electro-thermal model was used. This latter has been implemented in the ATP / EMTP software in order to simulate the internal temperatures of the varistors and the external temperatures of the surge arrester housing. Satisfactory results have been obtained.

***Keywords:*** *Polymeric surge arrester, grading ring, electric field, 3D-FEM, Taguchi design, Bat algorithm, electro-thermal modeling, ATP / EMTP, temperature.*

## **Résumé**

La première partie de cette thèse vise à améliorer la distribution du potentiel et du champ électrique le long d'un parafoudre 220 kV en polymère en optimisant la conception de l'anneau de garde. Une méthode combinée basée sur 3D-FEM et la conception de Taguchi est choisie afin d'obtenir la fonction objective. La conception optimale de l'anneau de garde est obtenue en minimisant le champ électrique le long de la colonne active de varistances en utilisant un nombre réduit de simulations basées sur la conception de Taguchi et un algorithme de chauve-souris. Par l'utilisation d'une conception optimale de l'anneau unique, le champ électrique est réduit de 42% dans la partie supérieure du parafoudre à oxyde métallique 220 kV. Ensuite, il a été proposé d'installer un anneau supplémentaire en haut du parafoudre à oxyde métallique afin d'obtenir une meilleure distribution du potentiel et du champ électrique le long de la colonne active. Cet anneau supplémentaire proposé a une grande dimension géométrique par rapport au premier anneau. Les résultats de simulation montrent qu'en utilisant une conception optimale de doubles anneaux, la distribution du potentiel peut être rendue aussi uniforme que possible et le champ électrique est réduit de 53% pour éviter la défaillance des varistances.

La deuxième partie de la thèse concerne la modélisation électrothermique des parafoudres à oxyde métallique qui permet d'obtenir la variation de la température du parafoudre étudié. Ce qui nous permettrait de surveiller l'état du parafoudre et d'éviter sa défaillance.

À cet effet, un modèle électrothermique de circuiterie a été adopté. Ce dernier a été implanté dans le logiciel ATP / EMTP afin de simuler les températures internes des varistances et les températures externes de l'enveloppe du parafoudre. Des résultats satisfaisants ont été obtenus.

**Mots clés:** *Parafoudre en polymère, anneau de garde, champ électrique, 3D-FEM, conception de Taguchi, algorithme de Bat, modélisation électrothermique, ATP / EMTP, température.*

## *Dedications*

---

---

*This thesis is dedicated*

*To...*

*My dear parents, may god have mercy on them.*

*My brothers and sisters*

*My wife*

*My little princess "LYNA"*

*My little prince "IYAD"*

*&*

*All my friends and work colleagues*

*ALTI.NADJIM (Issam)*

## *Acknowledgements*

---

---

*First and foremost, I thank Almighty God for giving me the strength, courage and will to do this work.*

*Firstly, I am grateful to the ALLAH for the good health and wellbeing that were necessary to complete this thesis.*

*I am so grateful to Prof. A. BAYADI for giving me the opportunity to carry out this research. His expert advice and continuous support have been a permanent source of great help.*

*My sincere thanks also go to Pr. GHERBI Ahmed, for honoring my jury by presiding it.*

*I would like to extend my gratitude also to;*

*Pr. HAMOU Nouri, Pr. MOULAI Hocine, Pr. MEKHALDI Abdelouahab and Pr. TEGUAR Madjid who kindly accepted to participate in the defense of this thesis as examiners.*

*I thank all who in one way or another contributed to the completion of this thesis*

*Finally, I must express my very profound gratitude to my family, and in particular to my parents may God have mercy on them, my wife and to my little princess "Lyna" for providing me with unfailing support and continuous encouragement throughout my years of study and through the process of researching and writing this thesis. This accomplishment would not have been possible without them.*

*Thank you.*

*ALTI NADJIM*

---

## *Table of contents*

---

<b>Chapter 01</b> .....	1
<b>GENERAL INTRODUCTION</b> .....	1
1.1. Background .....	1
1.2. Problem statement .....	2
1.3. Objectives .....	3
1.4. Contributions of the present work .....	4
1.5. Thesis Organization .....	5
<b>Chapter 02</b> .....	8
<b>SURGE ARRESTERS: A LITERATURE REVIEW</b> .....	8
2.1. Introduction .....	8
2.2. Metal oxide surge arrester .....	8
2.2.1. Internal parts of a surge arrester .....	10
2.2.2. Surge arrester housing .....	11
2.3. Functional principle of metal oxide surge arresters .....	17
2.4. Advantage of polymeric surge arrester .....	17
2.5. Characteristic parameters of metal oxide surge arresters .....	17
2.6. Main criteria for dimensioning a surge arrester .....	18
2.7. Surge Arrester failures .....	19
2.7.1. Sealing problems and internal humidity .....	19
2.7.2. Degradation and destruction of varistors .....	19
2.7.3. Varistors displacement .....	21
2.7.4. Superficial pollution .....	21
2.7.5. Irregular voltage distribution .....	23
2.8. Surge arresters condition monitoring methods .....	24
2.8.1. Leakage current measurement .....	25

---

---

2.8.2. Electromagnetic field measurement.....	27
2.8.3. V–I characteristic curve analysis .....	28
2.8.4. Thermo-vision.....	29
2.9. Conclusion .....	30
<b>Chapter 03</b> .....	<b>32</b>
<b>THERMAL BEHAVIOUR OF METAL OXIDE SURGE ARRESTERS</b> .....	<b>32</b>
3.1. Introduction.....	32
3.2. Thermal stability of metal oxide surge arrester .....	32
3.2.1. Thermal runaway critical condition .....	35
3.2.2. Heat dissipation capability of the housing .....	35
3.3. Heat transfer.....	36
3.3.1. Conduction .....	36
3.3.2. Convection .....	37
3.3.3. Radiation .....	38
3.4. Modeling of the thermal behavior of metal oxide surge arresters.....	38
3.5. Conclusion .....	53
<b>Chapter 04</b> .....	<b>55</b>
<b>GRADING RING DESIGN OPTIMIZATION FOR IMPROVED ELECTRIC FIELD DISTRIBUTION</b> .....	<b>55</b>
4.1. Introduction.....	55
4.2. Grading ring application .....	55
4.3. Modeling detail of the MOSA .....	57
4.3.1. Effects of air box size and mesh type on the electric field distribution.....	61
4.4. Taguchi design.....	61
4.5. BAT ALGORITHM .....	63
4.5.1. Movement of Virtual Bats .....	64
4.5.2. Loudness and pulse emission.....	65

---

---

4.6. Optimization process steps .....	68
4.7. Results and discussion .....	70
4.7.1. FEM Simulation without grading ring .....	70
4.7.2. FEM Simulation with Grading Ring .....	71
4.7.3. Optimization of the Grading Rings Parameters Based On BAT Algorithm .....	73
4.7.4. Additional grading ring installation .....	78
4.8. Conclusion .....	82
<b>Chapter 05</b> .....	85
<b>ELECTROTHERMAL MODELING OF THE METAL OXIDE SURGE ARRESTER</b> .....	85
5.1. Introduction.....	85
5.2. Electro-thermal model of metal oxide arrester .....	85
5.3. Determination of thermal parameters of electro-thermal model .....	86
5.3.1. Thermal resistances by conduction .....	87
5.3.2. Thermal resistances by radiation .....	88
5.3.3. Thermal resistances by convection .....	89
5.3.4. Thermal capacities of metal oxide surge arrester Components .....	91
5.3.5. Heat loss from varistors elements .....	92
5.4. Simulation results .....	93
5.4.1. Validation of the electro-thermal model .....	94
5.4.2. Study of the temperature variation of the surge arrester.....	94
5.4.3. Effect of applied voltage on temperature.....	97
5.4.4. Effect of applied voltage on power loss.....	98
5.4.5. Effect of ambient temperature on the varistors temperature variation .....	99
5.5. Conclusion .....	100
<b>Chapter 06</b> .....	102
<b>GENERAL CONCLUSIONS</b> .....	102
6.1 .Conclusions.....	102
6.2. Recommendations.....	104

---

---

## *List of figures*

---

Figure 2.1 Structure of metal surge arresters: (a) porcelain housing; (b) polymer housing....	9
Figure 2.2 Cross section of the unit of a porcelain housing MO arrester [28] .....	12
Figure 2.3 Tube design for polymer surge arrester [32] .....	13
Figure 2.4 Cage design for polymer surge arrester [32] .....	14
Figure 2.5 Wrap design for polymer surge arrester [32] .....	15
Figure 2.6 Design of GIS arresters for different systems voltages: Left: single phase design for system voltage up to 170 kV. Middle: Three phase design up to 170 kV. Right: single phase design for system voltages above 170 kV with electrical one phase, but mechanically three columns of MO varistors, courtesy Siemens [31]. .....	16
Figure 2.7 Measuring leakage current through an arrester [59]. .....	25
Figure 2.8 Circuit for measurement of total leakage current of a surge arrester [60] .....	26
Figure 2.9 Measurement setup of PD [52] .....	28
Figure 2.10 V-I characteristic of aged and new varistors [45]. .....	29
Figure 3.1 Temperature dependence of ZnO voltage-current characteristic [1] .....	33
Figure 3.2 Diagram of the thermal stability of a MOSA [20] .....	34
Figure 3.3 Electrical analog circuit for the thermal parameters of MOSA [68].....	39
Figure 3.4 Electrothermal model of a MOSA [75].....	41
Figure 3.5 Electrothermal model developed by M.V Lat [76] .....	43
Figure 3.6 Generic electro-thermal modeling procedure for MOV [77].....	45
Figure 3.7 Temperature dependency of ZnO thermal conductivity and thermal resistance [77] .....	46
Figure 3.8 Temperature dependency of ZnO specific heat and thermal capacitance [77]....	46
Figure 3.9 Diagram of the electrothermal MOSA model [67] .....	47
Figure 3.10 Conventional electric model for MOSA [67].....	48

---

---

Figure 3.11 Thermal model of MOSA [67].....	48
Figure 3.12 Modèle IEEE du parafoudre [69].....	50
Figure 3.13 Electrical analog circuit for the thermal model of MOSA [69]. ....	51
Figure 3.14 Electrical analogous circuit at steady state [66].....	52
Figure 4.1 Structure of the studied 220 kV polymeric metal oxide surge arrester.....	58
Figure 4.2 Structural parameters of grading ring .....	59
Figure 4.3 Principle of the bats echolocation behavior .....	64
Figure 4.4 Loudness A.....	66
Figure 4.5 Pulse emission rate r.....	66
Figure 4.6 Pseudo -code of Bat algorithm.....	67
Figure 4.7 Optimization process steps.....	69
Figure 4.8 E-field distribution along the central axis of the surge arrester without grading ring .....	70
Figure 4.9 Distribution of the electric potential for a surge arrester without grading ring ...	70
Figure 4.10 Maxim E-field for different H&R with T=50 mm.....	71
Figure 4.11 Maximum E-field for different T&H with R=300 mm.....	72
Figure 4.12 Maximum E-field for different R&T with H=250 mm.....	72
Figure 4.13 Convergence process of the objective function for 100 iterations.....	75
Figure 4.14 E-field distribution along the central axis of the surge arrester .....	76
Figure 4.15 Distribution of the electric potential for a surge arrester with optimized grading ring .....	77
Figure 4.16 Electric potential distribution along the central axis of the surge arrester.....	77
Figure 4.17 Studied metal oxide surge arrester with additional ring .....	78
Figure 4.18 E-field distribution along the central axis of the surge arrester .....	81

---

---

Figure 4.19 Distribution of the electric potential for a surge arrester with optimized grading rings .....	81
Figure 4.20 Electric potential distribution along the central axis of the surge arrester.....	82
Figure 5.1 Cross section and equivalent electro-thermal model of the surge arrester .....	87
Figure 5.2 V-I Characteristic curve for a 220 kV metal oxide surge arrester .....	93
Figure 5.3 Electro-thermal model of surge arrester.....	93
Figure 5.4 Temperature variation of the MOSA during heating and cooling simulation under $0.9 \cdot U_{1mA}$ applied voltage .....	95
Figure 5.5 Thermal resistances variation during simulation process. ....	96
Figure 5.6 Temperature variation of the MOSA during heating simulation under $0.9 \cdot U_{1mA}$ applied voltage, and cooling under operating voltage .....	97
Figure 5.7 Temperature variation of the varistors elements simulation under different applied voltage .....	98
Figure 5.8 Power loss variation as a function of applied voltage ratio at 20 °C .....	99
Figure 5.9 Varistors temperature at different ambient temperatures.....	100

---

***List of tables***

---

Table 4.1 Grading ring dimensions for 245 kV surge arresters.....	59
Table 4.2 Grading ring parameters .....	60
Table 4.3 Plan of Taguchi.....	62
Table 4.4 Numerically computed results for a single ring .....	74
Table 4.5 Grading ring parameters optimization for different optimization algorithm .....	76
Table 4.6 Parameters of grading rings.....	79
Table 4.7 Numerically computed results for two rings .....	79
Table 5.1 Thermal–electrical analogies .....	86
Table 5.2 Thermal resistances by conduction of metal oxide arrester components .....	88
Table 5.3 Thermal capacity of metal oxide arrester components.....	91
Table 5.4 Temperature of the studied 220 kV polymeric metal oxide surge arrester at environmental temperature of 20 °C.....	94

---

## *List of abbreviations and symbols*

---

### **Abbreviations**

<b>ATP</b>	Alternative Transients Program
<b>AC</b>	Alternating Current
<b>AFSA</b>	Artificial Fish Swarm Algorithm
<b>AutoCAD</b>	Auto Computer Aided Design software package
<b>ANN</b>	Artificial Neural Network
<b>BA</b>	Bat Algorithm
<b>E-field</b>	Electric-field
<b>EPDM</b>	Ethylene Propylene Diene Monomer
<b>EMTP</b>	Electromagnetic Transients Program
<b>FEM</b>	Finite Element Method
<b>FRP</b>	Fiber-glass Reinforced Plastic
<b>FFT</b>	Fast Fourier Transform
<b>GIS</b>	Gas-insulated substations
<b>GA</b>	Genetic Algorithm
<b>HV</b>	High Voltage
<b>IEC</b>	International Electrotechnical Commission
<b>MOSA</b>	Metal Oxide Surge Arrester
<b>MOV</b>	Metal Oxide Varistor
<b>MCOV</b>	Maximum Continuous Operating Voltage
<b>MO</b>	Metal Oxide
<b>PD</b>	Partial Discharge
<b>PSO</b>	Particle Swarm Optimisation
<b>r.m.s</b>	root mean square
<b>RSM</b>	Response Surface Methodology
<b>SiC</b>	silicon carbide
<b>SF6</b>	Sulfur hexafluoride
<b>SA</b>	Surge Arrester

<b>TNM</b>	Thermal Network Method
<b>3D</b>	Three dimensional
<b>VHF</b>	Very High Frequency
<b>ZnO</b>	Zinc oxide

## **Symbols**

<b>A</b>	Loudness
<b><math>A^t</math></b>	The average loudness of all the bats at time t
<b><math>A_1, A_2, a_1, a_2</math></b>	Constants
<b><math>a_{i0}, a_i, a_{ii}</math> and <math>a_{ij}</math></b>	Represents the input variables related to the considered parameters
<b>B</b>	depends on the applied voltage level and the physical dimensions of the valve elements
<b><math>C_d</math></b>	Heat dissipation coefficient [W/cm/°K]
<b>°C</b>	Degree Celsius
<b><math>C_E, C_H</math></b>	Thermal capacities of the valve element and adjacent housing
<b><math>C_T</math></b>	Thermal dissipation factor
<b>cm</b>	Centimeter
<b><math>C_c</math></b>	Heat capacity of any particular component
<b><math>C_o</math></b>	Specific Heat
<b><math>C_1, C_2</math></b>	Empirical constants
<b><math>C_v</math></b>	Varistor thermal capacity
<b><math>C_p</math></b>	Housing thermal capacity
<b><math>C_{th}</math></b>	Thermal capacitance of ZnO
<b><math>C_1</math> to <math>C_5</math></b>	Represent the stray capacitance of each varistor
<b><math>C_{FF}</math></b>	The capacitance between the upper and lower flanges
<b><math>C_{FUSi}</math></b>	The upper flange stray capacitances with spacers and aluminum sheets
<b><math>C_{FDSi}</math></b>	The stray capacitances among the lower flange and spacers and aluminum sheets
<b><math>C_s</math></b>	is the specific heat capacity [J/ m <sup>3</sup> .°K]

---

---

$D$	Diameter of varistors elements
$D_{max}$	Maximum housing diameter
$d$	Height of the arrester in meters
$E$	Electric field
$F$	Voltage gradient [ $V/cm^2$ ]
$f_i$	Frequency
$Gr$	Grashof number
$H$	Positions of grading ring from HV electrode
$H_1$	Small ring position from HV electrode
$H_2$	Large ring position from HV electrode
$h$	Heat transfer Coefficient [ $W/(m^2 \cdot ^\circ K)$ ]
$h_v$	Varistor element height
$I_{mr1}$	Maximum amplitude of fundamental harmonic of the resistive leakage current
$I_{mr3}$	Maximum amplitude of third harmonic of the resistive leakage current
$I_{mc1}$	Maximum amplitude of fundamental harmonic of the capacitive current
$I_n$	Nominal discharge current of an arrester
$I_j$	Represents the heat source applied to the elements
$I_r$	Represents the heating effect of the sun
$i(t)$	The instantaneous surge current pulse
$J$	Current density in [ $A/cm^2$ ]
$kV$	Kilovolt
$kA$	Kiloampere
$K_B$	Boltzmann constant ( $0.86 \cdot 10^{-4} eV/^\circ K$ )
$^\circ K$	Kelvin
$kJ$	kilojoules
$k_1, k_2$	Constants
$kHz/MHz$	Kilo/Mega Hertz

---

---

$k_{th}$	Thermal conductivity
<b>L9</b>	Taguchi design model with nine rows (or number of experiments)
$L$	The height of the sample
<b>mA</b>	Milliampere
<b>ms</b>	Millisecond
<b>m</b>	Meter
$M$	is the mass of component [Kg]
$n$	Number of parallel columns of MO disks
$Np$	Number of bats in the echolocation
$Nu$	Nusselt number
<b>NLRES92</b>	Non-linear resistance model 92 taken from the EMTP /ATP software
<b>nF</b>	Nano farad
<b>pF</b>	Pico farad
<b>P</b>	Energy generated by surge arrester
<b>p(t)</b>	Heat source
$P_{loss}$	Power losses
<b>P-V-T</b>	Power loss-Voltage-Temperature
$Pr$	Prandtl number
<b>Q</b>	Heat dispersion of the housing
$\dot{q}$	Heat flux [ $W/m^2$ ]
<b>R</b>	Grading ring radius
$R_2$	Large ring radius
$R_1$	Small ring radius
$R_{EH}$	Thermal resistance from element to external surface of the housing
$R_{HA0}$	Thermal resistance from housing to ambient, radiation and natural convection components
$R_{HAF}$	Thermal resistance from housing to ambient, forced convection component only
$r_1, r_2$	Thermal resistance between varistor element and housing
$R_{ha}$	Thermal resistance between housing and ambient

---

<b>R<sub>p</sub></b>	Housing thermal resistance
<b>R<sub>pp</sub></b>	Thermal resistance between housing and ambient
<b>R<sub>o</sub></b>	Thermal resistance from housing to ambient, due to radiation and natural convection
<b>R<sub>f</sub></b>	Thermal resistance from housing to ambient due to forced convection
<b>R<sub>1</sub> to R<sub>5</sub></b>	Represent the resistances of each varistor
<b>T<sub>HI</sub></b>	Temperature of the inner surface of the arrester housing
<b>R<sub>CHO</sub></b>	Thermal resistor between the varistor and housing
<b>R<sub>EHR</sub></b>	Radiation thermal resistance between the ZnO varistors and housing
<b>R<sub>EHCV</sub></b>	Conduction thermal resistance between the ZnO varistors and housing
<b>R<sub>HACV</sub></b>	Conduction thermal resistance between the housing and ambient
<b>R<sub>HAR</sub></b>	Radiation thermal resistance between the housing and ambient
<b>R<sub>th</sub></b>	Thermal resistance of ZnO
<b>R</b>	Emission pulse rate
<b>R<sub>cd</sub></b>	Thermal resistances by conduction [°K/W]
<b>r<sub>out</sub></b>	The outside diameter of the sample
<b>r<sub>int</sub></b>	The inside diameter of the sample
<b>R<sub>rd</sub></b>	Thermal resistances by radiation
<b>Re</b>	Reynold number
<b>R<sub>cv</sub></b>	Thermal resistances by convection
<b>S</b>	Second
<b>S<sub>p</sub></b>	Are the regression coefficients
<b>S<sub>p1</sub></b>	The effective emitting area [m <sup>2</sup> ]
<b>S<sub>p2</sub></b>	The effective emitting/absorbing area internal [m <sup>2</sup> ]
<b>S1/ S2/ S3</b>	Switchs
<b>μs</b>	Microsecond
<b>T</b>	Temperature of ZnO valve elements
<b>T</b>	Grading ring tube thickness
<b>T<sub>2</sub></b>	The thickness of the large ring tube

---

$T_1$	The thickness of the small ring tube
$T_a$	Ambient temperature
$T_{cr}$	Critical temperature
$T_s$	Surface temperature
$T_0$	The temperature of ambient air or the temperature of another surface.
$T_E$	Valve element temperature
$T_H$	Housing temperature
$T_A$	Ambient temperature
$\Delta T_{HS}$	Temperature rise of the housing
$t$	time
$T_{pulse}$	The current pulse duration
$t_0$	The start time of the current pulse
$t_1$	The end time of the current pulse
$(t)$	Number of iterations
$T_1/T_2$	The effective emitting/absorbing area external [ $m^2$ ]
$\frac{\partial T}{\partial x}$	Temperature gradient in direction of a coordinate $x$
$\Delta T$	Temperature difference
$U_r$	Rated voltage
$U_c$	The Maximum Continuous Operating Voltage
$U_{m1}$	The value of applied voltage when the direct current is 1 mA
$V_c$	Volume of arrester component
$V_a$	Represents the ambient temperature
$V_v$	Varistor temperature
$V_p$	Housing temperature
$v(t)$	The instantaneous voltage drop across the varistor
$V$	Volume of the varistors
$v_i$	Velocity at position $xi$
$V-I$	Voltage-Current
$W$	Watt

---

$W_E$	Electrical power input to valve element [W]
$W_S$	Energy input due to solar radiation [W]
$W_c$	The activation energy
$X_i$	position of each bat
$x^{best}$	Best solution
$X_i$	The absolute temperature of emitting/ absorbing body
$Y$	Represents the wanted response
$\lambda$	Thermal conductivity [W/(m $\cdot$ $^{\circ}$ K)]
$\dot{\epsilon}$	The maximum emitted flux density
$\epsilon$	Emissivity between the side surface and the environment
$\sigma$	Stefane Boltzmann's constant (5.67. 10 $^{-8}$ [W/ (m $^2$ . $^{\circ}$ K $^4$ )])
$\alpha_c$	Temperature coefficient of specific heat
$\lambda_b$	Wavelength
$\epsilon$	Represents direction and intensity of random-walk
$\gamma, \alpha$	Constant
$\epsilon_1/\epsilon_2$	The emissivity coefficient of body 1/body 2
$\alpha$	Heat transfer Coefficient [W/(m $^2$ . $^{\circ}$ K)]
$\lambda_{air}$	Thermal conductivity of air
$\alpha_{20}$	is the temperature coefficient [ $^{\circ}$ K $^{-1}$ ]
$\beta$	A random vector drawn from a uniform distribution

# **CHAPTER 01**

## **GENERAL INTRODUCTION**

---

---

# *Chapter 01*

---

## GENERAL INTRODUCTION

---

### **1.1. Background**

The increasing consumption of electrical energy has led to the extension of the electric power transmission network and the development of very high voltage lines. At the same time, the need to ensure a sufficient service quality prompted the installation of means of protection against overvoltages [1, 2].

Power networks are often subject to overvoltage constraints, which can be either of internal origin such as switching surges, or of external origin such as lightning overvoltages [1, 3]. Lightning and switching overvoltages are regarded as the main factors contributing to insulation system failure in electric power systems [4]. These overvoltages are very likely to cause flashover and / or destruction of sensitive equipments when any adequate protection is not used [3].

In this regard, an appropriate protection policy against overvoltages is essential to ensure the overall system reliability. Hence, surge arresters constitute the best investment to achieve the expected results. They react to overvoltage by diverting surge current to the ground and limit surge voltage on the system [4]. Their impact on the quality of the energy distributed is undeniable and they make a significant contribution to improving safety for both equipment and people, as well as reducing operating and maintenance costs. Surge arrester is one of the important components in the electrical system network, whether it is in a high voltage system or a low voltage system. It constitutes an indispensable aid to insulation coordination in electrical power supply systems.

Metal oxide surge arresters are currently widely used at the world level because of their electrical performance, such as the high nonlinearity of the characteristic (V-I) of the varistors [5, 6], the low leakage current in steady state and the high absorption capacity of

electrical energy as well as ease of installation and competitive cost [7, 5]. In addition, metal oxide surge arresters are used practically in the entire voltage level from low voltage to very high voltage. The performance of metal oxide surge arresters is a key factor in the determination of power systems [8].

## 1.2. Problem statement

It has been observed that the distribution of potential and electric field along an arrester under normal operating conditions is non-uniform [9, 10]. As a result, the ZnO blocks at the top section subjected to higher potential, excessive electric fields and hence higher thermal stresses than the ZnO blocks at the bottom section, which lead to faster thermal ageing of the ZnO blocks at the top of the surge arrester [1, 10, 11].

The performance and reliability of metal oxide surge arresters may improve with the continuous improvement in their design. Moreover, E-field distribution along varistors column is an important factor that needs to be taken into account during designing of metal oxide surge arresters (MOSA). It can be improved by installing grading ring at the top of the arrester [1, 12].

Several investigations were performed to see the effect of different grading ring parameters on potential and electric field distribution [10, 11, 13, 14, 15, 16, 17, 18], but grading ring dimensions have not optimized. Therefore, optimized design of grading ring of the surge arrester is needed to ensure that the surge arrester can perform better and can provide longer service.

Metal oxide arresters do not contain gaps compared with SiC gapped arresters due to their highly nonlinear properties of ZnO ceramics which react against overvoltage in a very short period of time. Hence, a leakage current flows through the material at operating voltages which causes power losses and heating of the ZnO elements. One of the most important aspects for this type of surge arrester is that of thermal stresses. In fact, when protecting equipment, the surge arrester absorbs energy which causes an increase in temperature of the ZnO elements. The losses due to the joule effect under operating voltage increase with the temperature and it is then possible for the arrester to heat up thermally, leading to its destruction [19, 20].

Metal oxide arrester must have stable thermal performances. Their thermal stability is determined by the balance between the heat generation of ZnO varistors when the operating voltage and overvoltage are applied, and the heat dissipation of the house. The power loss characteristics of ZnO varistors decide the operating reliability of arresters and their life-spans [21].

Furthermore, the effect of solar radiation and environmental pollution on the surge arrester housing, and effect of high energy surge discharge may also contribute to the thermally stress. Under these conditions, it is obvious that thermal phenomena are particularly studied both by manufacturers and by users [20].

Therefore, the thermal behaviour of the surge arrester is vital to assess its operational condition. It presents itself as an important monitoring parameter, making it possible to detect operational failure or when the surge arrester has reached its lifespan limit [22].

The performance of metal oxide surge arrester is determined by the electrical and thermal properties of ZnO varistors elements, insulating materials used and design features of surge arrester [8]. Characterizing the surge arrester behavior in continuous operation requires, on the one hand, an evaluation of the electric field stresses in the varistors column. On the other hand, the temperature distribution within the arresters is interesting as it influences the metal oxide varistors and thus the power loss [23].

### **1.3. Objectives**

The objectives of this work are:

- 1- To design a model of 220 kV polymeric metal oxide surge arrester using 3D-FEM to calculate the electric field and potential distribution along the 220 kV surge arrester.
- 2- To analyze the effects of grading ring parameters on the distribution of the potential and electric field.
- 3- To extract the objective function based on the model L9 of Taguchi design.
- 4- To optimize the design of the grading ring is by minimizing the electric field along the active column of varistors using a bat algorithm.

5- To install and optimize an additional grading ring in order to make the electric potential distribution as uniform as possible and to reduce the electric field value in the top of arrester.

6- To investigate and analyze the thermal behaviour of metal oxide surge arresters.

7- To build an electro-thermal model of metal oxide arrester composed of heat source, thermal resistances and capacitances.

8- To simulate the internal temperatures of the varistors and the surge arrester housing temperatures.

#### **1.4. Contributions of the present work**

The major achievements and contribution of this research work can be summarized as follows:

1- The use of an experimental design methodology based on Taguchi method (L9 model). With the proposed methodology, 3D-FEM combined with the experimental design, the time required for simulations investigations is significantly reduced and then it can be considered as an efficient fast working tool.

2- The optimal design of grading ring such as: positions of grading ring from HV electrode (H), grading ring radius (R) and grading ring tube thickness (T) is achieved by minimizing the electric field along the active column of varistors using a reduced number of simulations based on the Taguchi design and a bat algorithm.

3- The use of an additional ring was proposed in order to make the electric potential distribution as uniform as possible and to reduce the electric field value in the top of arrester. Its parameters have been optimized using bat algorithm in the same way for a single ring.

4- Design an equivalent thermal model for the studied surge arrester in the ATP / EMTP software. This model, allows us to identify the temperature of the varistors and housing according to the dissipated energy. Knowing the temperature of the varistors is an important factor when monitoring the condition of the surge arrester.

## 1.5. Thesis Organization

This thesis has six chapters presented as follows:

Chapter 1 presents the general context, the problematic, the objective and the structure of this thesis.

Chapter 2 will expose the fundamental concepts related to surge arresters as well as a literature review on surge arresters failures and methods for monitoring their condition.

Chapter 3 provides the main fundamental concepts related the thermal behaviour of metal oxide surge arresters, such as thermal stability, thermal runaway critical condition, and heat transfer.

Chapter 4 investigates a new approach for optimal design of grading ring of 220 kV MOSA based on the 3D-FEM combined with the experimental design methodology of Taguchi and the BAT algorithm. The optimal design of grading ring is achieved by minimizing the electric field along the active column of varistors using a reduced number of simulations based on the Taguchi design and then optimized using bat algorithm. By using an optimal design of the single ring, the electric field is reduced by 42% in the top of the 220 kV MOSA and an improvement was recorded on the distribution of the voltage and the electric field along the surge arrester.

It was considered that this improvement is not sufficient, for this purpose, it has been proposed to install an additional ring in order to make the voltage distribution as uniform as possible and to reduce the electric field value in the top of arrester. Also, the additional ring parameters have been optimized using bat algorithm in the same way for a single ring.

Chapter 5 will be devoted to the simulation of the thermal behaviour of the surge arresters. This step will allow us to develop an equivalent thermal model for the surge arrester, their parameters of which will be identified, and will subsequently be implemented in the ATP / EMTP software. This equivalent circuit will give us the possibility of simulating the temperatures of the varistors and of the housing of the studied surge arrester, and therefore the determination of the temperature change during the heating and cooling phases.

Chapter 6 elaborates the main conclusions drawn throughout the study. Finally, future work recommendations to further improve the study proposed in the chapter.

## **CHAPTER 2**

# **SURGE ARRESTERS: A LITERATURE REVIEW**

---

---

# *Chapter 02*

---

## SURGE ARRESTERS: A LITERATURE REVIEW

---

### **2.1. Introduction**

In recent years, using metal oxide surge arresters is a common and prevalent affair for protection of electrical network against lightning overvoltages or switching activities in network. The installation of surge protective devices is one of the most economical and effective ways to avoid or reduce damage of electrical equipments in power network systems. Surge arresters are subjected to several constraints such as, electrical stress, varistors degradation, moisture ingress, higher current, pollution of their insulating surfaces, which leads to their failure. Therefore, their condition monitoring has significant influence on the reliability of power network.

In this chapter, we will present the fundamental concepts related to surge arresters, and then we will discuss their degradation and failure modes. In addition, a review of the methods proposed in the literature for condition monitoring of surge arresters is presented.

### **2.2. Metal oxide surge arrester**

The electrical network was first protected by spark gaps. Then silicium carbide surge arresters associating spark gaps were used. Actually, metal oxide surge arresters are the most used in protecting equipment against transient overvoltages and tends to replace spark-gap and SiC surge arresters [24].

During the sixties that varistors made of a ceramic based on zinc oxide appeared on the market for the protection of electronic circuits.

As early as 1970, manufacturers of arresters began to develop surge arresters using these ceramics. Metal oxide varistors, which are the active elements in the arrester, have excellent properties [4, 24] .

For the electrical engineer, these components have two main advantages [25, 26]:

- ✓ A very high coefficient of non-linearity over a wide current range.
- ✓ A high energy absorption capacity and a short time response.

Metal oxide arresters, from medium voltage to highest voltage, are simply made up of a stack of non-linear metal oxide varistors. Sometimes, but only for very high voltages, they include some additional capacitors placed in parallel on the varistors at the top of the surge arresters and intended to improve the voltage distribution along the varistors column [3, 27]. The whole is placed in an insulating housing, generally made of porcelain or polymer material. Figure 2.1 shows two types of metal surge arresters, porcelain housing (a) and silicone housing (b). The dimensions of the enclosure shed must take into account the effects of pollution and cooling.



**Figure 2.1** Structure of metal surge arresters: (a) porcelain housing; (b) polymer housing

### 2.2.1. Internal parts of a surge arrester

The internal parts of metal oxide surge arrester (MOSA) differ considerably between a porcelain surge arrester and a polymer surge arrester. The only thing common between these two designs is that both include a stack of series-connected metal oxide varistors with components to keep the stack together.

The varistors column is a series of metal oxide varistors blocks of cylinder or hollow style [3, 25]. Their diameter is within a range of about 30 mm when used for distribution systems, and up to 100 mm or more for high and extra high voltage systems and special applications [28].

The length of the active part is fitted to the housing length of the unit by means of metallic spacers [28]. The use and arrangement of metallic spacers is arbitrary in engineering [25].

Metal oxide blocks are manufactured in the same manner. They are composed of a stack of varistors with a strongly nonlinear characteristic. These varistors are variable resistors. At low values of the applied voltage, a varistor behaves like a strong resistance of value obeying the law of ohms, but above a threshold voltage, the device becomes strongly conductive exhibiting a low impedance at high voltages. When the varistor becomes conductive, it maintains the applied voltage at an indicated maximum, which the protected system can withstand.

A porcelain-housed arrester contains normally a large amount of dry gas such as air, nitrogen, SF<sub>6</sub>, while a polymer-housed arrester in most cases normally does not have any gas-filled between active part and interior of the housing in most cases [3, 24, 29]. This means that the requirements concerning short-circuit capability and internal corona must be solved quite differently for the two designs. Surge arresters containing an enclosed gas volume must be fitted with some type of pressure relief system in order to prevent them from bursting during internal pressure build-up by short circuit. Therefore, the arresters can be classed into two types, gas-filled or solid-filled. For the solid-filled arrester, the interior of arresters is filled with organic or inorganic solid-insulation materials such as silicone rubber or quartz sand, and there is practically no gas inside the arresters [25].

### 2.2.2. Surge arrester housing

The housings of surge arresters traditionally have been made of porcelain, but the trend today is towards the use of polymeric insulators. The basic idea is to replace the porcelain housing with a polymeric housing [29] .

The polymer housing is made of a special material based on silicone or EPDM (Ethylene Propylene Diene Monomer) [3]. The housing is molded directly onto the varistors column, or providing a layer of air between the housing and the varistors column. The mechanical strength of the surge arrester is sometimes ensured by a coating of glass fibers around the varistors. To combine the glass fiber design and the insulator, two main possibilities exist, firstly, the glass fiber design can be molded directly into the rubber insulator and secondly, the boundary between the glass fibers and the rubber insulator is filled with grease or gel, generally of silicon.

#### 2.2.2.1. Porcelain Housing

Metal oxide surge arrester mainly consists of a hollow porcelain housing, a stack of metal oxide (MO) varistors and a flange including the sealing and pressure relief system. A porcelain-housed arrester is filled with gas between the active column and the external insulator [28].

Figure 2.2 shows the cross section of a unit of an MO arrester with porcelain housing. Supporting rods out of FRP (fiber-glass reinforced plastic) material encircle the metal oxide varistors column like a cage. Holding plates – also out of FRP – additionally, provided on the one hand, prevent the supporting rods from being bent apart, and on the other hand, limit possible sagging of the whole construction towards the housing walls. A strong compression spring which is attached to the upper end of the column braces the active part in the housing [20, 28, 29].

The most important part with respect to safety and reliability is the sealing and pressure relief system. The sealing system must be designed to prevent ingress of moisture for the whole lifetime.

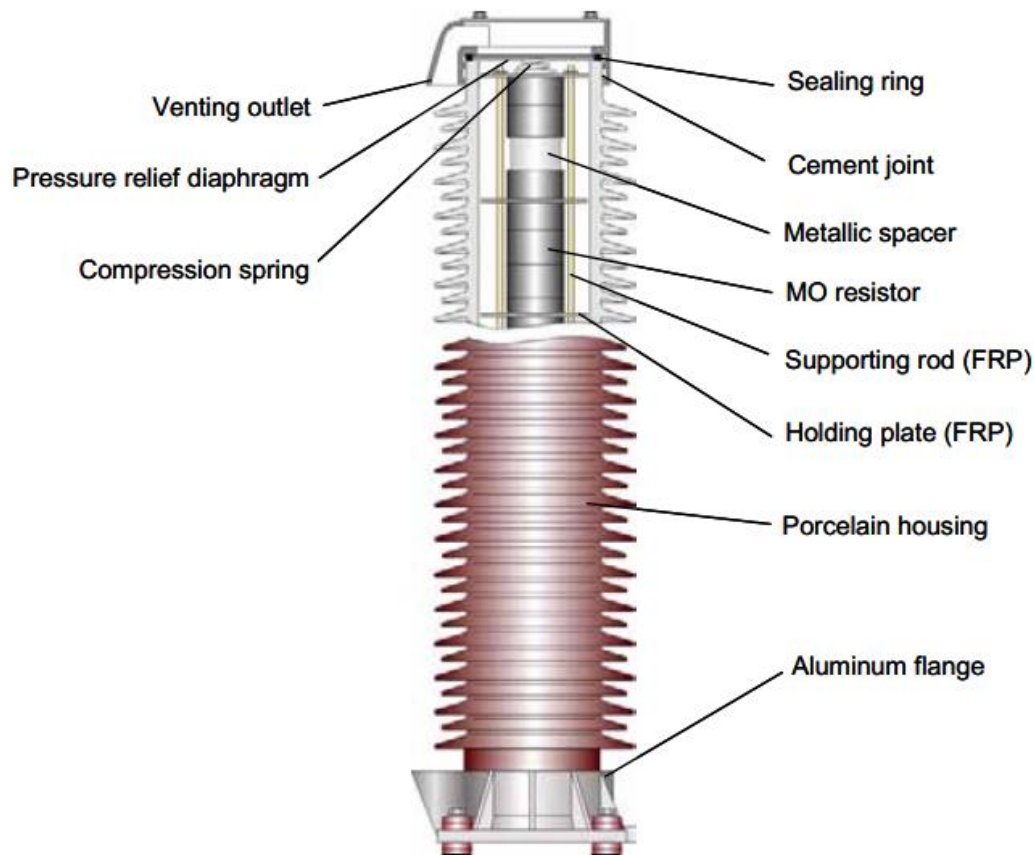


**Figure 2.2** Cross section of the unit of a porcelain housing MO arrester [28]

In case of an arrester failure and internal short circuit, the pressure relief system must release the pressure inside the housing which is caused by the arc heat before the housing is destroyed by the pressure shock wave. Furthermore, the pressure relief forces the arc out of the housing to prevent from further pressure built-up.

#### 2.2.2.2. Tube design polymer housing

The housing of a porcelain surge arrester might be replaced by a polymer housing which consist of a fiber reinforced plastic (FRP) tube with polymer sheds molded onto it. The construction of this tube design polymer housing is a more conventional approach, looking quite similar to that of a porcelain housed arrester [30, 31]. Silicone is directly molded onto the FRP tube. This tube ensures the high mechanical strength of this surge arrester. At the ends, the flanges are fixed with a special sealing system. The flanges are equipped with a directional pressure relief device. The stack of varistors elements is mechanically supported inside the FRP tube by an internal cage structure of FRP rods. This stack is clamped between the flanges as shown in figure 2.3 [31, 32].

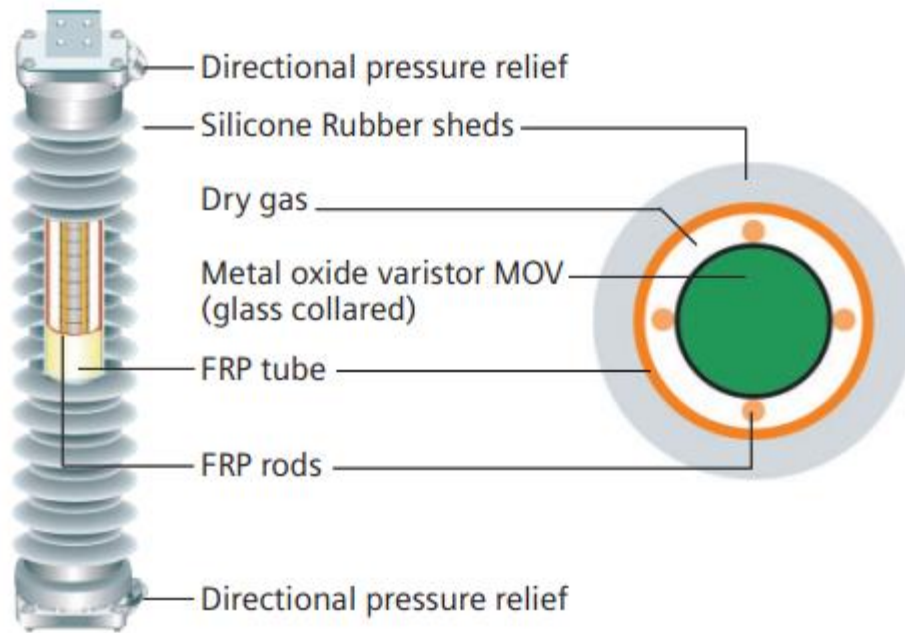


**Figure 2.3** Tube design for polymer surge arrester [32]

The silicone rubber material of the sheds is strongly hydrophobic which dramatically reduces the risk of surface flashover [30].

Tube design polymer housing surge arresters can be used in a double function as a surge arrester and as an insulator support to save space in the substation [30, 32]. It can be mounted at any vertical plane angle throughout the 360° range [32].

The mechanical properties of the FRP tube material are significantly better than of porcelain. Furthermore, the mechanical properties may be adjusted according to the manufacturers or customers' needs by varying the parameters of the FRP tube such as wall thickness or fiber angle. Thus, polymer tube design arresters are used where there are extremely mechanical requirements, in particular with respect to earthquakes [30, 32].

### **2.2.2.3. Cage design polymer housing**

As shown in figure 2.4, silicone is directly molded onto MO varistors (MOV) blocks and FRP rods, ensuring the total enclosure of all components to prevent partial discharges or moisture ingress [32]. This design consists of loop or cage of FRP rods around the block column. The MOV blocks are clamped between the metal end fittings with pre-stressed FRP rods [30, 31, 32].

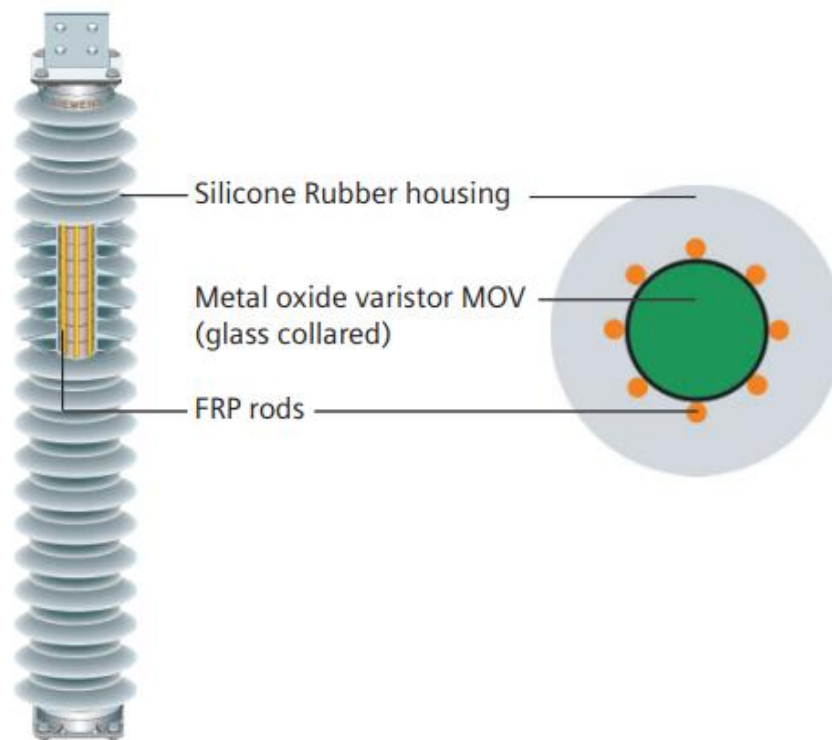


**Figure 2.4** Cage design for polymer surge arrester [32]

Unlike to tube design surge arresters, no pressure relief system needed. In case of arrester failure and internal short circuit the arc burns through the housing without significant pressure built-up. However, MOV may break and the supporting FRP rod structure may be burnt resulting in a collapse of the arrester and a total loss of the mechanical stability [30, 32].

The cage design is notable for its high mechanical strength in conjunction with minimal use of materials, and light weight. This design is particularly suitable for most standard applications and for line arresters [32]. The mechanical strength of cage design is lower than that of the tube design arresters [30, 32].

#### **2.2.2.4. Wrap design polymer housing**

Wrap design surge arresters have MOV blocks wrapped with fiberglass ribbons impregnated with epoxy resin to create a stack of MOV blocks. This MOV stack is then inserted into a pre-molded, EPDM based alloy or Silicone Rubber housing to create a module. The space between the module and housing is filled with grease or some form of dry interface material.

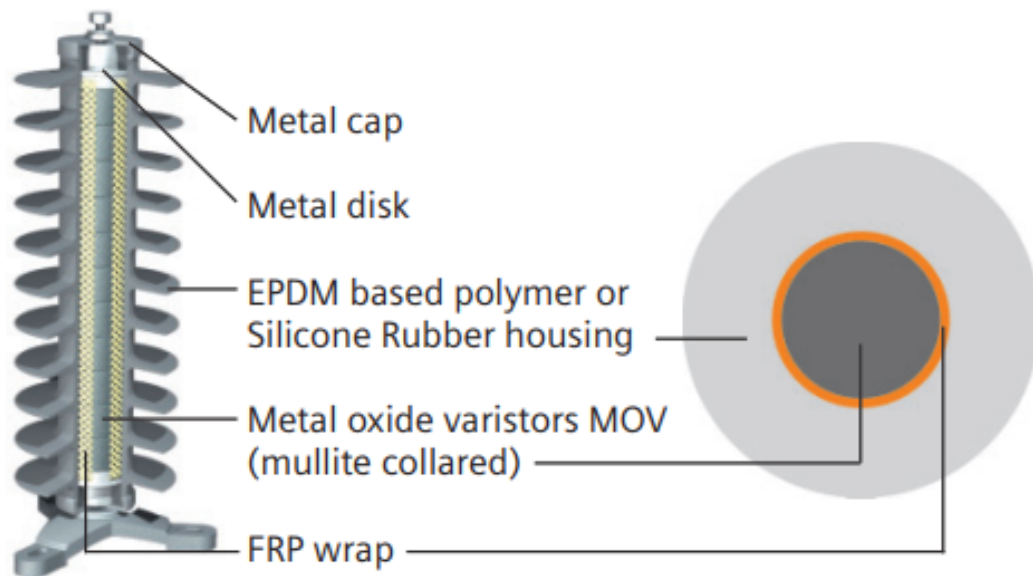


**Figure 2.5** Wrap design for polymer surge arrester [32]

The two ends are then covered with steel caps (Fig. 2.5), and that allows to moisture ingress into end face [28, 33]. The stacks of MOV blocks have no reinforcement and are simply held together with fiberglass wrap. This design does not provide enough mechanical strength, permits very high deflection under operating loads [32]. The wrap consists of flammable components (fiberglass with epoxy resin). Surge arresters of this design will continue to burn after an overload [32].

#### 2.2.2.5. SF<sub>6</sub> gas insulated metal oxide surge arresters

Gas-insulated surge arresters are in principle an integral part of an SF<sub>6</sub> gas insulated substations (GIS) where the interior atmosphere is composed of SF<sub>6</sub>.

Gas-insulated surge arresters principally consist, as all other MO arrester designs, of one or more parallel columns of MO varistors installed in an earthed metallic enclosure (metal vessel) filled up with SF<sub>6</sub> gas. Due to the very short radial distance between the active part on high voltage potential and the earthed vessel a relatively high capacitive stray current is flowing, which leads to an unfavorable axial voltage distribution along the active column of metal oxide varistors. For this reason, a metallic grading elements (hoods or rings) or capacitive grading elements have to be taken [31, 34].

GIS surge arresters exist with only one phase or with all three phases in one metallic

enclosure. For higher system voltages, generally a mechanically three or four column design is used.

In order to achieve an economical and space saving design and to minimize the impact of stray capacitances to the earthed vessel, there are special designs where a single columns are built up by connecting MO varistors elements in series. This reduces the overall physical length of the active part. Figure 2.6 shows the principle design of the GIS surge arrester. Main advantage of GIS arresters are their excellent behavior under pollution conditions, very high availability and the possibility to be integrated into the SF6 substation for optimized protection of the equipment, and their favorable performance under seismic stress [31, 34].

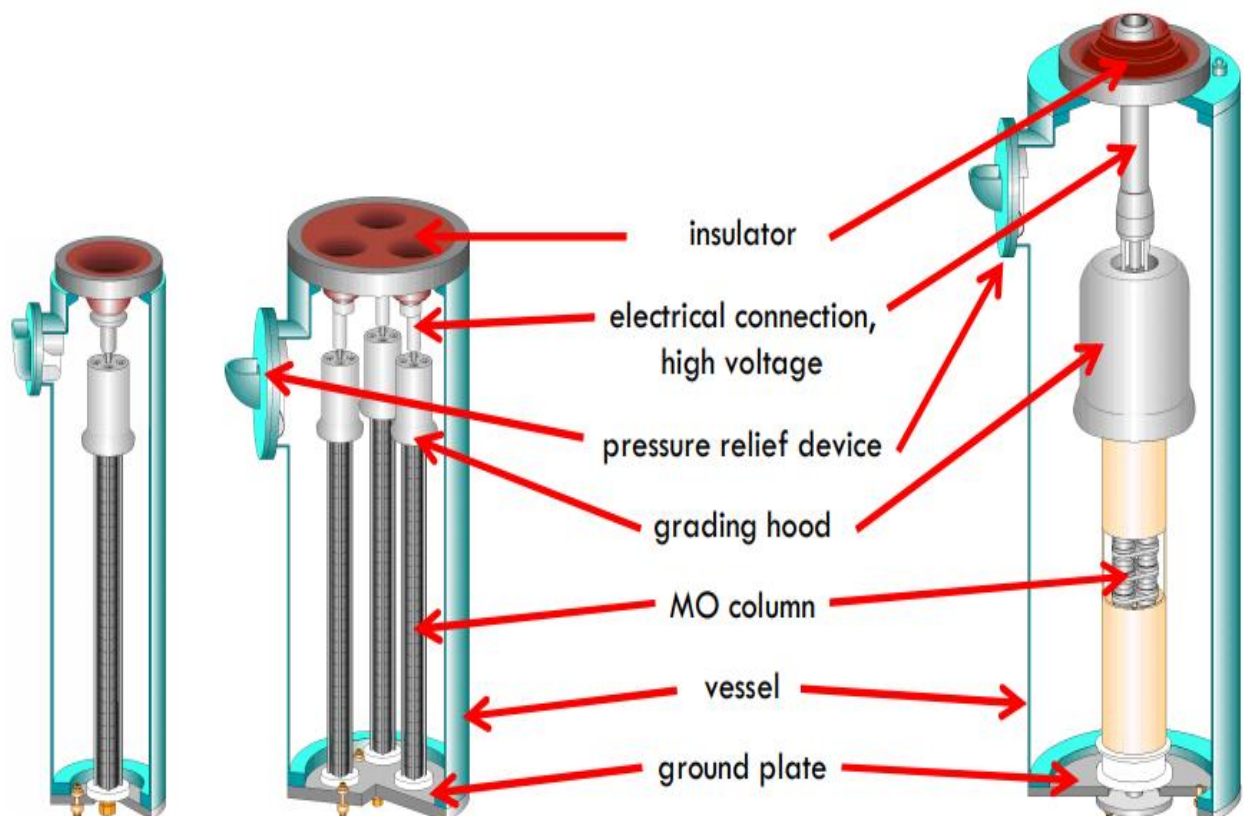


**Figure 2.6** Design of GIS arresters for different systems voltages: Left: single phase design for system voltage up to 170 kV. Middle: Three phase design up to 170 kV. Right: single phase design for system voltages above 170 kV with electrical one phase, but mechanically three columns of MO varistors, courtesy Siemens [31].

### 2.3. Functional principle of metal oxide surge arresters

Under continuous operating voltage, the impedance of the metal oxide surge arrester is very high and the varistor is traversed by a very low current (less than 1 mA). When a surge overvoltage appears (switching or lightning overvoltage), the resistance decreases rapidly, the varistor suppresses the overvoltage so as to constitute a preferential path to flow the corresponding energy to earth. After completely discharging the surge energy, the arrester will then return to its normal high impedance with its original characteristics restored [4, 35].

The main advantage of the metal oxide varistor is the strong nonlinearity of its V-I characteristics. The non-linearity is such that when the current flowing through the varistor goes from 0.1 mA to 1 kA for switching overvoltages and 20 kA for lightning overvoltages, the voltage at its terminals is only multiplied by approximately two, which makes this element an almost ideal protective device [36].

### 2.4. Advantage of polymeric surge arrester

Polymer insulation provides many advantages compared to other insulations [3, 4]:

- High mechanical strength (use of fiberglass reinforced structures)
- Lower weight and smaller size of the arrester, so it is easier to be suspended in power systems and their ease of handling during transportation and installation.
- Good performance in contaminated environments, especially when the housing is made of silicone rubber.
- Shatter resistance

### 2.5. Characteristic parameters of metal oxide surge arresters

The following essential parameters are used for all definitions relating to surge arresters [1, 12, 37]:

➤ **Rated voltage of an arrester ( $U_r$ )**

Is the maximum permissible root mean square (r.m.s) value of power-frequency voltage between the arrester terminals for which it is designed to operate correctly under temporary

overvoltage conditions as established in the operating duty tests (a 10 second power frequency overvoltage is applied to the surge arrester).

➤ **The Maximum Continuous Operating Voltage ( $U_c$ )**

Is the maximum value of a sinusoidal power frequency voltage that the arrester is able to withstand continuously under given ambient conditions.

➤ **Nominal discharge current of an arrester ( $I_n$ )**

Is the peak value of a current wave of 8/20  $\mu$ s bi-exponential form, which is used to classify the arrester. In medium voltage, it can take the value 5 kA or 10 kA. The protection level of the surge arrester is set at this current.

➤ **Residual voltage of an arrester**

Peak value of the impulse voltage that appears between the terminals of an arrester when it is crossed by the nominal discharge current.

➤ **The energy absorption capacity**

Is reflected by the withstand to current waves of bi-exponential shape 4/10 and by the withstand to current waves of rectangular shape, the duration and amplitude of which define the severity.

## 2.6. Main criteria for dimensioning a surge arrester

The main criteria for dimensioning a surge arrester are [3, 37]:

- ✓ Its Maximum Continuous Operating Voltage (**MCOV**) must be greater than the maximum operating voltage of the network. The voltage level in which the arrester will expose over most of its life is about 5% above the nominal line to ground voltage.
- ✓ Its rated voltage is fixed at  $1.25 \times \text{MCOV}$ .
- ✓ Its level of protection.
- ✓ Its energy capacity to withstand temporary overvoltages, given by an amplitude-duration curve.
- ✓ The use of a surge arrester is only effective under certain implantation conditions, and in particular according to the distances, which separate them from the equipment to be

protected and from its earth, hence the importance of the notion of the surge arrester protection distance.

## **2.7. Surge Arrester failures**

The some kinds of failures that are more frequent or more probable to happen in MOSA: Sealing problems and internal humidity, varistor degradation, varistor displacement, superficial pollution, irregular voltage distribution [25, 38].

### **2.7.1. Sealing problems and internal humidity**

Arresters are manufactured with a sealing system that provides a complete insulation between the inner area of the equipment and outside. Any failure in this sealing system can lead to humidity ingress in the arrester. The presence of moisture in the inner region of the arrester brings changes in its electrical characteristics, increasing the superficial current and reducing the insulation, and can lead to internal discharges [25, 38, 39].

In addition, the loss of isolation allowing the exchange of gases, and yields to changes in warming characteristics of the arrester due to the gases circulation. Sealing loss can occur at surge arrester due to failures in manufacture process, or caused by the natural aging process of the equipment [5].

### **2.7.2. Degradation and destruction of varistors**

The term varistor degradation is often used to describe the electrical state of a varistor. The degree of degradation is a good indication of varistor reliability. A varistor in good conditions conducts a current in the order of microamperes for a continuous operation condition [1, 38].

A metal oxide surge arrester must have an excellent nonlinear V-I characteristics, which is capable of withstanding high electrical stresses due to surge overvoltages before returning to its normal operating condition. However, the V-I characteristics may experience degradation resulting from the effects of various electrical and thermal stresses and environmental pollution. Degradation due to the thermal stresses is normally caused by the effect of high energy surge discharge, which results in increased temperature of metal

oxide varistors. Furthermore, the effect of solar radiation and environmental pollution on the surge arrester housing may also contribute to the thermally effected degradation. Meanwhile, degradation due to the electrical stresses is normally caused by the effects of lightning discharge, switching operation and temporary overvoltages [1, 4].

### 2.7.2.1. Failure modes of varistors

Severe and frequent electrical surges, as though as humidity are able to damage the varistors so that they miss their electro-thermal stability, presenting excessive heating and a high leakage current. Also, leakage current of the surge arrester can be increased by any increase of ageing level [40]. Sometimes, punctures appear on the varistors surface, indicating a discharge across the varistors structure. There are three main failure modes of varistor elements [26, 41, 42]:

- Thermal runaway.
- Electrical puncture.
- Physical cracking.

Failure mode due to thermal runaway can be investigated through the relationship between heat generation and heat dissipation of varistors elements. During surge energy absorption event, the leakage current and consequently the joule heating of varistors, increase with temperature. Thus, if the temperature is raised above the thermal stability temperature  $T$ , power input may exceed heat dissipation, and thermal runaway occurs. Thermal stability of metal oxide varistors disks, as well as of complete arresters, has been studied extensively [4, 20, 43].

- In Ref [26], the experimental results state that the measured energy absorption capabilities are highly scattered for different commercial varistors, and for the same varistors under diverse current waves. Thermal runaway is related to current and voltage instability, while physical cracking is due to huge thermal stresses, and electrical puncture is caused by current concentration.

- In Ref [41], two different failure modes of varistor are considered: puncture and cracking. They are related to the electrical nonuniformities of varistors disks and caused by the localization of the current in the breakdown mode; local currents cause local heating, which

leads to nonuniform thermal expansion and thermal stresses.

- In Ref [7], the failure processes of metal oxide varistors caused by multiple lightning impulse currents were investigated. The performance changes of metal oxide varistors after multiple lightning impulses were analyzed. According to the results of this study's experiments, the failure mode of metal oxide varistors after multiple lightning impulses involved the rapid deterioration of the electrical parameters with the increase of the number of impulse, until destruction occurred by side-corner cracking.

### **2.7.3. Varistors displacement**

This problem results from the incorrect transportation or storage of the arrester. If they are kept for a long period in the horizontal position, the effects of gravity or trembling can displace the varistors in central position so that they lose their alignment in the column. However, this kind of problem may be caused by manufacturer process due to assembly errors. As a result, the contact surface between varistors is diminished, modifying the conduction patterns, and leads to the creation of preferential conductive pathways in the region of the best contact which produces overheating in the region and premature degradation of the varistors [5].

### **2.7.4. Superficial pollution**

Pollution is a major problem in the degradation of the insulation of electrical power systems, mainly the ones located in highly polluted sites [3]. The surge arresters are exposed to various constraints. Among them, the pollution of their housing constitutes one of the factors of the first importance in their performance and their reliability [44, 45] . Indeed, in rainy weather or of fog, polluting deposits attaching to insulating surfaces. The humidification of the polluting layers facilitates in fact, the flow of a leakage current causing local heating and thereafter the drying of the pollution layer, thus the formation of the dry band and discharge appearance that can develop into total flashover when the potential gradient exceeds the breakdown strength [1, 46, 47] . Therefore, it is significant to the users and to the manufacturers to hold accounts this type of problem to avoid the unexpected destruction of the surge arresters. Therefore, several studies examining the effect of pollution on the performance of surge arrester have been published on literature.

Pollution test results of single unit 110 kV metal oxide surge arresters with porcelain housing according to the solid layer and salt fog methods were presented in reference [46]. The internal and external charges were measured. The formation of dry bands on the housing was observed, especially during salt fog tests. In such cases, the varistors temperature can reach about 70°C. The simple electrical model of the arrester enabling calculations of voltages and currents as a function of arrester and pollution parameters has been developed.

I. A. Metwally [48] presented an experimental investigation of distribution-class surge arrester (SA) performance under dry, clean-fog and salt-fog conditions. Both the internal and the external currents were measured for each SA up to its maximum continuous operating voltage (MCOV). The lower part of SA housing was greased near its base to separate the internal and external currents. When the leakage current pulses become repetitive, the leakage current dries the conductive layer and dry bands are formed. Short current peaks may appear at the signal crest due to discharges across dry band areas. This can lead to degradation for both the external housing and the internal active materials.

In Ref [47], an algorithm was developed to study the voltage distribution and the current inside and outside the polluted metal oxide surge arrester (MOSA) and flashover conditions can be achieved. Dynamic surface resistance change during the formation of dry bands due to leakage current has been considered.

In Ref [49] an equivalent circuit for a 15 kV metal oxide surge arresters under polluted conditions was presented. The simulation of the discharge on the dry band was carried by opening the switch S1 firstly at the same time the switch S2 is closed. The operation of these two switches simulated a formation of dry band. Then after a little time of 0.2 ms by closing the S3 switch for a short duration of 0.1 ms to simulate a discharge across the dry band.

Alti et al [50] were used an electrical circuit model to simulate the performance of the polymeric surge arrester under polluted condition in EMTP-ATP software. In order to study the influence of the presence of early discharge activities on the behavior of the surge arrester, they simulated the dry band discharge by adopting an insulators flashover dynamic

model. This model allows predicting the behavior of a polluted insulating surface under AC voltage. It uses the Hampton's propagation criterion, and the Rahal's speed expression.

Thipprasert et al [51] modeled the Metal Oxide Surge Arresters in 22kV Distribution System by ATP-EMTP program and compares the experimental testing of surge arrester. The proposed model is used for leakage currents analysis of distribution system. Moreover, it will be useful to select or design suitable SA for using in places with salt conditions, high rainfall, high wind speeds and high humidity.

The effect of pollution and moisture on the surge arrester characteristics is also investigated [52]. Samples subjected to surface pollution were created according to the IEC 507 standard under both wet and dry conditions. The partial discharge related signals are recorded and studied. Electromagnetic emission at the very high frequency (VHF) range of 30 to 300 MHz is used to detect surface defects on outdoor polymer metal oxide surge arresters. The results of this work show that the physical defects on the polymer metal oxide surge arrester produced partial discharge in the form of electromagnetic signals at normal operating voltage.

Khodsuz et al [45] were observed that surface contamination has influence on resistive harmonic components, especially the third and fifth harmonics. To accomplish this purpose, experimental tests have been performed on various polymer housed surge arresters.

### **2.7.5. Irregular voltage distribution**

Voltage distribution along varistors column is an important factor that must be taken into account during designing metal oxide surge arresters [53]. This results from the irregular electric field through different regions of the arrester. As this field is more intense in the region close to the high voltage terminal, the varistors located in this region are submitted to a higher voltage drop, resulting in a premature degradation of these varistors when compared to the ones located in lower regions of the equipment [39]. In order to improve the distribution of the voltage and the electric field along the surge arrester under proper conditions, more detail will be discussed and annotated in chapter 4.

The existence of any stray capacitance will cause a non-uniform voltage distribution along

the surge arrester. When metal oxide arrester operates under polluted conditions, it can be stressed with severe non-uniform field distribution, which could cause external breakdown, internal partial discharges and a rise in the temperature of the varistors. Several published works have studied the distribution of voltage in the presence of pollution on the surge arrester housing [8, 49, 54].

The distribution of the potential and the electric field can be influenced by the presence of pollution on the surface of the surge arrester. The finite element method (FEM) was realized. The COMSOL Multiphysics software was used for this purpose [50]. The results obtained show that the formation of dry bands affects directly on external potential. The interaction between the polluted polymeric housing and the inner varistor column due to capacitive coupling is responsible for the voltage rise of varistor elements. The potential distribution along the surge arrester is especially high near the dry zone.

These results are in agreement with the results obtained in reference, where the voltage is especially high near the dry zone. The potential difference between inside and outside of the arrester block causes very high electric field at the position of dry band. This high voltage may lead internal charges. These internal charges may lead to destruction of arresters.

## **2.8. Surge arresters condition monitoring methods**

Surge arrester condition monitoring has a significant influence on the reliability of power system. For condition monitoring of surge arresters, many offline and online methods have been presented in literature such as leakage current measurement, Voltage–current (V–I) characteristic curve analysis, electro-magnetic field measurement and temperature measurement [45, 55]. Thermo-vision and electromagnetic tests are non-destructive monitoring methods which are used for surge arresters condition monitoring. The advantages of these methods are that there is no need to disconnect the equipment and secure distance from object.

Condition monitoring of surge arresters, can be divided into two different groups: online methods, where the arrester is connected to the system and energized with the service voltage during normal operation, and offline methods, where the arrester is disconnected

from the system and energized with a separate voltage source on site or in a laboratory. Accurate results may be obtained by using the offline methods [56, 57, 58]. Requirement of expensive equipment for these experiments and the need for disconnecting the surge arrester from the system are drawbacks of offline method [45].

### 2.8.1. Leakage current measurement

The AC leakage current of surge arresters is the most important information for monitoring and the condition assessment process of the surge arrester. The most common methods for condition monitoring of surge arresters are online measuring of total leakage current and extraction of the resistive current by means of analytical methods. Portable instruments, which connected to the earth terminal of the arrester by means of a clip-on, or permanently installed current transformer have been used to measure online leakage current [45]. Figure 2.7 illustrates the use of a leakage current monitor. The instrument can be used to display or monitor on a computer remotely and store data at intervals as required providing diagnostic information. Now it is easier to take corrective measures in time. The instrument can also be programmed to give an alarm at a preset value of  $I_r$  when the actual operating conditions exceed this [59].

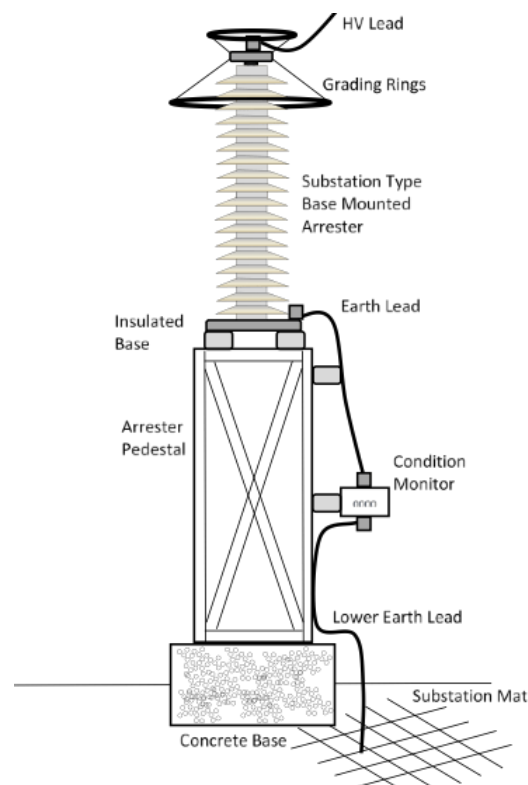


**Figure 2.7** Measuring leakage current through an arrester [59].

M. Khodsuz et al [55] presents proper indicators for evaluation of the surge arrester condition based on the leakage current analysis. Maximum amplitude of fundamental harmonic of the resistive leakage current ( $I_{mr1}$ ), maximum amplitude of third harmonic of the resistive leakage current ( $I_{mr3}$ ) and maximum amplitude of fundamental harmonic of the capacitive current ( $I_{mc1}$ ) have been used as indicators for surge arrester condition monitoring. Based on 3D-FEM and ATP-EMTP, surge arrester model has been performed for calculating leakage current. The effects of operating voltage fluctuation, third order of voltage harmonic, over-voltage and varistors aging have been investigated. This study shows that the introduced indicators are proper criteria for surge arrester condition monitoring.

Purpose of the authors in reference [60] is to measure and analyze of the leakage current of 20 kV polymer and porcelain metal oxide surge arresters under different applied voltage when changes the ambient humidity in an artificial fog chamber. The circuit used in this test to measure the total leakage current of a surge arrester is shown in the figure 2.8. The characteristics of leakage current in the time and frequency domain were measured and analyzed, Fast Fourier Transform (FFT) amplitude and the resistive component of the leakage current is measured, using a voltage reference signal. It found out that, in humid ambient conditions, amplitude of first harmonic order increases with increase in humidity. It is a good indicator for evaluating arresters in humid ambient conditions.

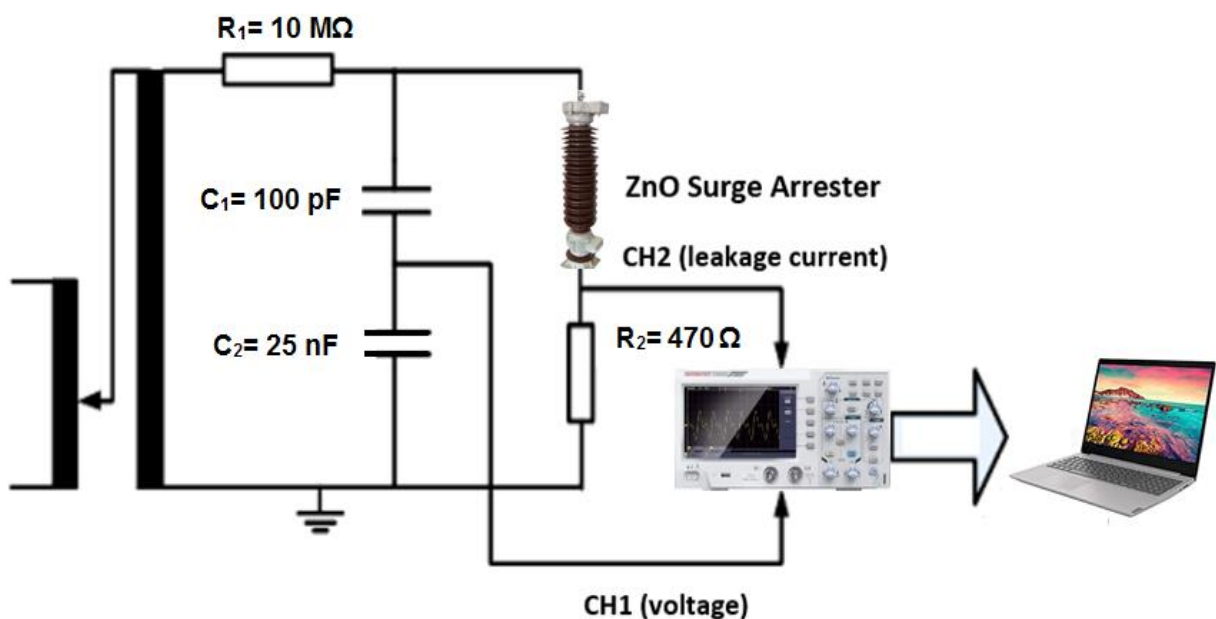


**Figure 2.8** Circuit for measurement of total leakage current of a surge arrester [60]

In reference [58], the total leakage current of two 20 kV metal oxide surge arresters is measured and the resistive component for three different cases (brand new arresters, under artificial rain and measurements after impulse voltage subjection) is computed. The analysis of the produced results can be useful in correct diagnosis of arresters condition and in more effective scheduled maintenance.

Surge arrester model for calculating leakage current has been performed in ATP-EMTP [61]. Several methods have been used to extract the resistive current from the total leakage current of the arrester [57, 62, 63]. A modified method based on time-delay addition method was introduced to extract the resistive current from the surge arrester total leakage current without measuring voltage signal [61]. In addition, the signal processing has been done using MATLAB software. To show the accuracy of the proposed method, experimental tests have been performed to extract resistive leakage current by the proposed method.

### **2.8.2. Electromagnetic field measurement**

Electromagnetic emission at the very high frequency (VHF) range of 30 to 300 MHz is used to detect surface defects on outdoor polymer metal oxide surge arresters. The partial discharge related signals are recorded and studied. The effect of moisture and pollution on the characteristics is also investigated [52].

In this proposed method, monitors the electromagnetic pulses originating from the electrical discharge on a polymer surge arrester. A broadband bi-conical antenna is used to record electromagnetic pulses from the surge arrester at normal operating voltage as shown in figure 2.9. The output from the antenna is connected to the preamplifier via a coaxial cable. The results of this work show that the physical defects on the polymer metal oxide surge arrester produced partial discharge in the form of electromagnetic signals at normal operating voltage.

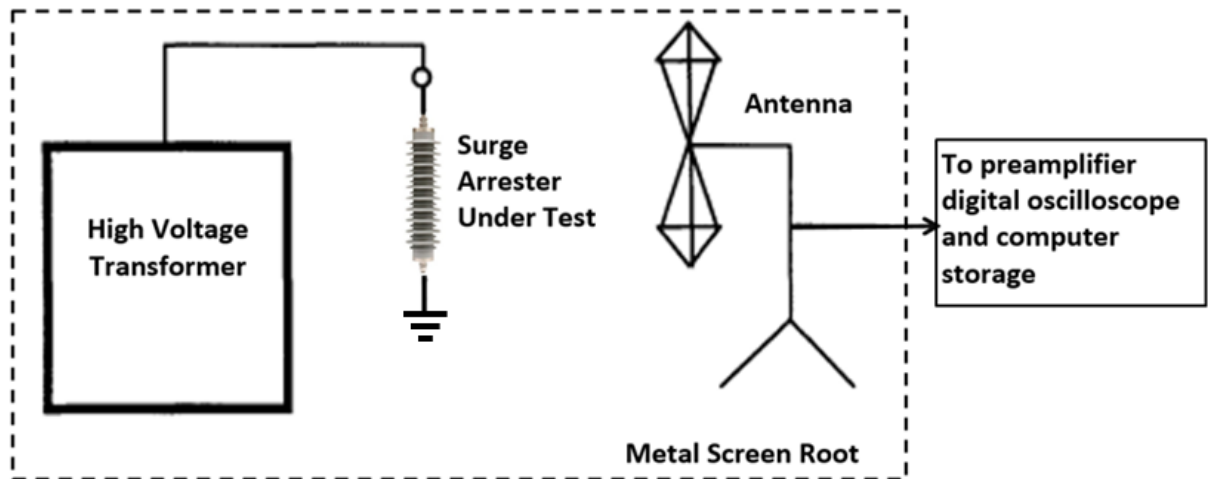


**Figure 2.9** Measurement setup of PD [52]

In order to evaluate if metal oxide surge arrester present any partial discharge (PD) in case of internal moisture and how applicable it is as a condition monitoring diagnostic method, eight distribution metal oxide surge arresters from four different manufacturers were submitted to an immersion test for 19 days [64]. The partial discharge and leakage current levels were measured daily. For those samples identified with internal moisture, the partial discharge activity showed a special behavior keeping a limited amplitude itself but presenting a high repetition rate.

### 2.8.3. V–I characteristic curve analysis

A reliable metal oxide varistor must be capable to maintain its original V–I characteristics during normal operating condition and after discharging high energies due to transient surges. Previous researches have shown that the degradation greatly influences the nonlinear V–I characteristics, which in turn produces higher leakage current through the surge arrester [4, 62]. The V–I characteristics give a realistic image of the electrical behavior and of changes caused by any kind of degradation. However, measuring of the V–I characteristics requires equipment, which is usually not available on site. It is therefore hardly used for online monitoring [62]. To evaluate varistor degradation experimentally, an aged varistor has been extracted from surge arrester which has been installed in power system for 15 years [45]. V–I characteristic of aged varistor, which was extracted from used surge arrester, was changed and reduced compared with the new varistors as shown in figure 2.10.

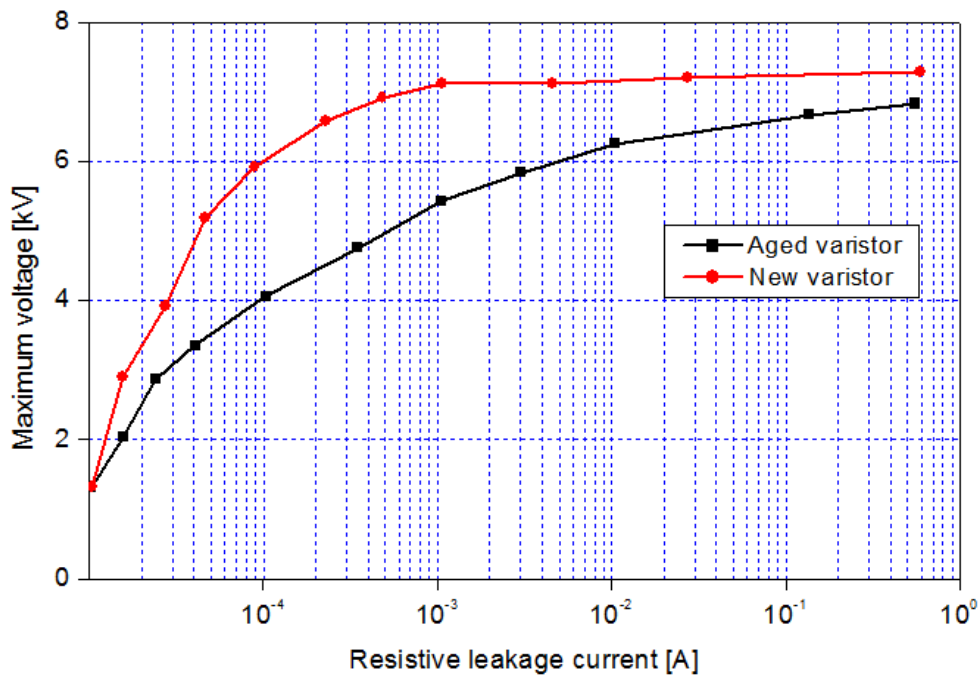


**Figure 2.10** V-I characteristic of aged and new varistors [45].

To investigate the relationship between the V-I characteristics and degradation level, V-I characteristics at room temperature were tested every 100 lightning impulses [42]. Performance deterioration of the arrester under successive 8/20  $\mu$ s lightning strikes was measured. Deterioration steps of V-I characteristics and residual voltage of arrester were detected. It can be seen that the nonlinear characteristic of V-I notably decreases as the values of  $U_{m1}$  and maintains a downward trend compared to the curve of the new varistors.

#### 2.8.4. Thermo-vision

Thermo-vision, sometimes referred to as thermography is a useful tool that is capable of detecting a number of problems on HV insulators, surge arresters and overhead transmission lines. Infrared video detects temperature rise on an object. In the context of HV engineering, the temperature rise is associated with detrimental phenomena such as corona discharge and leakage current [52]. The resistive component of the leakage current is responsible for the heating of the surge arrester and its increase is reflected as an increase in the temperature of the equipment. If the surge arrester is in perfect condition, such heating is practically uniform on the surface and will be within predetermined limits [65]. Although infrared imaging has proved to be effective in detecting anomalies associated with heat, its

application in HV equipment monitoring is still limited. The high cost of infrared cameras makes it unsuitable for large area installation and the correct interpretation of the infrared image depends on the experience of the camera operator. Furthermore, the technology is susceptible to external influences such as wind, solar flux and high load.

## **2.9. Conclusion**

This chapter provides the fundamental concepts related to metal oxide surge arresters. In addition, we have synthesized the knowledge already undertaken on the degradation and failure modes of metal oxide surge arrester. Some kinds of failures that are more frequent to happen in MOSA are well discussed in this chapter, where degradation of varistors is one of the most important causes of arresters failure.

Therefore, the techniques or methods for conditions monitoring of the surge arrester existing in the literature were presented. The most common methods are online measuring of total leakage current and extraction of the resistive current. This chapter allowed us to present the notions useful to the good conduct of this research project.

## **CHAPTER 3**

# **THERMAL BEHAVIOUR OF METAL OXIDE SURGE ARRESTERS**

---

# THERMAL BEHAVIOUR OF METAL OXIDE SURGE ARRESTERS

---

### **3.1. Introduction**

The operation of metal oxide surge arresters, in permanent or transient conditions, is governed by their electrical and thermal characteristics [20]. The degradation of the ZnO elements which leads to the increase in the resistive component of the leakage current for a given operating voltage. The increase in the resistive leakage current increases the temperature of the elements, which consequently increases the resistive leakage current in these elements. This process continues cumulatively leading to thermal instability causing short circuit and internal flashover and eventually total failure of surge arrester can be produced [4, [66]. Indeed, the electrical behavior of a MOSA is strongly linked to its thermal characteristics. Therefore, the laws of heat transmission are of decisive importance for the study and operation of surge arresters [1], [67]. Under these conditions, it is essential that the thermal phenomena of surge arresters must be particularly studied by manufacturers and users.

### **3.2. Thermal stability of metal oxide surge arrester**

Thermal stability is one of the most important application criteria for metal oxide surge arresters [68]. Arrester is thermally stable according to the definition of the international standard IEC if, after an operating duty causing temperature rise, the temperature of the varistors elements decreases with time when the arrester is energized at specified continuous operating voltage and at specified ambient conditions [12]. In surge arresters, the ZnO varistors elements are generally located in an environment consisting of gas or solids which will limit cooling of these varistors elements when submitted to their continuous operating voltage [1].

Figure 3.1 shows the influence of ZnO temperature on the V-I characteristic. From this figure, we can see that for the same applied voltage level, any temperature rise would increase the current because of the high sensitivity to temperature of the V – I characteristic in the low conduction regime. A sort of positive feedback will occur and may cause damage to the arrester if the material heat is not dissipated. For this reason, thermal stability is one of the most important application criteria for metal oxide surge arresters, which can be analyzed by the thermal balance diagram between the energy generated or losses (P) and the heat dispersion of the housing (Q) [1, 21, 69, 70]. The thermal stability of MOSA's is affected by ambient temperature and heat dissipation capability, impulse degradation and ageing [1, 20].

To obtain thermal stability, the electrical power dissipation in the element (P) must be balanced against heat output to the environment (Q). Near the thermal equilibrium, it is possible to express the thermal dissipation capacity Q of a surge arrester as [1, 20, 71]:

$$Q = C_T \cdot (T - T_a) \quad (3.1)$$

Where:

$T$ : is the temperature of ZnO valve elements.

$T_a$ : is the ambient temperature.

$C_T$ : is the thermal dissipation factor.

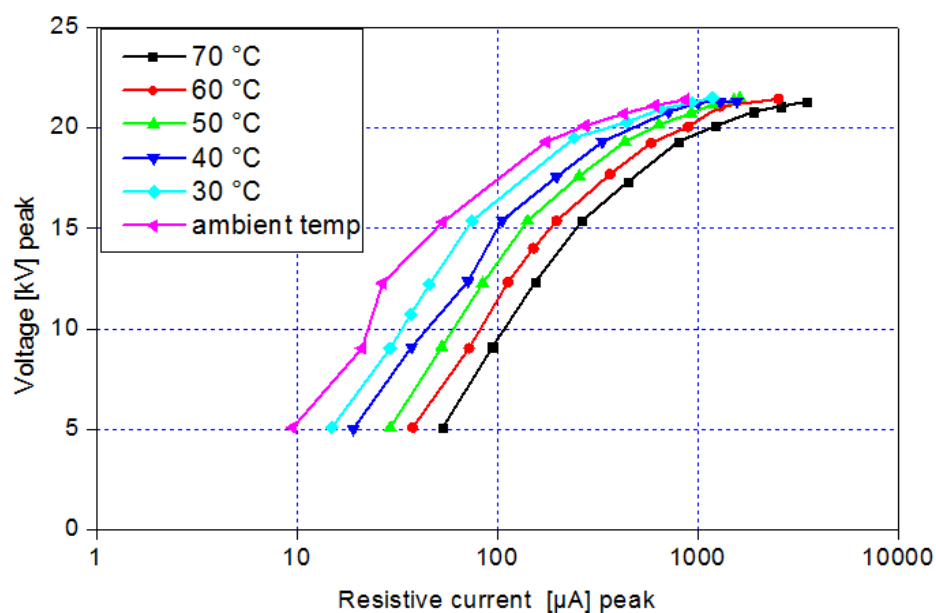


**Figure 3.1** Temperature dependence of ZnO voltage-current characteristic [1]

The heat generation,  $P$  which is voltage and material composition dependent, may be approximated by [1, 71]:

$$P = B \cdot e^{-(W_c/K_B T)} \quad (3.2)$$

Where:

$W_c$  : is the activation energy,

$K_B = 0.86 \cdot 10^{-4}$  eV/°K (Boltzmann constant),

$T$  : is the temperature of the material and  $B$  depends on the applied voltage level and the physical dimensions of the valve elements.

Both power curves ( $P$ ,  $Q$ ) have two common points of intersection (A) and (B) as shown in figure 3.2. The left one (point A) corresponds to a stable operating point; the second corresponds to an unstable operating point (point B).

To achieve thermal stability, the power generated must be balanced by the dissipated power ( $Q$ ) towards the ambient air. If  $P$  is greater than  $Q$ , zones I and III, the excess energy is stored in the ceramic, increasing its temperature. Inversely, if  $Q$  is greater than  $P$ , the temperature of the ceramic decreases.

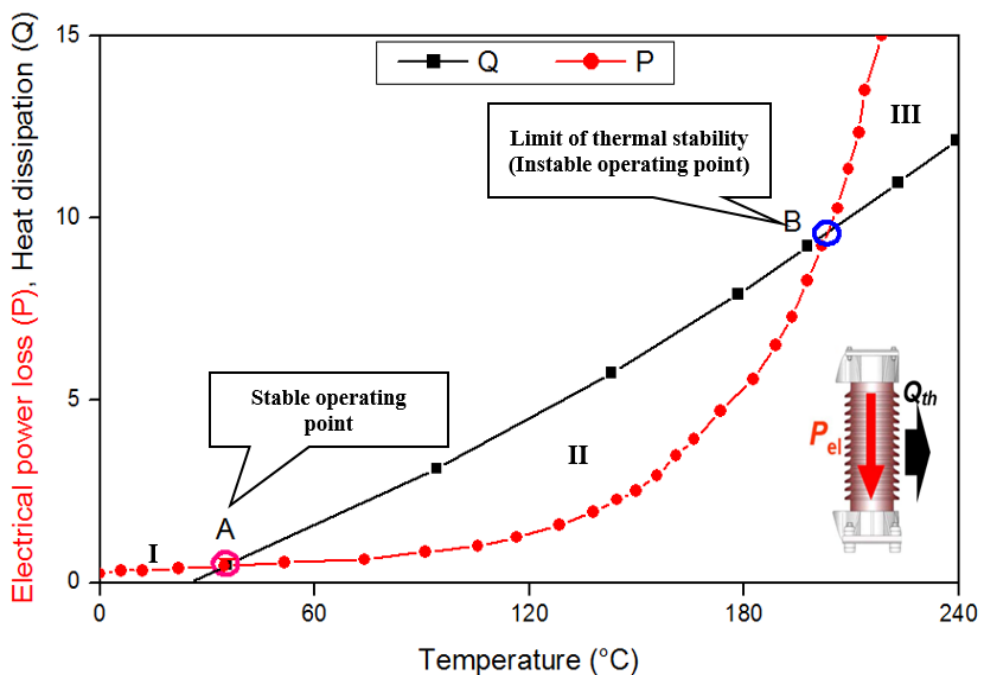


**Figure 3.2** Diagram of the thermal stability of a MOSA [20]

### 3.2.1. Thermal runaway critical condition

The critical condition of thermal runaway is evaluated analytically based on the temperature dependence and the heat loss of the arrester to ambient air. As shown above in figure 3.2, thermal runaway occurs when the lower stability point (A) moves to the upper stability point (B), so the heat dissipation curve Q is tangential to the generation curve P [1, 20].

At that instant, we can write the critical conditions:

$$P = Q \quad (3.3)$$

And

$$\frac{\partial P}{\partial T} = \frac{\partial Q}{\partial T} \quad (3.4)$$

Using equations (3.1) and (3.2), the critical values of temperature  $T_{cr}$  and power  $P_{cr}$  are:

$$T_{cr} = T_a \cdot \left( 1 + \frac{K_B T_a}{W_c^2} \cdot (W_c + 2K T_a) \right) \quad (3.5)$$

And

$$P_{cr} = 4 \frac{C_d}{D} \cdot (T_{cr} - T_a) \quad (3.6)$$

Where:

$C_d$  : is the heat dissipation coefficient [W/cm/°K], and  $D$  is the diameter of elements.

### 3.2.2. Heat dissipation capability of the housing

The heat dissipation capability (Q) of arrester directly determines the heat stability characteristics of arrester, and plays an important role in thermal balance diagram. Temperature variation is one of the main factors in the heat dissipation capability (Q) that obtains using the cooling curve of MOSA housing [21, 70]. If the absorbed energy cannot dissipate into the ambient quickly, the temperature of arresters would exceed the limiting operating temperature. The main reason for this is related to the heat flow along an arrester

column. Heat dissipation is reduced at the center of the active column. As a consequence, the temperature of the middle section of an arrester is higher than those at the ends [1].

The improvement of heat dissipation is significant for surge arresters. Improving the heat dissipation capability of the arrester means that the curve Q on figure 3.2 will be lifted to higher values; hence the thermal property of the arrester is improved. Up to six times improvement can be achieved if cooling metal fins are used [1]. An arrester's heat dissipation capability (heat flow) is determined by thermal conduction, convection and radiation [31].

### 3.3. Heat transfer

The term heat transfer is defined by the law of thermodynamics as the energy that is transported across the boundary of a thermodynamic system due to a temperature difference between the system and its surroundings [72, 73]. Heat transfer can be achieved by conduction, convection or radiation. Each one of these heat transfer processes are used for different regions of the arrester. In solid elements, the conduction plays a major role, while convection and radiation takes place in regions where air or other gaseous substances are present [31, 74].

#### 3.3.1. Conduction

Conduction is the form of heat that exists due to direct contact without movement. A temperature gradient within a substance causes a flow of energy from a hotter to colder region. These gradients can exist in solids, liquids and gases; provided there is no movement in the fluid phases, *i.e.* fluids which are not well mixed. Over time the temperature difference will reduce and approach thermal equilibrium (same temperature). Conduction occurs in a solid, liquid or gas; provided there is no bulk movement.

The following relation is well-known as Fourier's law, named after Jean Baptiste Joseph Fourier, who expressed this relation first in 1822 [72, 73]:

$$\dot{q} = -\lambda \frac{\partial T}{\partial x} \quad (3.7)$$

The sign minus (-) means that the heat flow in the direction of decreasing temperatures.

$\dot{q}$  : Heat flux [ $\text{W}/\text{m}^2$ ].

$\lambda$  : Thermal conductivity [ $\text{W}/(\text{m}\cdot^\circ\text{K})$ ].

$x$  : Direction in which there is a temperature gradient (direction of heat transfer) [m].

$\frac{\partial T}{\partial x}$ : Temperature gradient in direction of a coordinate  $x$ .

The thermal conductivity is typically highest for solids, followed by liquids and gases [72].

➤ For solids under normal conditions  $\lambda$  is approximately in the range:

$$1 \leq \lambda_{solid} \leq 450 \quad [\text{W}/(\text{m}\cdot^\circ\text{K})]$$

Metallic materials such as silver and copper at the upper end, and nonmetallic materials such as coal, glass at the lower end of the range.

➤ For liquids under normal conditions  $\lambda$  is approximately in the range:

$$0.1 \leq \lambda_{liquid} \leq 0.65 \quad [\text{W}/(\text{m}\cdot^\circ\text{K})]$$

➤ For gases under normal conditions  $\lambda$  is approximately in the range:

$$0.015 \leq \lambda_{gas} \leq 0.15 \quad [\text{W}/(\text{m}\cdot^\circ\text{K})]$$

For example, the thermal conductivity of air at atmospheric conditions is:

$$\lambda_{air} \approx 0.0246 \quad [\text{W}/(\text{m}\cdot^\circ\text{K})]$$

### 3.3.2. Convection

Convection is the transfer of heat due to the bulk movement of fluids (flow of gaseous or liquid fluids). As such convection only applies to heat transfer within a fluid or between a solid and a fluid but not the heat transfer within a solid. This heat transfer is achieved by the movement of molecules within the fluid. The heat flux  $\dot{q}$  depends on the temperature difference but also on the temperature and velocity profiles in the boundary layer. The convective heat is directed towards the lower temperature [72, 73].

Convection is governed by Newton's law of cooling [72, 73, 74]:

$$\dot{q} = h(T_S - T_0) \quad (3.8)$$

Where:

$h$  : Heat transfer Coefficient [ $\text{W}/(\text{m}^2 \cdot ^\circ\text{K})$ ].

$(T_S - T_0)$ : Temperature difference [ $^\circ\text{K}$ ], with  $T_S$  is the surface temperature and  $T_0$  is the temperature of ambient air or the temperature of another surface.

### 3.3.3. Radiation

Radiation is the transfer of energy due to electromagnetic waves when thermal energy is converted by the movement of the charges of electrons and protons in the material. When a body radiates, the energy comes from the entire depth of the body, not just the surface. Radiation does not require a temperature gradient. A person standing some distance from the source will still feel the effects of the heat, e.g. a person near a fire is heated by the fire, not by the air surrounding them. Unlike conduction or convection the energy transport from a location A to a location B by radiation is not bounded to any interlinking transport medium because electromagnetic waves can travel through a vacuum [72, 73].

The maximum emitted flux density is given by Stefan-Boltzmann's law [72, 73, 74]:

$$\dot{e} = \varepsilon \cdot \sigma \cdot T^4 \quad (3.9)$$

Where:

$\varepsilon$  : is emissivity between the side surface and the environment ( $0 \leq \varepsilon \leq 1$ ).

$\sigma = 5.67 \cdot 10^{-8}$  [ $\text{W}/(\text{m}^2 \cdot ^\circ\text{K}^4)$ ] is Stefane Boltzmann's constant.

### 3.4. Modeling of the thermal behavior of metal oxide surge arresters

The temperature distribution along the surge arresters is interesting because it influences the varistors and thus the power loss. Temperature rises caused by absorbed energy can lead to electro-thermal failure of metal oxide surge arresters. Therefore, it is necessary to analyze the electrical and thermal characteristics of arresters.

In follows, we will present the main electro-thermal models of metal oxide surge arresters existing in the literature.

In Ref [68], a simple electrical analog model of the thermodynamic behaviour of the arrester assembly has been formulated and verified by testing. The electrical equivalency is based on representing power flow (W) as current and temperature ( $^{\circ}\text{C}$ ) as voltage. The equivalent units of resistance are then  $^{\circ}\text{C}/\text{W}$  and  $(\text{W.s})/^{\circ}\text{C}$  for capacitance. Thermal energy, released within the metal oxide elements assembly, is transported to the environment by means of radiation, conduction and convection. The equivalent electrical circuit, valid for most metal oxide arrester designs, is shown in figure 3.3.

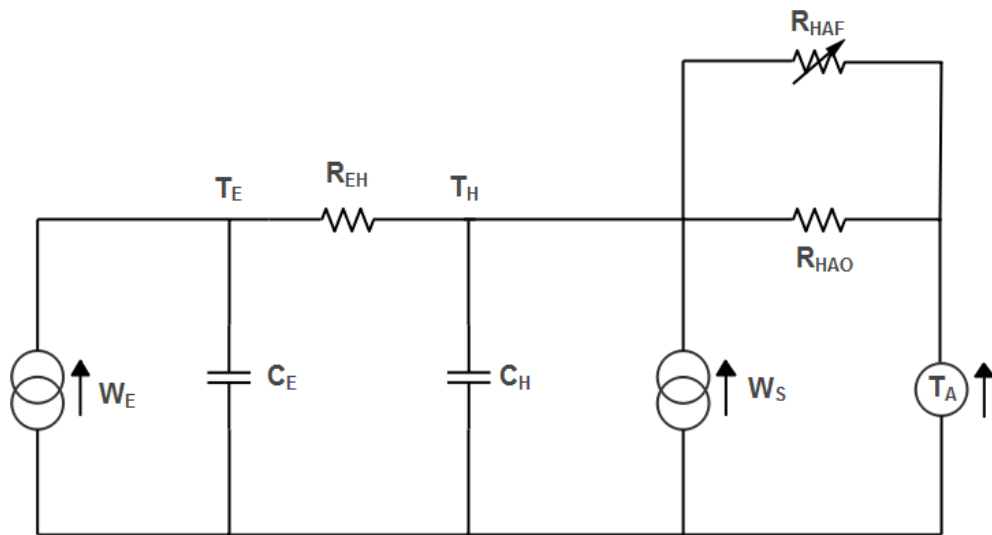


**Figure 3.3** Electrical analog circuit for the thermal parameters of MOSA [68]

$C_E, C_H$ : thermal capacities of the valve element and adjacent housing respectively ( $\text{W.s}/^{\circ}\text{C}$ )

$R_{EH}$ : thermal resistance from element to external surface of the housing ( $^{\circ}\text{C}/\text{W}$ ).

$R_{HA0}$ : thermal resistance from housing to ambient, radiation and natural convection components ( $^{\circ}\text{C}/\text{W}$ ).

$R_{HAF}$ : thermal resistance from housing to ambient, forced convection component only ( $^{\circ}\text{C}/\text{W}$ ).

$T_E$ : valve element temperature ( $^{\circ}\text{C}$ ).

$T_H$ : housing temperature ( $^{\circ}\text{C}$ ).

$T_A$ : ambient temperature ( $^{\circ}\text{C}$ ).

$W_E$ : electrical power input to valve element (W).

$W_S$ : heat input due a solar radiation (W).

This model can be used for steady-state and transient simulation of arrester performance in field or laboratory conditions. Model parameters can be determined analytically from physical dimensions of a particular arrester unit or derived by experimental measurements on actual units. The analytical method yields values which are in good agreement with experimentally derived figures. In steady-state,  $C_E$  and  $C_H$  are not included in the analog circuit.

Energy input to the valve element, resulting from lightning and switching surge discharges and temporary overvoltage (high magnitude, short duration), be treated adiabatically. The author has made extensive use of the following empirical relationship between valve element voltage and current ( $V, I$ ) for this application:

$$V = \frac{C_1}{C_2 - \ln(I)} + R \cdot I \quad (3.10)$$

Where:  $C_1, C_2, R$ , are empirical constants determined from test data.

In steady-state, the 60 Hz power input to the valve element has been modelled using a look-up table of 160 experimentally derived points. This system can be used to determine the 60 Hz power input ( $W_E$ ) into a typical undamaged element under various operating or long-term overvoltage conditions.

Also, the power input density to the arrester surface is approximately 60 to 75% of maximum solar radiation intensity. Hence, the energy input due to solar radiation ( $W_s$  in [W]) can be expressed:

$$W_s = 0.068 \cdot D_{max} \cdot h_v \quad (3.11)$$

Where:

$h_v$ : element height, and  $D_{max}$  is the maximum housing diameter.

Assuming that power density at the housing surface is uniform, temperature rise of the

housing ( $\Delta T_{HS}$ ) can be calculated:

$$\Delta T_{HS} = R_{HAO} \cdot W_S \quad (3.12)$$

The heat capacity of any particular component ( $C_C$ ) or an arrester can be determined as follows:

$$C_C = V_C \cdot (C_O - \alpha_C \cdot T) \quad [J/^\circ C] \quad (3.13)$$

Where:

$V_C$  : Volume of arrester component ( $\text{cm}^3$ ).

$T$  : Temperature of component ( $^\circ\text{C}$ ).

$C_O$  : Specific Heat [ $\text{J}/(\text{cm}^3 \cdot ^\circ\text{C})$ ].

$\alpha_C$  : Temperature coefficient of specific heat [ $\text{J}/(\text{cm}^3 \cdot ^\circ\text{C}^2)$ ].

The energy absorption capability of a metal oxide surge arrester is limited by the temperature of its elements. To predict this temperature, a computer model can be a valuable tool. Petit et al [75] has provides an experimental method to determine a coupled electrothermal model of metal oxide varistor elements (Fig. 3.4).

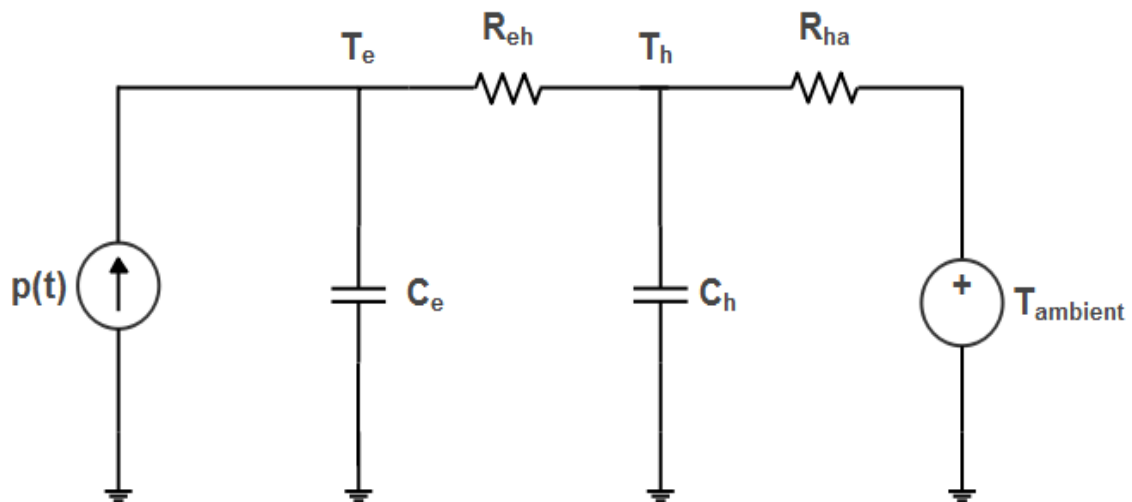


**Figure 3.4** Electrothermal model of a MOSA [75]

Where:

$T_e$  and  $T_h$ : the temperature of the elements and housing respectively.

$C_e, C_h$ : the thermal capacitivities of the elements and of the housing;

$R_{eh}$  and  $R_{ha}$ : the thermal resistances between element and housing, and between housing and ambient;

$p(t)$ : is the heat source.

Firstly, electrical heat production from the varistor elements was determined by computing watt-losses ( $V \cdot I$ ) from voltage-current-temperature characteristic of the studied arrester. Next, a single high-energy discharge based on linear system analysis and least-squares minimization curve fitting was then used to determine the four (4) values of the thermal model.

Solving the circuit shown in figure. 3.4 for an input power  $p(t)$ , gives the following equation for the varistor element temperature ( $T_e$ ) in function of time:

$$T_e(t) = k_1 \cdot e^{r_1 t} + k_2 \cdot e^{r_2 t} + T_a \quad (3.14)$$

Where:

$T_a$ : is the ambient temperature, and  $k_1, k_2, r_1, r_2$  are the constants of this double exponential function.

By measuring the temperature of the elements at different points in time, it is possible to find by a least-squares minimization method, the four (4) parameters  $k_1, k_2, r_1$  and  $r_2$  ( $T_a$  being known) that best fit the experimental data. Solving these four equations describing  $k_1, k_2, r_1, r_2$  in terms of  $C_e, C_h, R_{eh}, R_{ha}$ , we find:

$$C_e = \frac{P}{k_1 + k_2} \quad (3.15)$$

$$C_h = \frac{-P \cdot (k_1 \cdot r_1 + k_2 \cdot r_2)^2}{(k_1 + k_2) \cdot k_1 \cdot k_2 \cdot (r_1 - r_2)(r_2 - r_1)} \quad (3.16)$$

$$R_{eh} = \frac{-(k_1 + k_2)^2}{P \cdot (k_1 \cdot r_1 + k_2 \cdot r_2)} \quad (3.17)$$

$$R_{ha} = \frac{k_1 \cdot k_2 \cdot (r_1 - r_2)(r_2 - r_1)}{P \cdot r_1 \cdot r_1 \cdot (k_1 \cdot r_1 + k_2 \cdot r_2)} \quad (3.18)$$

The precision of the complete electro-thermal model was then quantified by a sensitivity analysis. According to the individual parameter study, the most critical value that must be measured with high precision in the laboratory is the voltage parameter, which sensitivity is mainly affected by extreme non-linearity of the metal oxide varistor elements.

J.F. Lara and J.C. Montenegro [76] studied the thermal behavior of metal oxide surge arresters. An electrothermal model illustrated in the figure 3.5 developed by M.V Lat [68] was used.

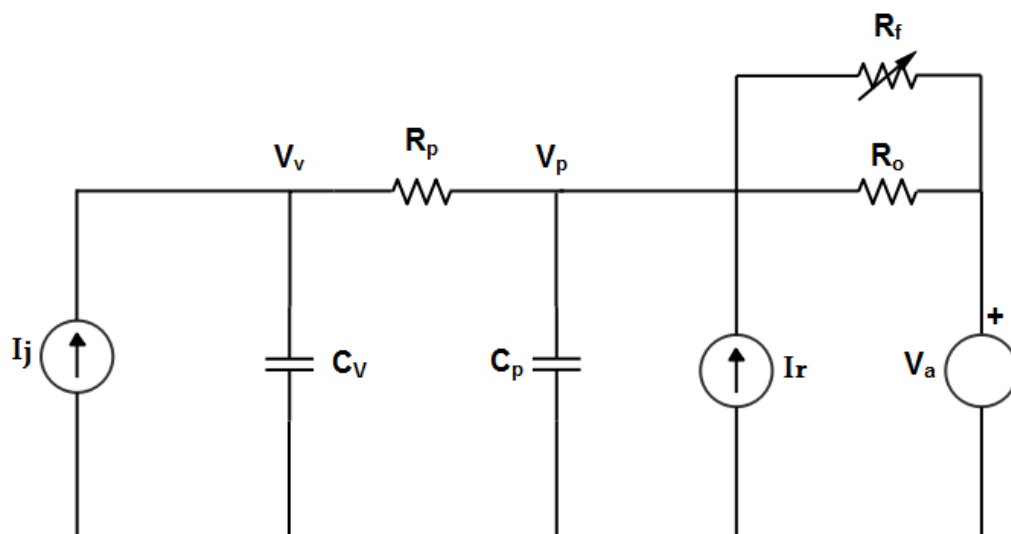


**Figure 3.5** Electrothermal model developed by M.V Lat [76]

With:

Input variables:

$I_j$ : Represents the heat source applied to the elements (Electrical power input).

$I_r$ : Represents the heating effect of the sun (solar radiation). In the experimental stage, solar radiation will not be used as input.

$V_a$ : Represents the ambient temperature.

Output variables:

$V_v$ : Varistor Temperature

$V_p$ : Housing Temperature.

Parameters to be identified:

$C_v$ : Varistor thermal capacity.

$C_p$ : Housing Thermal capacity.

$R_p$ : Housing thermal resistance.

$R_o$ : Thermal resistance from housing to ambient, due to radiation and natural convection.

$R_f$ : Thermal resistance from housing to ambient due to forced convection.

For the identification of these parameters, an autoregressive mathematical model was used. The input parameters are known ( $I_j$ ,  $I_r$ , and  $V_a$ ). Therefore, the values used as inputs are the ones to be used during the experiments. The current impulse is converted into its equivalent energy impulse by  $E = I.V.t$  joules with  $t = 28 \mu \text{ sec}$ ,  $V=8 \text{ kV}$  and  $I=5 \text{ kA}$ , to obtain an energy impulse  $E=1.12 \text{ kJ}$ .

The ambient temperature is estimated at  $25^\circ \text{ C}$ . The output variables ( $V_v$ ,  $V_p$ ) are measured during laboratory tests by the temperature telemetry technique. The studied surge arrester is subjected to a voltage of  $8 \text{ kV}$  and a pulse current of  $5 \text{ kA}$  ( $28 \text{ micro seconds}$ ). The temperature of the varistor and the envelope was taken every minute.

In Ref [77], an electro-thermal modeling procedure for a metal oxide varistor (MOV) has been proposed and investigated. The proposed modeling concept for the electro-thermal behavior of MOV is shown in figure 3.6.

The test voltage ( $V$ ), together with the current pulse profile ( $I$ ) will represent the inputs to the power loss model, which will calculate the total losses generated by the varistor under the given test conditions. Then, the local ambient temperature ( $T_{a,local}$ ) and the power losses ( $P_{loss}$ ) are included into the thermal model, and translated to the temperature of the varistor.

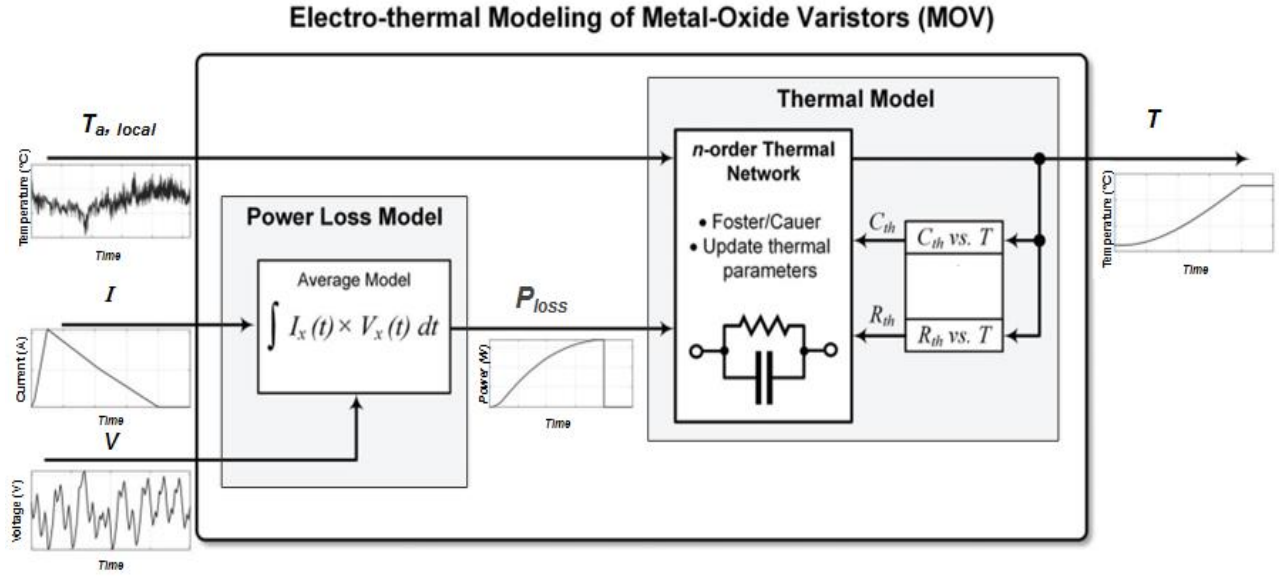


**Figure 3.6** Generic electro-thermal modeling procedure for MOV [77]

Thus, the following equation can be utilized:

$$P_{loss} = \frac{1}{T_{pulse}} \int_{t_0}^{t_1} v(t) \cdot i(t) dt \quad (3.19)$$

Where:

$T_{pulse}$  : is the current pulse duration,  $t_0$  is the start time of the current pulse,  $t_1$  is the end time of the current pulse,

$v(t)$  : is the instantaneous voltage drop across the varistor, and  $i(t)$  is the instantaneous surge current pulse.

Additionally, the resulting varistor temperature ( $T$ ) will represent a feedback to the thermal model, in order to characterize the temperature dependency of the ZnO compound thermal resistance and thermal capacitance (according to the thermal properties presented in figure 3.7 and figure 3.8).

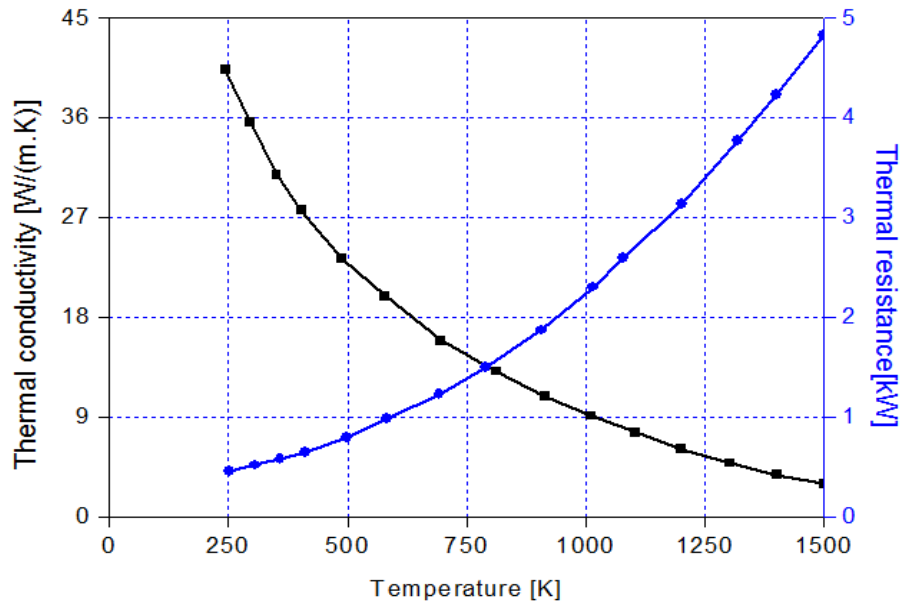


**Figure 3.7** Temperature dependency of ZnO thermal conductivity and thermal resistance [77]

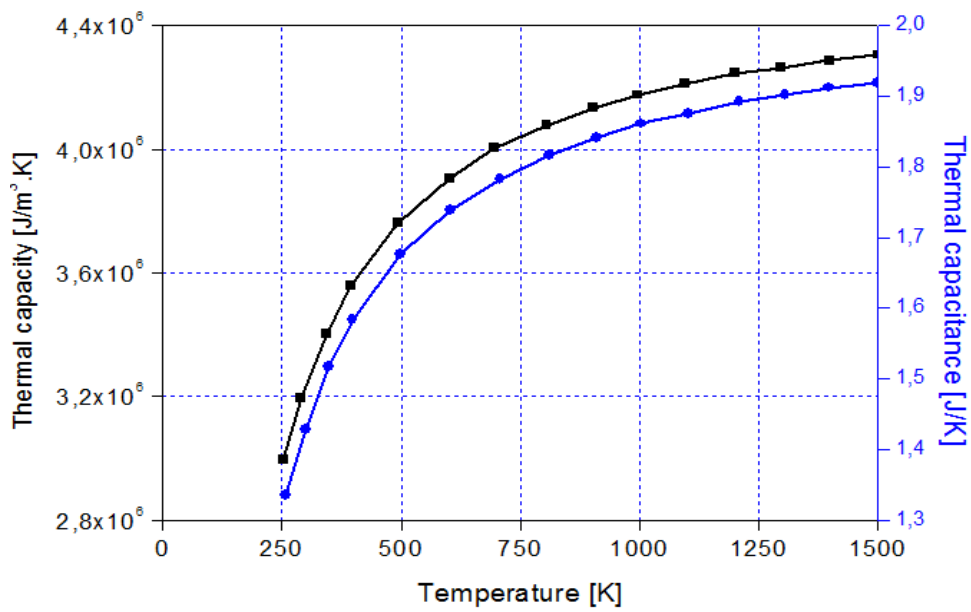


**Figure 3.8** Temperature dependency of ZnO specific heat and thermal capacitance [77]

The thermal resistance can be calculated according to the following equation:

$$R_{th} = \frac{t}{k_{th}} \quad (3.20)$$

Where:

$t$  : is the thickness of the varistor, and  $k_{th}$  is the thermal conductivity.

Similarly, the thermal capacitance is computed based on the formula given below:

$$C_{th} = q_{th} \cdot V \quad (3.21)$$

Where:

$V$  : is the volume of the varistor, and  $q_{th}$  is the thermal capacity.

During the heating phase, the thermal resistance and thermal capacitance are updated continuously according to their temperature dependency curves shown in figure 3.7 and figure 3.8, which are included as a look-up table.

On the other hand, during the cool-down phase of the varistor, the thermal network is built based on the empirical thermal resistance ( $R_{th,exp}$ ) and capacitance ( $C_{th,exp}$ ) values, which have been observed and fitted throughout experimental testing.

In order to study the electric and thermal characteristics of MOSAs under power frequency voltage, an improved electro-thermal model of a MOSA has been proposed [67] as shown in figure 3.9. The proposed electro thermal-model can be divided into an electric model (figure 3.10) and a thermal model (figure 3.11). This electro-thermal model can be used to predict not only the voltage and leakage current, but also the temperature characteristics of a MOSA.

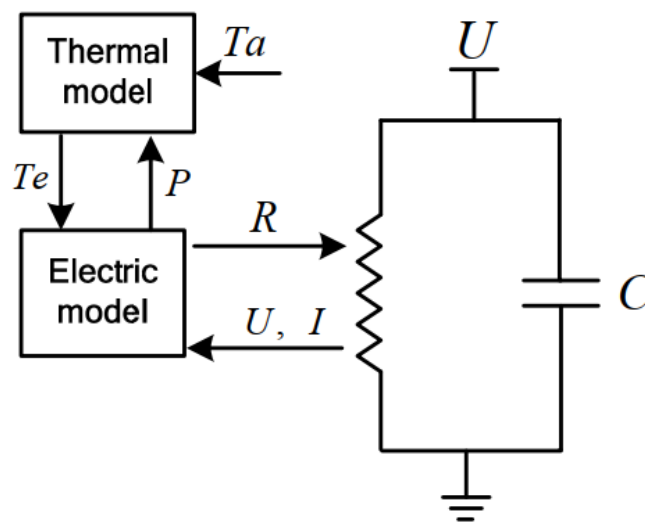


**Figure 3.9** Diagram of the electrothermal MOSA model [67]

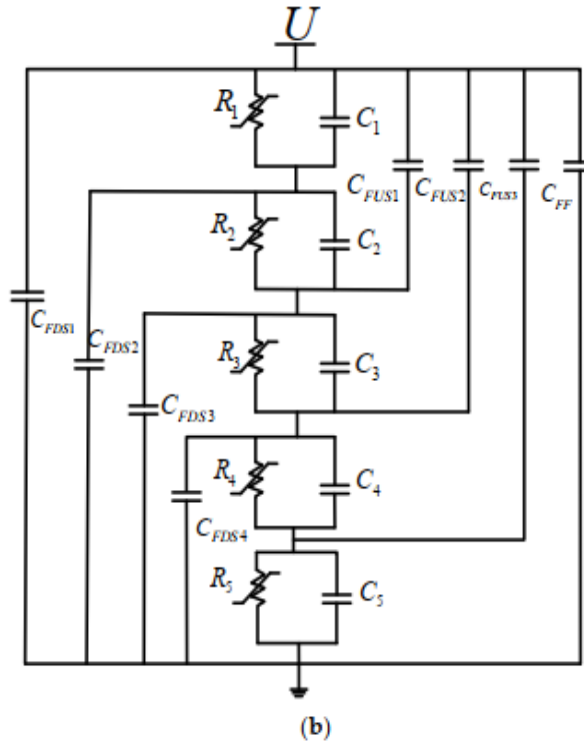


**Figure 3.10** Conventional electric model for MOSA [67]

Five ZnO varistors are contained in the MOSA;  $R$ ,  $R_1$  to  $R_5$  represent the resistances of each varistor.  $C$ ,  $C_1$  to  $C_5$  represent the stray capacitance of each varistor.  $C_{FF}$  is the capacitance between the upper and lower flanges,  $C_{FUSi}$  ( $i = 1, 2, 3$ ) are the upper flange stray capacitances with spacers and aluminum sheets, and  $C_{FDSi}$  ( $i = 1, 2, 3, 4$ ) are the stray capacitances among the lower flange and spacers and aluminum sheets.

In this paper, finite element methods are used to calculate the stray capacitances in ANSOFT Maxwell software.

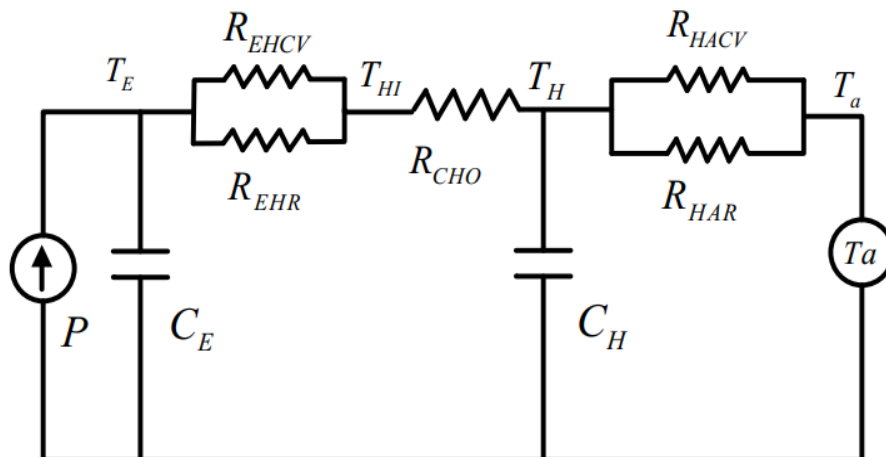


**Figure 3.11** Thermal model of MOSA [67]

With:

$P$  is the power loss obtained from the electric model,  $T_a$  is the ambient temperature,  $T_E$  is the varistor temperature,  $T_{HI}$  is the temperature of the inner surface of the arrester housing,  $T_H$  is the temperature of the polymer housing,  $R_{CHO}$  is the thermal resistor between the varistor and housing,  $R_{EHR}$  and  $R_{EHCV}$  are the radiation and conduction thermal resistances between the ZnO varistors and housing,  $R_{HACV}$  and  $R_{HAR}$  are the conduction and radiation thermal resistance between the housing and ambient, and  $C_E$  and  $C_H$  are the thermal capacitance of the ZnO varistor and housing.

According to the equations given by Lat [68], the thermal resistance and capacitance at different times in figure 3.11 can be calculated.

- Firstly, in order to build the electric part of the electro-thermal model, experiments were carried out to obtain the voltage–current–temperature (V–I–T) characteristics of the tested ZnO varistors. According to the experimental results, the electric model of the tested ZnO varistors considering the temperature effects is built. Using temperature and applied voltage as input data, the leakage current flowing through the MOSA can be calculated using the artificial neural network (ANN) method.
- Secondly, a thermal resistance circuit model is introduced to build the thermal part of the model. Using power loss and ambient temperature as input data, the temperature of the MOSA is calculated, which is used as the input data of the electric model.

The temperature of the varistors can be obtained as the output of the thermal model. The temperature of the arresters is used as the input data of the electric part of the model consequently.

Resonant overvoltages caused by transformer energization in relatively weak systems, especially during power system restoration, are investigated in [69]. These transient overvoltages may result in failures, especially for surge arresters. The temperature rise of surge arresters is proposed as an index to diagnose a harmonic resonance case. An appropriate electrothermal model for metal–oxide surge arresters is developed using the thermal model and proposed combined electrical model.

A complete electrothermal model of MOSA is the combination of two parts:

- 1) An electrical model to obtain the power dissipated inside the MOSA
- 2) A thermal model to obtain its temperature rise.

For this purpose, a combined electric model has been proposed, which uses the temperature-dependent model for the low current region of characteristic V-I, and the IEEE model for the high current region of curve V-I at the same time than the equivalent circuit of the proposed electrothermal model.

The IEEE electrical model for the surge arrester is shown in figure 3.12.

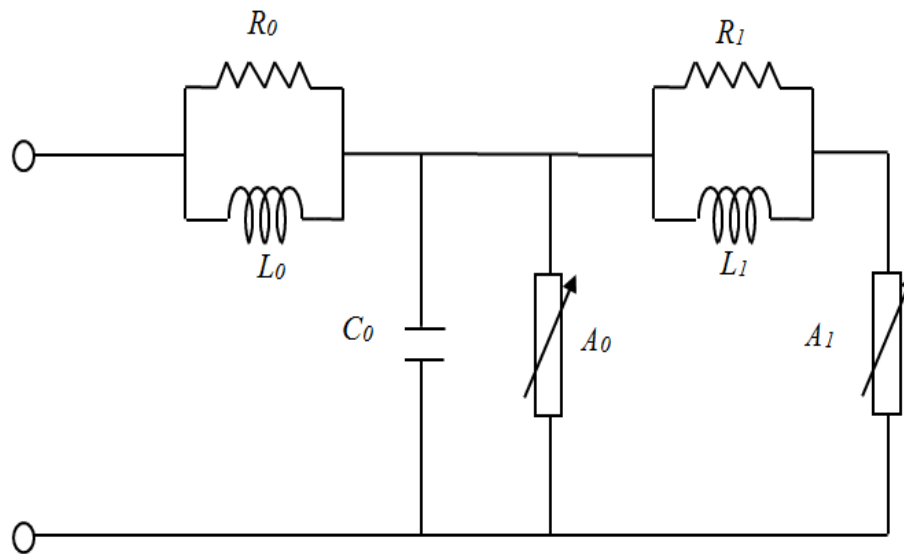


**Figure 3.12** Modèle IEEE du parafoudre [69]

$$\begin{aligned}
 L_0 &= 0.2 \frac{d}{n} \text{ (}\mu\text{H)}, & R_0 &= 100 \frac{d}{n} \text{ (}\Omega), & L_{01} &= 15 \frac{d}{n} \text{ (}\mu\text{H)}, \\
 R_1 &= 65 \frac{d}{n} \text{ (}\Omega), & C_0 &= 100 \frac{d}{n} \text{ (pF)} & & 
 \end{aligned} \tag{3.22}$$

Where:

$d$  : is the height of the arrester in meters

$n$  : is the number of parallel columns of MO disks.

The electrical model that is temperature dependent is presented as follows:

$$J(F) = 2F \left\{ 2A_1 + A_2 \exp\left(\frac{a_1}{T}\right) \cdot \left[ 1 - \tanh\left(a_2 + \frac{a_3}{T} - \frac{a_4}{T}\right) \right] \right\}^{-1} \quad (3.23)$$

Where:

$J$ : is the current density in  $[A/cm^2]$

$F$ : is the voltage gradient  $[V/cm^2]$

$A_1=1$ ;  $A_2=0.7$ ;  $a_1 = 8000$ ;  $a_2 = 13$ ;  $a_3 = 4004$ ;  $a_4 = 38235$

For the thermal model, the analog model of M.V Lat [68] was used in this paper, as shown in figure 3.13.

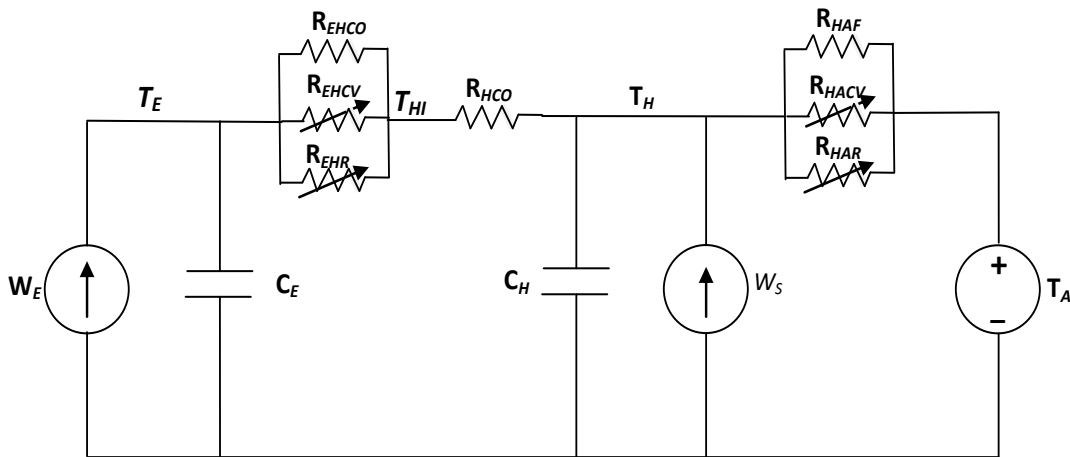


**Figure 3.13** Electrical analog circuit for the thermal model of MOSA [69].

Where:

$T_E$ ,  $T_{HI}$ ,  $T_H$  and  $T_A$ : are the temperature of element, internal, and external surface of the housing and ambient, respectively  $[^\circ C]$ .

$W_E$ ,  $W_S$ : are the electrical and solar radiation power inputs, respectively.

$C_E$ ,  $C_H$ : are the thermal capacities of the elements and housing, respectively  $[J/^\circ C]$ .

$R_{HAF}$ ,  $R_{HACV}$ ,  $R_{HAR}$ ,  $R_{HCO}$ ,  $R_{EHCV}$ ,  $R_{EHR}$ : are the thermal resistances  $[^\circ C/W]$ , and they calculated at a fixed temperature [68].

In steady state,  $C_E$  and  $C_H$ , can be neglected and omitted.

A thermal model of the 60 kV polymer metal oxide surge arrester for steady state condition only has been adopted by S. Likitha et al [66] represented by an electrical analogous circuit made of resistance as shown in figure 3.14.

The power loss was calculated by an electrical model and it is used as input to the thermal model. The electrical model is obtained by conducting experiments on a representative ZnO element at various voltages and temperatures which yields Voltage-Current-Temperature (V-I-T) and Power loss-Voltage-Temperature (P-V-T) characteristics. A data bank was established from the measured values of resistive leakage current and power loss. These values are fit into mathematical equations to facilitate prediction of the resistive leakage current and the power loss at any required voltage and temperature other than the ones considered in the experiments.

The thermal model is solved iteratively at a given electrical power loss (input), ambient and element temperature in order to obtain steady state polymeric housing temperatures of MOSA. The input to the thermal resistance circuit is the power loss obtained from the electrical model with fixed ambient temperature. The initial thermal resistance values are calculated using an initial estimate for housing temperature, known element and ambient temperatures. It depends on the physical dimensions and material used for the arrester.

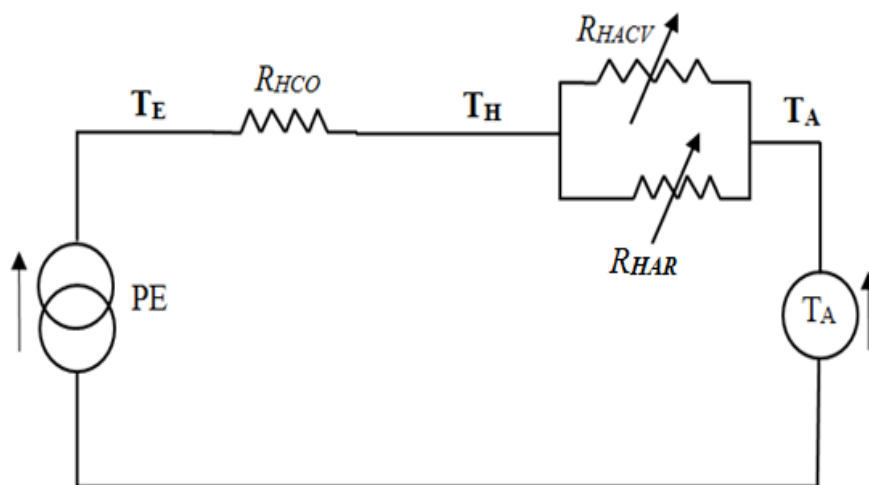


**Figure 3.14** Electrical analogous circuit at steady state [66]

The stable operating and thermal instability points have been successfully estimated for 60kV gapless polymer metal oxide surge arrester at various applied voltages and ambient temperatures using power Input-Heat loss verses element temperature curve based on electro-thermal model.

### **3.5. Conclusion**

In this chapter we have presented the main aspects that characterize the thermal behavior of metal oxide surge arresters, such as thermal stability, which can be analyzed by the thermal balance diagram between the absorbed energy ( $P$ ) and heat dissipation of the housing ( $Q$ ). This latter is directly determined the heat stability characteristics of arrester.

Also we have presented the three heat transfer processes, by conduction, convection and radiation.

Furthermore, we have presented the main electrothermal models of metal oxide surge arresters existing in the literature. For the thermal model, the electrical analog circuit of M.V Lat [68] was adopted. These models represent a good tool for predicting the thermal behavior of surge arresters and describing the temperature evolution of the varistors elements and housing as a function of the power absorbed.

# **CHAPTER 4**

## **GRADING RING DESIGN OPTIMIZATION FOR IMPROVED ELECTRIC FIELD DISTRIBUTION**

---

# **GRADING RING DESIGN OPTIMIZATION FOR IMPROVED ELECTRIC FIELD DISTRIBUTION**

---

## **4.1. Introduction**

Metal oxide surge arrester is the most important devices for power system protection against switching and lightning over-voltages; it is installed closely to the equipment being protected from rapid surge current [55]. Today, installed surge arresters are almost nonlinear metal oxide arresters without gaps due to high-energy absorption capability and highly nonlinear V-I characteristic of ZnO varistors.

Ageing of metal oxide surge arrester is mainly affected by the high electric stress near the high voltage (HV) electrode. It has been observed that the distribution of potential and E-field along an arrester under normal operating conditions is non-uniform [9]. This non-uniformity should be kept to a minimum in order to avoid damage the upper parts of the arresters with the ZnO discs placed near HV electrode are more stressed than the remaining discs by excessive electric fields and hence thermal stresses leading to faster thermal ageing of these highly stressed discs [1, 11].

The distribution of potential and E-field along an arrester can be improved by installing grading ring at the top of the arrester [1]. Grading ring dimensions need to be optimized, for this purpose, the effect of grading ring geometrical parameters is investigated in order to achieve a more uniform electric field and potential distribution.

## **4.2. Grading ring application**

As definition, grading ring is a metal device usually circular in shape, installed to modify electrostatically the potential distribution along the surge arrester [12]. Surge arresters of system voltages about 145 kV and over and if their length exceeds 1.5 to 2

meters, and usually for arresters made up of several units, grading rings are absolutely essential with one or more metallic rings suspended down from the top of the arrester [27, 28, 29]. For very high system voltages, additional rings are used to prevent external corona from the upper metallic flange and from the line terminal [29].

E-field distribution along varistors column is an important factor that needs to be taken into account during designing of metal oxide surge arresters. Recently, finite element method (FEM) has been increasingly employed in all fields of engineering to aid in simulating various practical problems, including electric field analysis [78, 79, 80]. For this reason, FEM software's such as Maxwell [13, 14] and FEMM 4.2 [15] were used to investigate the design of the grading ring for a MOSA.

In [13], the influence of grading ring design parameters and spacer numbers on potential distribution and electric field in 230 kV metal oxide surge arrester was studied. Maxwell software was applied to calculate these latter, and then the equivalent circuit of the surge arrester has been simulated in EMTP/ATP software for evaluation of leakage current. The variation of grading ring design parameters affects the total leakage current and its components. Grading ring increases capacitive leakage current component but decreases resistive current component.

He et al [16] applied 3D finite element method (FEM) and circuit-analytic method to analyze and improve the potential distribution of the 1000-kV MOSA. The influences of the grading ring and mounting height of the MOSA on the potential distribution are also discussed.

Grading ring height was optimized between 75 and 86% of the total arrester length [11, 17]. It is clear that its effectiveness depends on its relative position. In addition, the maximum value of the distributed potential will decrease by increasing the grading ring diameter. It was found that placing spacers at the bottom of the arrester give a minimum stress, compared to spacers placed at the top.

The E-field and potential distribution of a 624 kV rated voltage polymeric surge arrester with varying the grading ring parameters was study such as ring diameter, tube diameter, ring position and height of pedestal [10]. Acceptable value for the potential

deviation of 12% to 15% is considered for the grading ring parameters optimization. In this study, the commercially available 2D Elecnet software based on Finite Element Method (FEM) was employed.

He et al have proposed a combined method of electrical field and electric circuit in order to analyze potential distribution of suspended-type metal oxide surge arresters [18]. A charge simulation method and matrix transformations were used to obtain the equivalent electric circuit. Potential distribution along the ZnO varistor column of a 220 kV surge arrester without and with the grading ring was also examined. After installing grading ring, the potential distribution has been improved and the maximum voltage ratio is reduced from 1.24 without ring to 1.04.

According to these studies cited previously, they have not optimized the dimensions of grading ring of the arrester's by artificial intelligence methods. Only, investigations were performed to see the effect of different ring parameters on potential distribution and electric field.

Otherwise, several studies have been carried out to optimize the corona ring parameters in order to control the electric field stress on the insulator surface [81, 82, 83, 84, 85]. Corona rings are employed in insulator to avoid corona discharge activity caused by high electric stress near the end fittings [81, 86]. Artificial intelligence methods such as PSO, artificial fish swarm algorithm (AFSA), response surface methodology (RSM) and others methods have been performed for the optimization of the corona ring parameters [81, 85, 86].

### **4.3. Modeling detail of the MOSA**

The structure of the studied 220 kV polymeric metal oxide surge arrester is shown in figure 4.1. The arrester considered for this study is made of two 110 kV MOSA unites in series with a total height about 2 m. The arresters unit 110 kV consists of 32 ZnO varistors having a diameter of 71 mm and thickness of 20.5 mm. A fiberglass reinforced plastic (FRP) with their inner and outer diameters are 73 and 86 mm. The maximum outer diameter of the shed is 202 mm, and the diameter of the silicone rubber cylinder is 94 mm. All metal parts in the studied arrester are made of aluminum alloy [21].

3D model of studied polymeric metal oxide surge arrester was designed by the Computer Aided Design (AutoCAD) software package. This model was imported into COMSOL Multiphysics.

3D finite element method was employed via software COMSOL MULTIPHYSICS<sup>®</sup> 4.3 to calculate the E-field and potential distribution. We simulated the polymeric surge arrester under dry and clean conditions. The high voltage (HV) electrode is carried to a potential of  $(220 \cdot \sqrt{2})/\sqrt{3}$  kV while the lower electrode carried to a null potential (0 V).

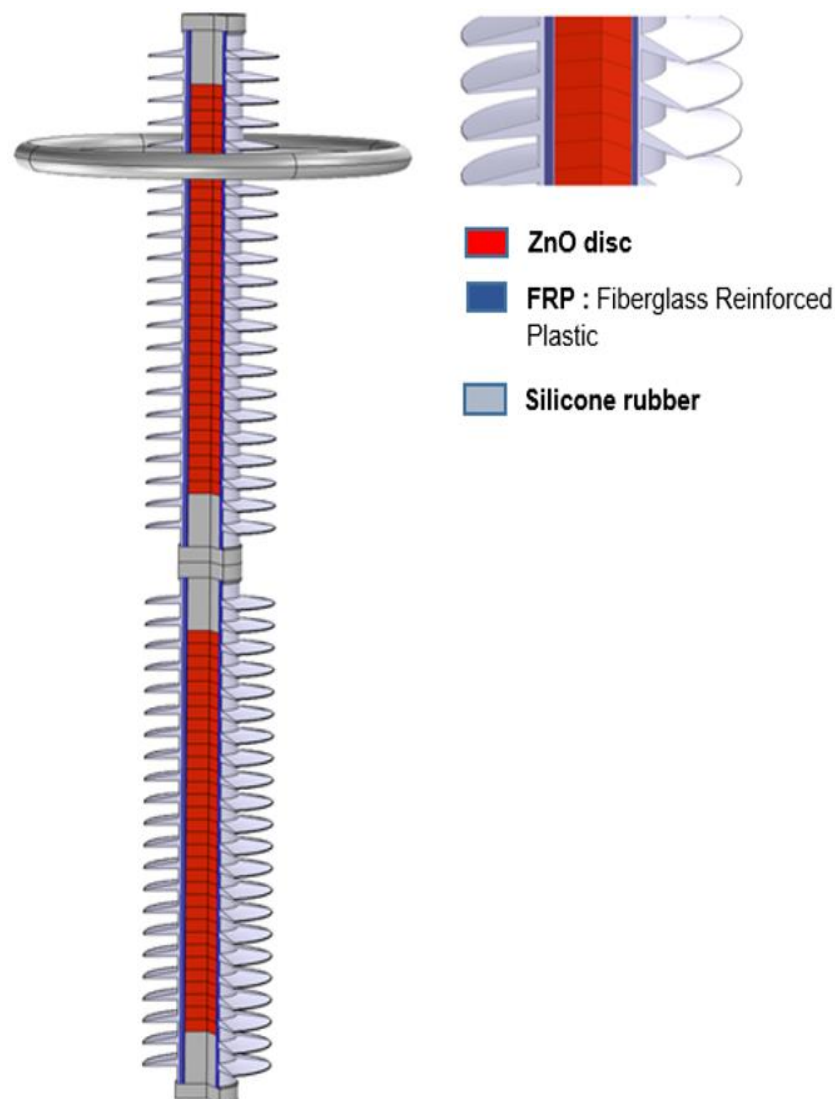


**Figure 4.1** Structure of the studied 220 kV polymeric metal oxide surge arrester

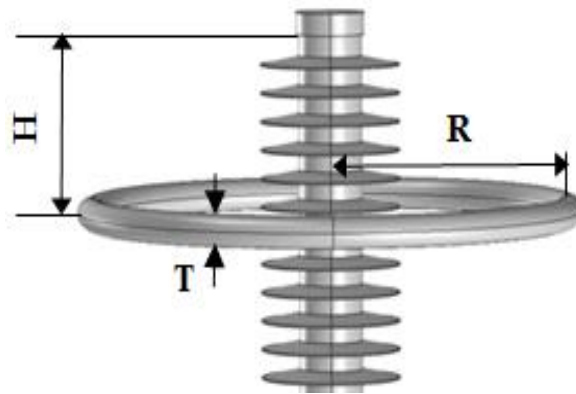


**Figure 4.2** Structural parameters of grading ring

**Table 4.1** Grading ring dimensions for 245 kV surge arresters

Grading ring dimensions	H [mm]	R [mm]	T [mm]
Ref [87]	160	200	/
Ref [88]	381	320	48
Ref [13]	1724*	425	65
Ref [89]	800	400	/
Ref [11]	80% $H^*_{\text{arrester}}$	/	100
Ref [17]	75% $H^*_{\text{arrester}}$	400	/

\*: the ring position was calculated from bottom electrode.

The electric field along the central axis of the arrester particularly close to the energized end fittings in the top unit of arrester must be minimized, for this purpose three structural parameters of a single grading ring are considered (Fig. 4.2):

- ✓ The position of the grading ring from HV electrode (H).
- ✓ The grading ring radius (R).
- ✓ The thickness of the grading ring tube (T).

Grading ring dimensions differ from a manufacturer to another. Table 4.1 summarizes some used rings and their dimensions for 245 kV surge arresters.

Therefore, we choose three values for each parameter (H, R, T). Grading ring parameters to be studied and their variation ranges are indicated in Table 4.2.

**Table 4.2** Grading ring parameters

Parameters	H [mm]	R [mm]	T [mm]
	0	200	20
<b>Variation ranges</b>	250	300	50
	500	400	80

In addition, there are no standards for the design and the placement of the grading rings by manufacturers. According to the author of the reference [27, 28], a grading ring should be installed in quarter of the total arrester length from top in order to achieve an acceptable axial distribution of the electric potential, power losses and temperatures.

The dry arc distance is reduced if the position of the ring from end (H) increased over 500 mm, this distance is related to total length of the metal oxide surge arrester. It is the distance to respect in order to avoid arcing. According to reference [90], the arc distance must be greater than 1.10 m for a voltage of 225 kV. For this reason, we choose three positions of grading ring from HV electrode: H (0, 250 and 500 mm).

To avoid any contact between the shed and the ring, the inner radius of ring must be superior to the larger shed radius of 101 mm. Three variation ranges are chosen (200, 300 and 400 mm). In this study, we note that the increase of the ring radius beyond 400 mm has practically no effect on the maximum E-field.

Three ring tube thickness variation ranges are chosen (20, 50 and 80 mm). We note that low thickness leads to high E-field. The excessive increasing of tube thickness beyond 80 mm is not economical, and makes the ring more bulky and is subjected to mechanical stresses [13, 14, 86] .

In order to reduce the number and the simulations time performed to optimize the grading ring parameters, an optimal design requires a smaller number of simulations is adopted based on the model L9 of Taguchi. A combined method based on 3D-FEM and Taguchi design is opted in order to obtain the objective function .The optimization problem

is achieved by minimizing the electric field using a BAT algorithm.

#### **4.3.1. Effects of air box size and mesh type on the electric field distribution**

The air box around the designed arrester was also drawn to observe the electric field distribution surrounding the test object. The chosen size of the air box around the studied arrester having a height about  $1.5\times$  the total height of the arrester [12].

After assembling the full geometry, material properties were assigned to each domain, also boundary conditions in the geometry model, and the model was meshed into smaller elements for effective computation. The size of the mesh elements has substantial effect on the simulation time and also to ensure the accuracy of the calculation. Therefore, the influence of mesh size was investigated [91]. Finer mesh elements were adopted, and applied on the all area with their tetrahedron shape. Because the potential is concentrated in the HV electrode and the varistors near this electrode, as well as the grading ring. Hence, almost all areas are important for our study [39, 92].

#### **4.4. Taguchi design**

Taguchi design is a statistical method developed by the Japanese researcher Taguchi. Initially it was developed for improving the quality of goods manufactured (manufacturing process development), later its application was expanded to many other fields in engineering, such as biotechnology etc [93, 94].

Taguchi design is considered as a statistical method for modeling of problems in which different variables affect the desired response. It allows determining an appropriate approximation function representing the relationship between the response and independent variables [81, 94, 95, 96].

Taguchi method is one of the best experimental methodologies used to find the minimum number of experiments to be performed within the permissible limit of factors and levels. It is a method of designing experiments, which requires only a fraction of the full factorial combination. The factors are physical variables input, modifiable by the experimenter and influence the response variations. With the plans of experiments, we obtain the maximum information's with the minimum of experiences. Thus the marriage of design of

experiments with optimization of control parameters to obtain best results is achieved in the Taguchi Method.

In this thesis, we have three parameters called factors (H, R, T), each parameter has three values (variation ranges or called levels).

The obtained test data were analyzed by model L9 of Taguchi. It is necessary to respect the distribution of the nine experimentations (nine simulations) according to the studied variables and their variation ranges according to the plan L9 of Taguchi as shown in Table 4.3. This model was extracted from Minitab, as it is also exists in the literature. The model L9 of Taguchi must consist of three parameters (H, R, T), each parameter with three ranges of variations. Taguchi model in combination with FEM will be used to obtain the objective function.

The variation ranges (or levels) of the factors to be included for the tests were chosen by the searchers. In our study, these levels were chosen based on the constraints discussed above. Each factor has 3 levels (1, 2, 3) as shown in Table 4.3.

**Table 4.3** Plan of Taguchi

<b>Parameters (or Factors)</b>				
	<b>H</b>		<b>R</b>	<b>T</b>
<b>Variation ranges</b>	1		1	1
	1		2	2
	1		3	3
	2		1	2
	2		2	3
	2		3	1
	3		1	3
	3		2	1
	3		3	2

## 4.5. BAT ALGORITHM

Metaheuristic algorithms including evolutionary and swarm intelligence algorithms are now becoming powerful methods for solving many difficult optimization problems. The vast majority of heuristic and metaheuristic algorithms have been derived from the behaviour of biological systems and/or physical systems in nature [97, 98].

Bat algorithm (BA) is a recent swarm-intelligence-based metaheuristic algorithm. It has been proposed by Yang in 2010 [97]. It is a recent metaheuristic optimization algorithm inspired by the echolocation behavior of bats [98, 99]. The bats use a type of sonar, called, echolocation to build a precise image of their surroundings in order to detect prey and avoid obstacles [98, 99, 100]. These bats emit a very loud sound pulse and listen for the echo that bounces back from the surrounding objects. Each pulse only lasts a few thousandths of a second (about 8 to 10 ms), however, it has a constant frequency which is usually in the region of 25 kHz to 150 kHz. Where, each ultrasonic burst may last typically 5 to 20 ms, and bats emit approximately 10 to 20 of such sound bursts every second. The pulse emission rate increases depending on how close the bats are to the prey. When they fly near their prey, the rate of pulse emission can be sped up to about 200 pulses per second. These short sound bursts imply the fantastic ability of the signal processing power of bats.

The principle of the bats echolocation behavior is illustrates in figure 4.3, where the yellow pulses represent the sonar waves that are emitted by the bat and the red pulses indicate the reflected signal by the sounds bounce of objects and return as echoes from the prey or the obstacle, and this help the bats to determine the direction and distance of anything in their path.

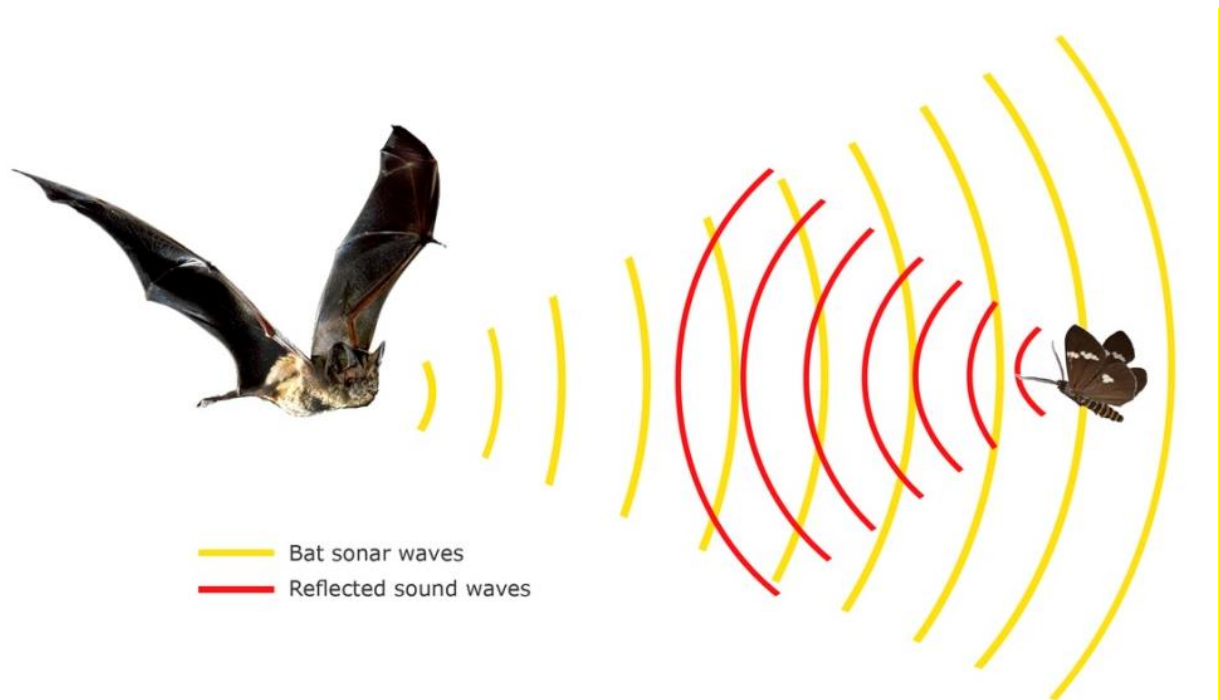


**Figure 4.3** Principle of the bats echolocation behavior

The three idealized rules used of developing the bat algorithm are [97]:

1. All bats use echolocation to sense distance, and they also ‘know’ the difference between food/prey and background barriers in some magical way.
2. Bats fly randomly with velocity  $v_i$  at position  $x_i$  with a fixed frequency  $f_{min}$ , varying wavelength  $\lambda_b$  and loudness  $A_0$  to search for prey. They can automatically adjust the wavelength (or frequency) of their emitted pulses and adjust the rate of pulse emission  $r \in [0; 1]$ , depending on the proximity of their target.
3. We assume that the loudness varies from a large positive value  $A_0$  to a minimum constant value  $A_{min}$ ; it can vary in many ways.

#### 4.5.1. Movement of Virtual Bats

Initializing the bat population is performed randomly in this Algorithm, with each bat ( $b_i$ ) is defined by its position ( $x_i$ ), velocity ( $v_i$ ), frequency ( $f_i$ ), loudness ( $A_i$ ) and the emission pulse rate ( $r_i$ ) in a  $d$ -dimensional search space. Let ( $N_p$ ) be number of bats in the echolocation, and ( $t$ ) is the number of iterations.

New solution generation or motion of virtual bats is performed by updating their frequency, velocity which is proportional to frequency and position according to the following equations [97, 98]:

$$f_i = f_{min} + (f_{max} - f_{min}) \cdot \beta \quad (4.1)$$

$$v_i^t = v_i^{t-1} + [v_i^{t-1} - x^{best}] \cdot f_i \quad (4.2)$$

$$x_i^t = x_i^{t-1} + v_i^t \quad (4.3)$$

Where  $\beta \in [0,1]$  indicates a random vector drawn from a uniform distribution,  $f_i$  is a frequency value corresponding to the  $i^{th}$  bat used for seeking its prey,  $f_{min}$  and  $f_{max}$  are minimum and maximum frequency values respectively, and  $v_i^t$  is the velocity of the  $i^{th}$  bat at  $t^{th}$  time step,  $x^{best}$  is the obtained best solution after comparing all solutions among the  $Np$  bat.

A solution is selected from the best current solutions and then for local search, we apply the random walk on bats with their pulse emission rates ( $r_i$ ) smaller than the random number in order to generate a new solution for each Bat as follows [97, 98]:

$$x_{new} = x_{old} + \varepsilon A^t \quad (4.4)$$

Where  $\varepsilon \in [-1; 1]$  is a random number and represents direction and intensity of random-walk and  $A^t$  is the average loudness of all the bats at time  $t$ .

#### 4.5.2. Loudness and pulse emission

Once the bat has found its prey, the loudness decreases while pulse emission rate gradually increases as shown in figure 4.4 and 4.5.

At each iteration of the algorithm, loudness  $A_i$  and pulse emission rate  $r_i$  are updated by the following equations:

$$A_i^t = \alpha A_i^{t-1} \quad (4.5)$$

$$r_i^t = r_i^0(1 - e^{\gamma t - 1}) \quad (4.6)$$

Where  $0 < \alpha < 1$  and  $\gamma > 0$  are constants [97, 101]. At the initialization step of the algorithm, each bat has a different random loudness  $A_i^0$  which is in  $[1; 2]$  and random pulse emission rates  $r_i^0$  which is in  $[0; 1]$ . It is worth noting that bat algorithm balance between global and local search by adjusting the loudness and pulse rate.

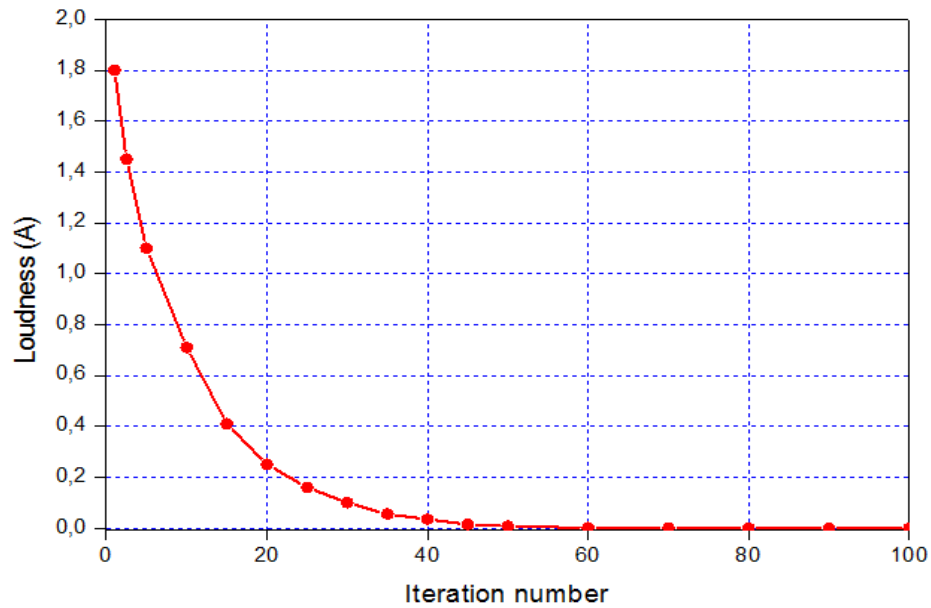


**Figure 4.4** Loudness A

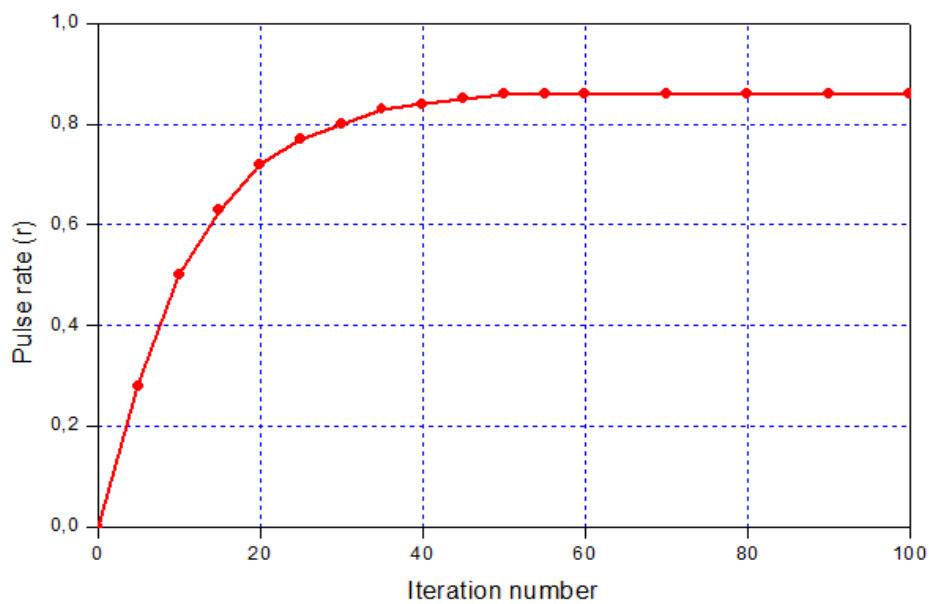


**Figure 4.5** Pulse emission rate r

Main steps of Bat algorithm can be summarized as the pseudo-code shown in figure 4.6.

**Bat Algorithm:**

**Input:** Bat population  $x_i = (x_{i1}, \dots, x_{id})^T$ , for  $i = 1, 2, \dots, Np$ , velocity ( $v_i$ ), frequency ( $f_i$ ), loudness ( $A_i$ ), pulse rate ( $r_i$ ) and the maximum number of iteration (Max\_It).

**Output:** The best solution  $x^{best}$  and its corresponding fitness value  $f(x^{best})$

- (1) Initialize the bat population  $x_i$  ( $i = 1, 2, \dots, Np$ )
- (2) Evaluate fitness for each bat  $f(x_i)$

**while** ( $t < Max\_It$ )

**for**  $i = 1$  **to**  $Np$  **do**

    Generate new solutions by adjusting frequency, and updating velocities and locations/ solutions [equations (4.1) to (4.3)]

**if** ( $rand < r_i$ )

      Select a solution among the best solutions

      Generate a local solution around the selected best solution

**end if**

    Generate a new solution by flying randomly

**if** ( $rand < A_i$  and  $f(x_i) < f(x^{best})$ )

      Accept the new solutions

      Increase  $r_i$  and reduce  $A_i$

**end if**

**end for**

  Rank the bats and find the current best  $x^{best}$

**end while**

Display results

**Figure 4.6** Pseudo -code of Bat algorithm

#### **4.6. Flowchart of the optimization process**

Project process for optimization of grading ring parameters is carried out as follows:

- 1- 3D model of studied metal oxide surge arrester was designed by the Computer Aided Design (AutoCAD) software package. After, this model was imported into COMSOL Multiphysics.
- 2- Three-dimensional finite element method was employed based on COMSOL MULTIPHYSICS software to calculate the electric field and voltage distribution depending on grading ring geometrical parameters.
- 3- Taguchi design was employed based on MINITAB software to find the objective function which consists of a mathematical relationship between the maximum E-field magnitudes and grading ring parameters.
- 4- Bat algorithm has been implemented using JAVA Script software to optimize the grading ring parameters. The objective function was introduced in the program of Bat.

The process flow for optimizing the grading ring parameters can be summarized by steps shown in figure 4.7. This figure shows all the optimization processes involved starting from the initial stage until the desired results of optimization are obtained.

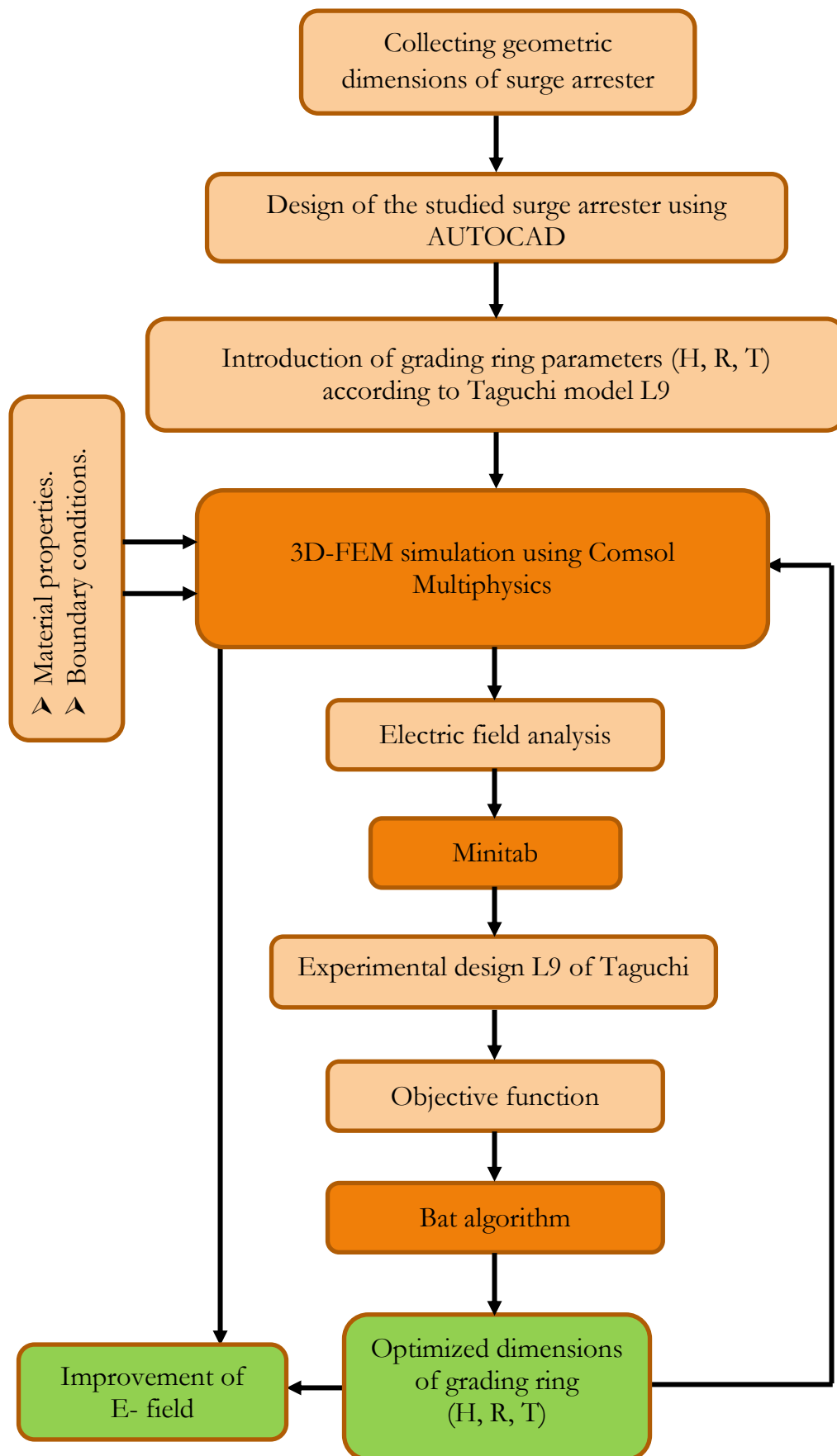


**Figure 4.7** Optimization process steps

## 4.7. Results and discussion

### 4.7.1. FEM Simulation without grading ring

Initially, the electric field and potential distribution are computed along the central axis of the metal oxide surge arrester without grading ring.

Figure 4.8 shows the E-field distribution, it is clearly indicated that the E-field at the HV electrode of the surge arrester reaches a maximum value located at the same triple point height and decreases rapidly then after. So the top discs near the HV electrode are more stressed [9, 13].

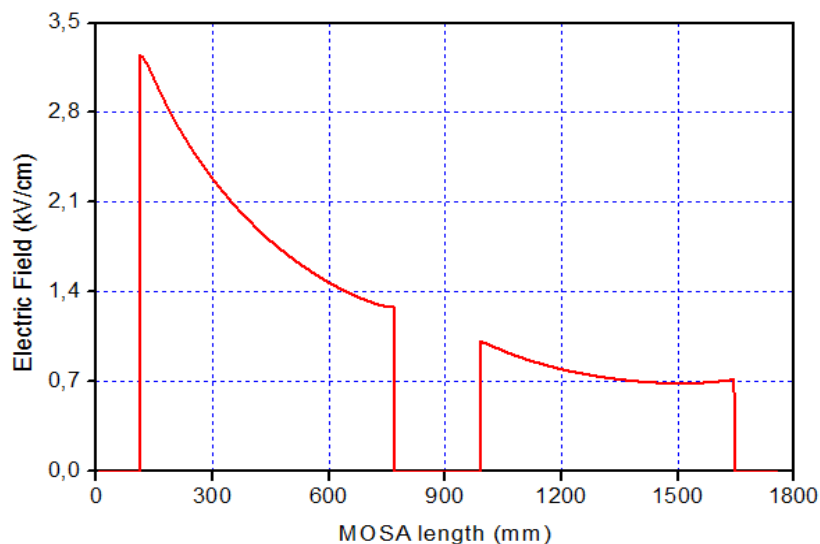


**Figure 4.8** E-field distribution along the central axis of the surge arrester without grading ring

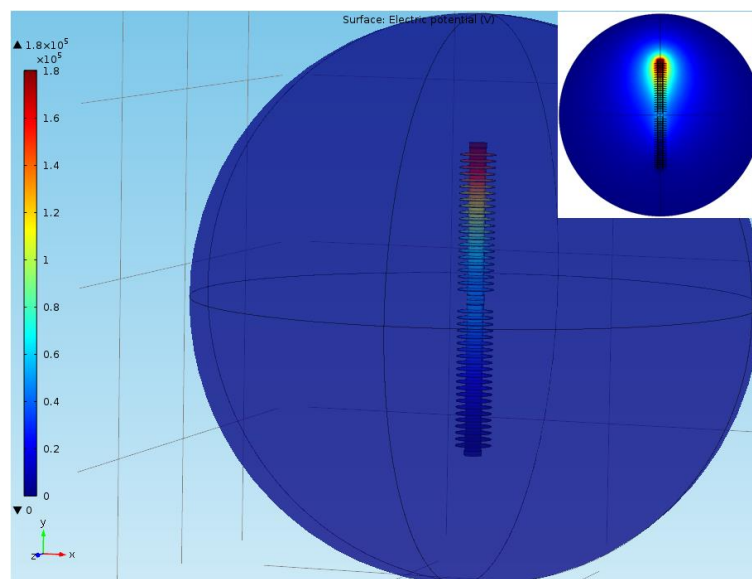


**Figure 4.9** Distribution of the electric potential for a surge arrester without grading ring

Figure 4.9 shows the distribution of the electric potential along the studied metal oxide surge arrester without grading ring. The high electric potential strength areas are concentrated on the top of arrester close to the energized end. It is shown that the potential distribution along the arrester is not uniform because of the effect of the stray capacitances to the earth and to the HV electrode [1].

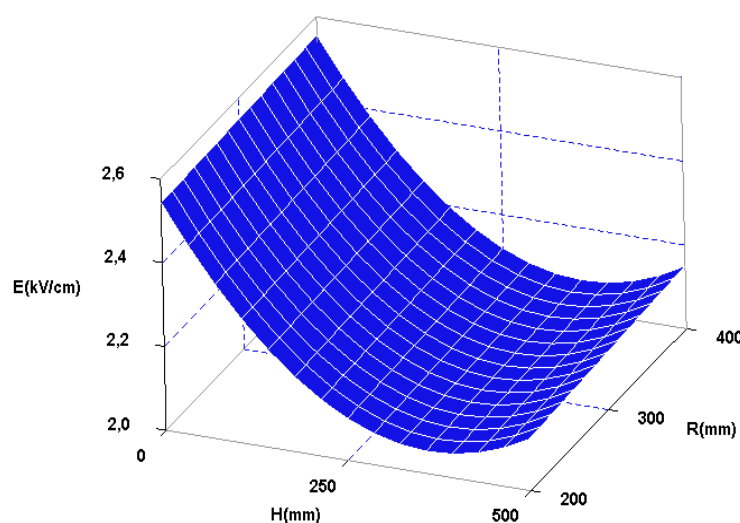
#### 4.7.2. FEM Simulation with Grading Ring

In order to examine the influence of ring parameters (H, R, T) on the axial distribution of the E-field, 3D-FEM simulation is carried out. The electric field variation is plotted as a function of two ring parameters, while the third parameter is kept at a fixed value.

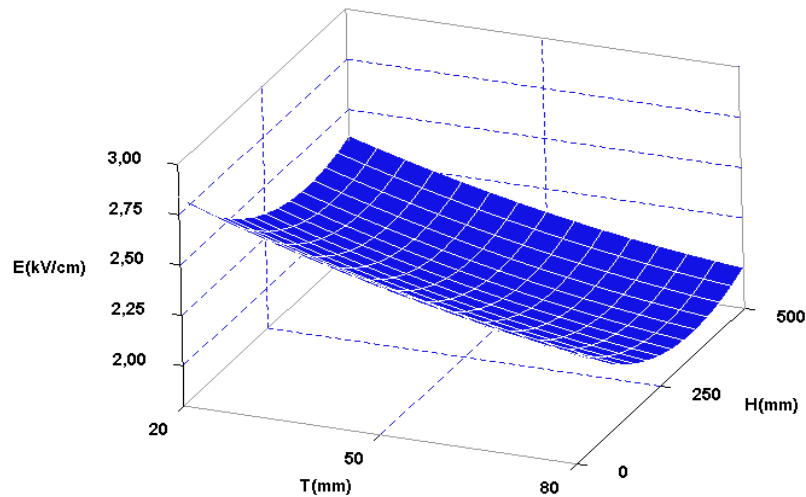
Figure 4.10 shows the maximum E-field in the top discs of arrester which located at the same triple point height for different H and R chosen previously while keeping ring tube thickness at  $T=50$  mm. It is noticed that increasing the ring position firstly decreases strongly the E-field to reach a minimum value before increasing again. On the other hand, increasing ring radius (R) increases the E-field.

Figure 4.11 shows the maximum E-field for different T and H with  $R=300$  mm. It can be seen that increasing the ring tube thickness has an effect of reducing the E-field.

Figure 4.12 shows the effect plots of ring radius and ring tube thickness on the E-field value. It can be seen that the minimum E-field is correspondent to ring radius value equal to 200 mm and to ring tube thickness value equal to 80 mm.



**Figure 4.10** Maxim E-field for different H&R with  $T=50$  mm



**Figure 4.11** Maximum E-field for different T&H with  $R=300$  mm

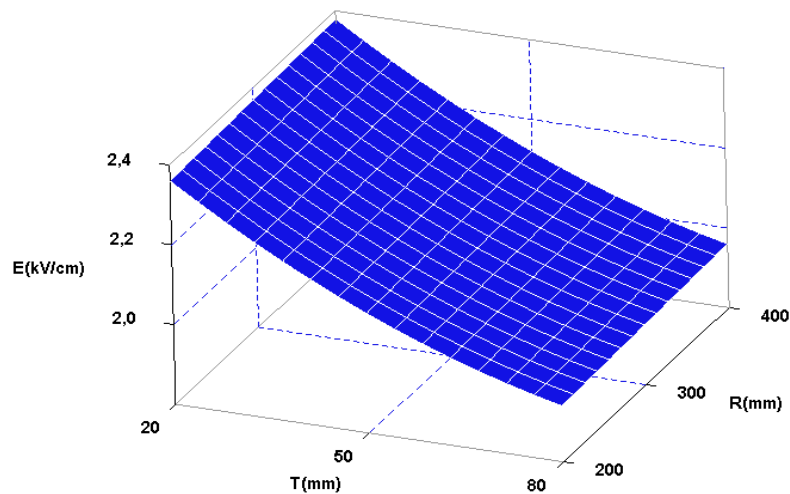


**Figure 4.12** Maximum E-field for different R&T with  $H=250$  mm

The increase of the ring radius has an increasing influence on the E-field. According to these obtained results, the optimum value of  $H$  that corresponds to a minimum value of the E-field varies in the interval [300-400] mm.

In addition, the electric field is reduced, if the ring is closer to shed, and if the ring tube thickness is at the chosen maximum value.

Therefore, grading ring parameters should be optimized to obtain better electric field distribution along the MOSA.

### 4.7.3. Optimization of the Grading Rings Parameters Based On BAT Algorithm

The main objective of the optimization of grading ring geometrical parameters is to reduce maximum E-Field along 220 kV MOSA and improve its distribution.

In our work, the optimization process is based on BAT algorithm. Indeed, the optimization problem can be formulated as follows:

$$f(x_1, x_2, x_3) = E(H, R, T) \quad (4.7)$$

Where  $x_1, x_2, x_3$  corresponds to H, R and T respectively,

E : E-field [kV/cm].

H : grading ring position from HV electrode [mm].

R: grading ring radius [mm].

T : the thickness of the grading ring tube [mm].

In order to obtain the objective function which can evaluate relationship between maximum electric field strength and grading ring structure parameters, a combined method based on 3D-FEM and Taguchi design is opted. Results of these experiments analyzed and fitted to a second-order polynomial using regression analysis as given by the following form [81, 96]:

$$Y = a_0 + \sum_{i=1}^3 a_i \cdot X_i + \sum_{i=1}^3 a_{ii} \cdot X_i^2 + \sum_{i<j}^3 a_{ij} \cdot X_i \cdot X_j \quad (4.8)$$

Where:

Y: represents the wanted response.

$a_0, a_i, a_{ii}$  and  $a_{ij}$  : are regression coefficients.

$X_i$ : Represents the input variables related to the considered parameters.

$X_i^2$ : Represents the square of the variables and  $X_i \cdot X_j$  represents the interaction between variables.

**Table 4.4** Numerically computed results for a single ring

H [mm]	R [mm]	T [mm]	E [kV/cm]
0	200	20	2.83
0	300	50	2.55
0	400	80	2.37
250	200	50	2.10
250	300	80	1.95
250	400	20	2.38
500	200	80	1.99
500	300	20	2.37
500	400	50	2.15

We keep the same variation ranges of studied parameters (H, R, T) of the table 4.2.

We adopted the experimental design L9 of Taguchi orthogonal array as shown in table 4.4. It's the most suitable orthogonal array for experimentation [94]. Numerically computed results obtained by 3D-FEM of table 4.4, relating to the studied configurations of grading ring parameters such as H, R, T and its corresponding maximum E-field are used to find the objective function.

The objective function consists of a mathematical relationship between the maximum E-field magnitudes and grading ring parameters and their interactions. For this reason, Statistical software MINITAB ®18 was employed. It can be presented according to the following equation:

$$E = 3.063 - \left( \begin{matrix} 2911.H - 67.R + 13440.T \\ - 4.H^2 - 56.T^2 - 4.H.T \end{matrix} \right) \cdot 10^{-6} \quad (4.9)$$

Where:

E : Electric field [kV/cm].

H : grading ring position from HV electrode [mm].

R : grading ring radius [mm].

T : the thickness of the grading ring tube [mm].

The optimal design is achieved by minimizing the objective function mentioned in (4.9). This objective function was inserted in the program of BAT algorithm in order to optimize grading ring parameters.

Note that the advantage of BAT algorithm is a very program, the Bat algorithm enables rapid convergence to an accurate solution. It is a simple and efficient algorithm.

The optimum value of the electric field is achieved (1.87 kV/cm) as shown in figure 4.13. From this figure, it can be seen that the objective function achieves its minimal value after a few numbers of iterations (5th iterations) and then any change can happen. The optimal value corresponds to the minimum value on the 100 iterations in figure 4.13.

The optimized dimensions of grading ring are: grading ring position  $H=310$  mm mm, radius of grading ring  $R=200$  mm, and grading ring tube thickness  $T=80$  mm.

In order to validate the powerful and the reliability of the used optimization method and to check accuracy of the obtained results, two different optimization algorithms, Particle Swarm Optimization (PSO) and Genetic Algorithm (GA) are utilized for comparison with a Bat algorithm. This comparison was made for the same studied MOSA, and the optimal design of grading ring is achieved by minimizing the same used objective function mentioned in (4.9) for the same number of iterations.

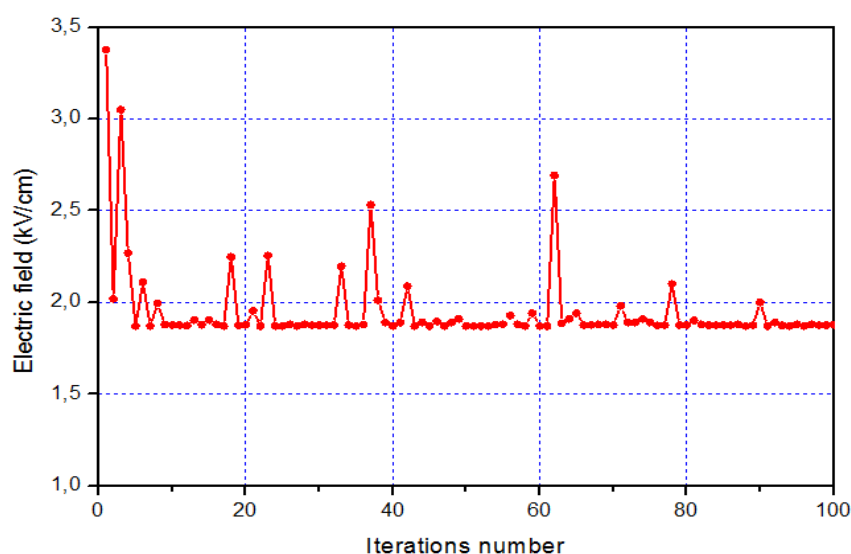


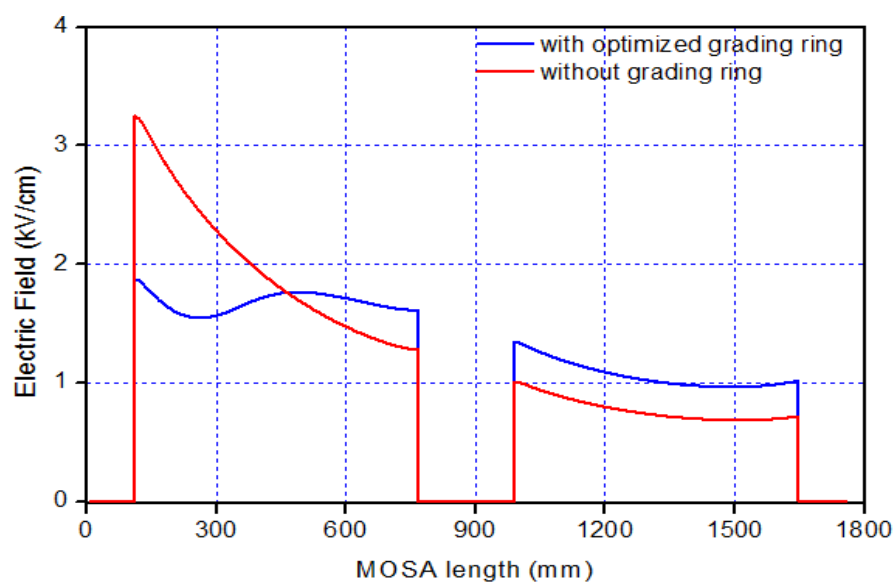
**Figure 4.13** Convergence process of the objective function for 100 iterations

**Table 4.5** Grading ring parameters optimization for different optimization algorithm

Parameters	H [mm]	R [mm]	T [mm]	E [kV/cm]	Computation time [s]
BAT	310	200	80	1.87	5
PSO	325	200	80	1.91	12
GA	341	203	80	1.96	45

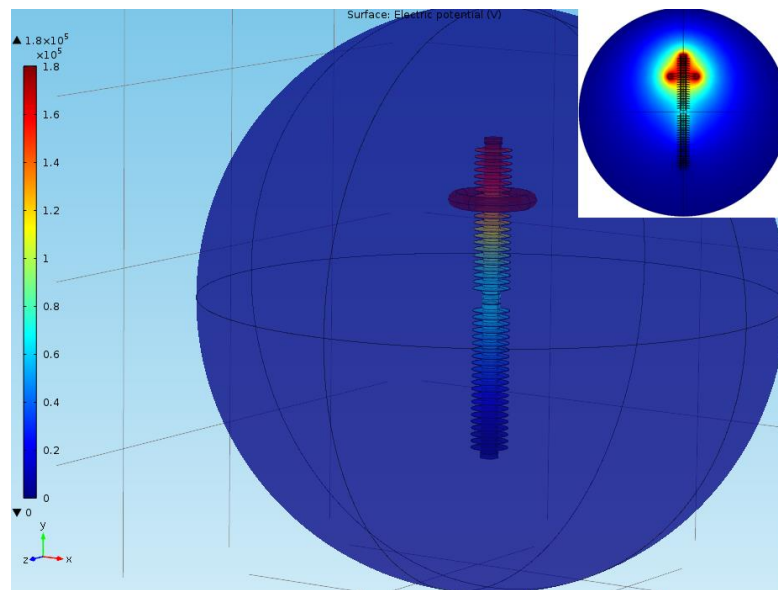
The obtained results are shown in table 4.5. From these results, we can notice that the BAT, PSO, and GA methods almost lead to the close results. The E-Field value optimized by Bat algorithm corresponds to the minimum value compared to the other methods, which means that the Bat algorithm produces more accuracy results. It's our goal to get the minimum value.

Furthermore, the BAT approach possesses less computation time than the other two algorithms as shown in table 4.5. We note that choice of the objective function based on the 3D-FEM and Taguchi design is minimized the computation time.

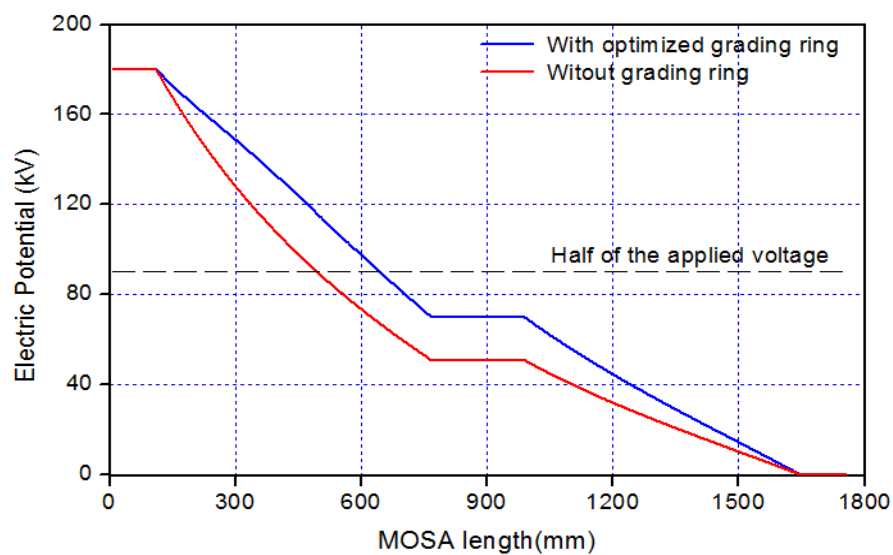
**Figure 4.14** E-field distribution along the central axis of the surge arrester

Then, these optimized parameters are verified by FEM. We insert these parameters into the 3D model of the surge arrester, in order to see the distribution of the electric field and the potential along the surge arrester.

Figure 4.14 shows the E-field distribution along the central axis of the 3D surge arrester with optimized grading ring; it is clearly observed that the E-field at the HV electrode of the surge arrester have been reduced by nearly 42%. The optimized grading ring installation improves the electric field distribution along the surge arrester.



**Figure 4.15** Distribution of the electric potential for a surge arrester with optimized grading ring



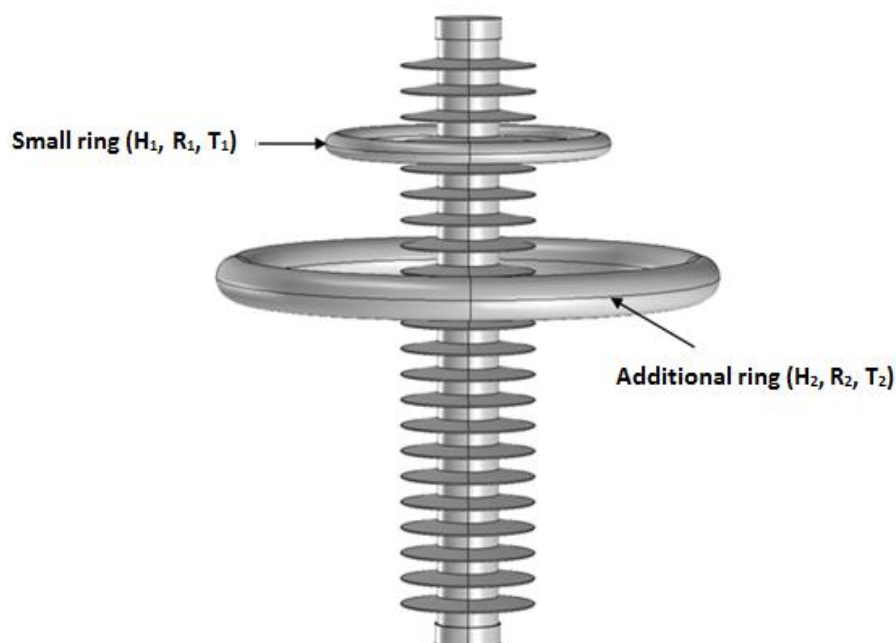
**Figure 4.16** Electric potential distribution along the central axis of the surge arrester

Figure 4.15 illustrates the distribution of the electric potential along the studied metal oxide surge arrester with optimized grading ring. It is shown that the potential distribution along the arrester is improved compared to the case without ring; this improvement is well clear up in figure 4.16. This figure shows that before the installation of grading ring, the half of the applied voltage (90 kV) is supported only by 500 mm of the surge arrester length. While by using the optimized grading ring, this distance is increased to reaches almost 700 mm of the surge arrester length and that means improving the potential distribution.

#### 4.7.4. Additional grading ring installation

From the results obtained in section 4.7.3, it was considered that this improvement is not sufficient. For this purpose, it has been proposed to install an additional ring in order to make the potential distribution as uniform as possible and to reduce the electric field value in the top of arrester. The proposed additional ring has a large geometric dimension compared to the first ring as shown in figure 4.17 [29, 87, 102].

According to some simulation tests, the dimensions of small ring have been fixed to new values different from the ring dimensions in the first case where there is only one ring, and the dimensions of the large ring were allowed to vary, three levels for each parameter are chosen as shown in Table 4.6.



**Figure 4.17** Studied metal oxide surge arrester with additional ring

**Table 4.6** Parameters of grading rings

Parameters	H [mm]	R [mm]	T [mm]
<b>Small ring</b>	150	175	30
	200	200	20
<b>Large ring</b>	350	300	50
	500	400	80

As already said, there are two rings used to improve the distribution of the potential and the electric field, a small ring and a large ring. The thickness of the small ring was set at 30 mm. The increase in the thickness beyond this value will increase the electric field to the metal flanges in the middle of the arrester and make its distribution no uniform.

**Table 4.7** Numerically computed results for two rings

H <sub>2</sub> [mm]	R <sub>2</sub> [mm]	T <sub>2</sub> [mm]	E [kV/cm]
200	200	20	2.18
200	300	50	1.93
200	400	80	1.78
350	200	50	1.77
350	300	80	1.64
350	400	20	1.85
500	200	80	1.81
500	300	20	1.78
500	400	50	1.63

The value of  $H_1$  is fixed at 150 mm. Also, we chose the same minimum distance between the shed and ring. Therefore, we chose the radius of the small ring at 175 mm. These chosen values always remain our own proposal.

Table 4.7 shows the nine studied configurations of grading rings and its corresponding highest E-field, distributed according to the model L9 of Taguchi orthogonal array.

The obtained objective function in this case is as follows:

$$E = 3.047 - (3833 \cdot H_2 - 89 \cdot R_2 + 15190 \cdot T_2 - 4 \cdot H_2^2 - R_2^2 - 44 \cdot T_2^2 + 3 \cdot H_2 \cdot R_2 + 19 \cdot H_2 \cdot T_2) \cdot 10^{-6} \quad (4.10)$$

Where:

$E$  : E-field [kV/cm].

$H_2$  : Large ring position from HV electrode [mm].

$R_2$  : Large ring radius [mm].

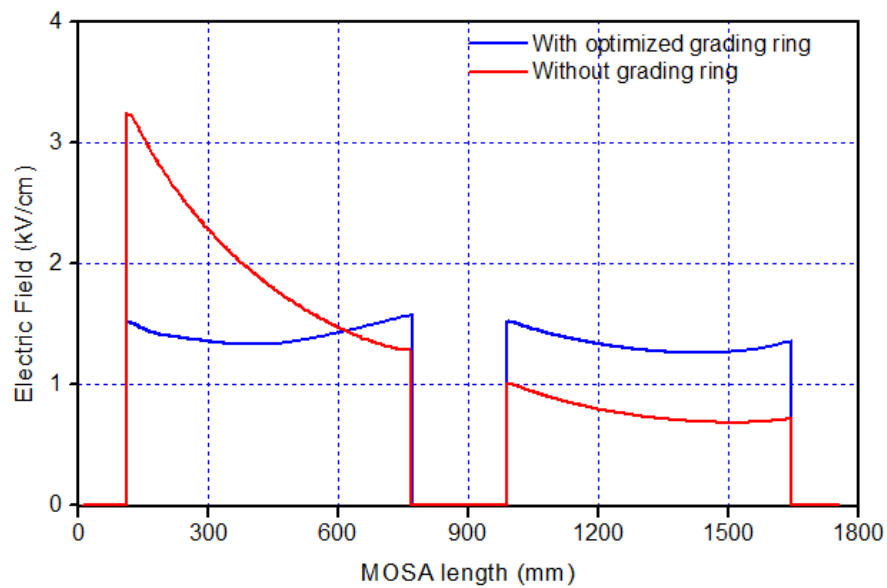
$T_2$  : Large ring tube thickness [mm].

Then, the geometrical parameters of the additional ring (large ring) have been optimized using bat algorithm in the same way for a single ring. These optimized parameters are: grading ring position  $H_2=457$  mm, radius of grading ring  $R_2=200$  mm, and grading ring tube thickness  $T_2=80$  mm. In this case, the optimum value of the electric field is 1.51 kV/cm. Furthermore, by using an optimal design of double rings, the E-field at the HV electrode was reduced by 53% and redistributed along the arrester as shown in figure 4.18.

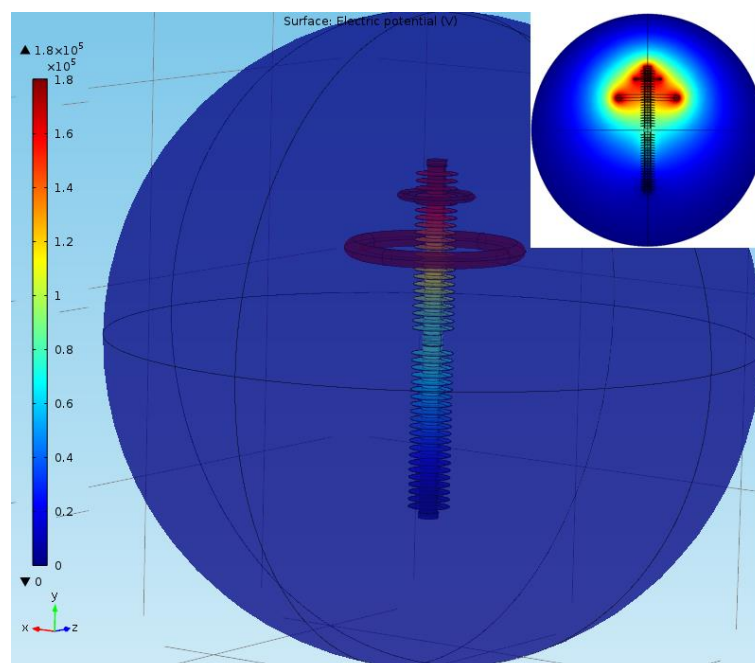
It is clearly observed that the optimized grading rings installation improves the electric field distribution along the metal oxide surge arrester.

Figure 4.19 shows the electric potential distribution along the studied metal oxide surge arrester with two optimized grading rings. It is shown that the potential distribution

along the arrester is uniform; this uniformity is well clear in figure 4.20, where it is shown that the applied voltage is almost equally distributed on both units of MOSA.



**Figure 4.18** E-field distribution along the central axis of the surge arrester



**Figure 4.19** Distribution of the electric potential for a surge arrester with optimized grading rings

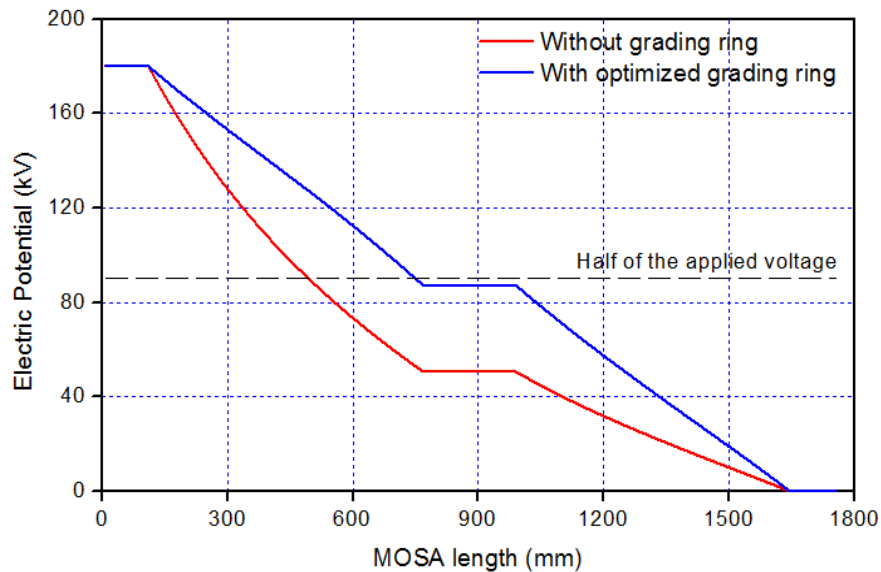


**Figure 4.20** Electric potential distribution along the central axis of the surge arrester

#### 4.8. Conclusion

The 3D finite element method was used to calculate the potential and electric field distributions of a 220 kV surge arrester. The effects of grading ring parameters are analyzed. A combined FEM and Bat algorithm was used to conduct the optimization process for grading ring parameters.

The optimal design of the grading ring is achieved by minimizing the electric field along the active column of varistors using a bat algorithm, and the objective function of this algorithm is based on Taguchi design which allows using response surfaces modeling (RSM).

Then the optimized parameters are verified by 3D-FEM. A good agreement has been reached between the results of this last and the Bat algorithm.

The obtained results shows that using of an optimal design of a single grading ring, the electric field is reduced by 42% in the top of the 220 kV MOSA and the electric potential distribution can be improved.

In order to obtain a better distribution of the potential and the electric field along the arrester, an additional ring has been proposed. This proposed additional ring has a large geometric dimension compared to the first ring. The dimensions of small ring have been

fixed, and the dimensions of the large ring were allowed to vary. Simulation results shows that using of an optimal design of double rings, the potential distribution can be made as uniform as possible and the electric field is reduced by 53% to avoid damage of varistors.

## **CHAPTER 5**

# **ELECTROTHERMAL MODELING OF METAL OXIDE SURGE ARRESTER**

---

---

## *Chapter 05*

---

# ELECTROTHERMAL MODELING OF METAL OXIDE SURGE ARRESTER

---

### **5.1. Introduction**

In this chapter; we will present the complete equivalent circuit developed for the simulation of the thermal behaviour of the polymer surge arrester, and the modeling details of the different parts of this circuit. Then, the equivalent circuit of the electrothermal model will be implemented in the ATP / EMTP simulation software. This model allows us to know the temperatures of the varistors and of the surge arrester housing.

Finally, we will present at the end of this chapter discussions of the obtained simulation results.

### **5.2. Electro-thermal model of metal oxide arrester**

The same polymeric surge arrester studied in the previous chapter is used here.

Surge arrester electro-thermal model composed of heat sources, thermal resistances and capacitances can be easily represented and simulated by means of ATP-EMTP program. The basic idea of analogue circuit is to describe a thermal problem by an electrical equivalent circuit and then solve the network equations. The approach is based on the similarity between the electrical and the thermal parameters [20, 68].

Thermal Network Method (TNM) utilizes the analogy between electric and thermal field problems as shown in table 5.1, where temperature and heat flow correspond to voltage and current respectively. This method considerably reduces the computation time, despite requiring the user to specify more geometric parameters than FEM models [20, 103].

**Table 5.1** Thermal–electrical analogies

	<b>Electrical parameters</b>	<b>Thermal parameters</b>
<b>Potential</b>	U [V]	T [°K]
<b>Current</b>	I [A]	Q [W]
<b>Resistance</b>	R [ $\Omega$ ]	R [°K/W]
<b>Capacitance</b>	C [F]	C [J/°K]
<b>Ohm's Law</b>	$I = U / R$	$Q = T/R$

### 5.3. Determination of thermal parameters

As discussed in chapter 3, there are three modes of heat transfer: conduction, convection and radiation, and they are determined by the structure and dimensions of the arrester.

In this study, the surge arrester can be represented by an axial cylinder [12]. It has been assumed that in the middle section of varistors column, the most heat transfer takes place radially and the axial heat flow is minimal [20, 103].

The arresters unit consists of metal oxide (ZnO) varistors encapsulated in a fiberglass reinforced plastic (FRP). The gap between the varistors column and the FRP cylinder is filled with silicone rubber. Everything is placed in silicone rubber housing.

The heat produced in the metal oxide varistors column is transferred to the outside by conduction directly to the thin silicon rubber layer, FRP cylinder, then to the housing. The outer surface of the arrester housing dissipates heat by radiation and free convection to the environment (surrounding air).

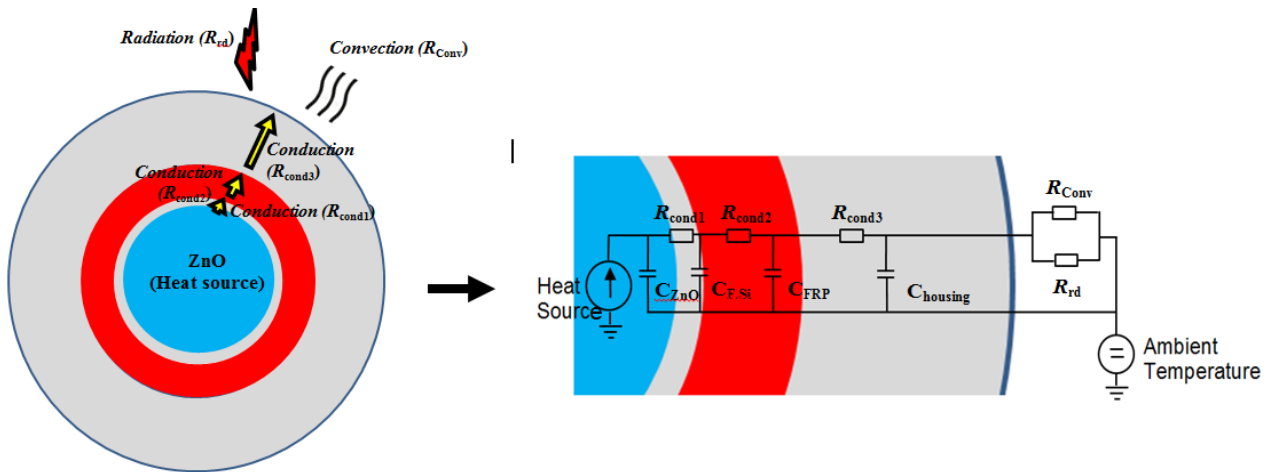


**Figure 5.1** Cross section and equivalent electro-thermal model of the surge arrester

The sample surge arrester assumed for the analyses and their cross-section are shown in figure 5.1.

### 5.3.1. Thermal resistances by conduction

Thermal resistances will be a function of the radial cross-section design and materials involved in the heat transfer path. Heat exchanges by conduction are governed by the Fourier equation(3.7).

In the case of coaxial cylinders, the calculation of the thermal resistance between two surfaces is given by the following expression [68, 72]:

$$R_{cd} = \frac{\ln\left(\frac{r_{out}}{r_{int}}\right)}{\lambda 2\pi L} \tag{5.1}$$

Where:

$\lambda$  : thermal conductivity [W/(m · °K)].

$L$  : is the height of the sample [m].

$r_{out}$  : is the outside diameter, and  $r_{int}$  is the inside diameter [m].

Table 5.2 summarizes the various thermal resistances by conduction of the surge arrester and their values.

**Table 5.2** Thermal resistances by conduction of metal oxide arrester components

	$D_{int}$ [mm]	$D_{out}$ [mm]	$\lambda$ [W/(m · °K)]	$R_{cd}$ [W/°K]
<b>filled silicone rubber insulation material</b>	71	73	0.22	0.0118
<b>fiberglass reinforced plastic (FRP)</b>	73	86	1.85	$83 \cdot 10^{-4}$
<b>Silicone rubber housing</b>	86	148	0.22	0.231

### 5.3.2. Thermal resistances by radiation

Heat transfer by means of radiation is the transfer of energy due to electromagnetic waves, and this does not require any medium for propagation. In the case of two coaxial cylinders, heat exchanges by radiation between two surfaces are generally defined by [68, 72]:

$$R_{rd} = \frac{T_2 - T_1}{\varepsilon \sigma S_p (T_2^4 - T_1^4)} \quad (5.2)$$

Where:

$\varepsilon$  : is emissivity between the side surface and the environment ( $0 \leq \varepsilon \leq 1$ );

$S_p$  : is the effective emitting area [ $m^2$ ];

$\sigma$ : Stefane Boltzmann's constant ( $5.67 \cdot 10^{-8}$  [W/ $m^2 \cdot ^\circ K^4$ ]);

$T_1$  : is the absolute temperature of emitting body [ $^\circ K$ ];

$T_2$  : is the absolute temperature of absorbing body [ $^\circ K$ ].

$$\varepsilon = \frac{1}{\frac{1}{\varepsilon_1} + \frac{S_{p1}}{S_{p2}} \left( \frac{1}{\varepsilon_2} - 1 \right)} \quad (5.3)$$

$\varepsilon_1$ : is the emissivity coefficient of body 1, and  $\varepsilon_2$  is the emissivity coefficient of body 1;

$S_{p1}$  : is the effective emitting/absorbing area internal [ $m^2$ ];

$S_{p2}$  : is the effective emitting/absorbing area external [m<sup>2</sup>];

### 5.3.3. Thermal resistances by convection

The heat flux exchanged by convection is given by [72]:

$$P_{cv} = \alpha \cdot S_p \cdot (T_2 - T_1) \quad (5.4)$$

So the thermal resistance is described as follows [72, 103]:

$$R_{cv} = \frac{1}{\alpha S_p} \quad (5.5)$$

Where:

$S_p$  : Area of convective surface [m<sup>2</sup>],

$\alpha$  : Heat transfer Coefficient [W/(m<sup>2</sup> · °K)].

In our case, heat transfer by convection occurs only between the surge arrester housing and the surrounding air, where the housing surface of which is exposed to a flowing fluid which is air.

The heat transfer coefficient  $\alpha$  depending not only on temperature but also on many other physical factors, like density, viscosity, pressure and so on. It is a complex phenomenon.

Following the long list of experimental observations, a way to get around this difficulty has been developed. It refers to what is called a group of dimensionless numbers, where the Nusselt, Grashof, Prandtl and Reynold numbers play an important role for determining the heat convection coefficient.

There are two types of thermal convection:

- Heat Transfer by natural convection
- Heat Transfer by forced convection

#### A. Natural convection

In natural convection, the fluid motion is caused by density differences in the fluid due to temperature differences.

The Nusselt number in this case is expressed as follows [72, 73]:

$$Nu = f(Gr \cdot Pr) = C \cdot (Gr \cdot Pr)^n \quad (5.6)$$

Where:

$Nu$  : Nusselt number;

$Gr$  : Grashof number;

$Pr$  : Prandtl number;

$C, n$  : are empirical constants.

Product  $Gr \cdot Pr$  is determined by [20, 72]:

$$Gr \cdot Pr = k_s \cdot L^3 \cdot \Delta T \quad (5.7)$$

$k_s$  : material parameter depends on sort of gas, its pressure and temperature;

$L$  : characteristic length;

$\Delta T$  : Temperature difference.

The heat transfer coefficient is based on definition of Nusselt number as follows [72]:

$$\alpha = \frac{Nu \cdot \lambda_{air}}{L} \quad (5.8)$$

$\lambda_{air}$ : Thermal conductivity of air;

## **B. Forced convection**

In forced convection, the fluid motion is caused by outer forces, for example by the pressure increase in a pump, a wind, a fan or some similar devices. For the surge arrester surface, the wind is the only cause of forced convection.

The Nusselt number in this case is expressed as follows [72, 73]:

$$Nu = f(Re \cdot Pr) = C \cdot (Re \cdot Pr)^n \quad (5.9)$$

$Re$  : Reynold number.

In our study, forced convection is neglected.

### 5.3.4. Thermal capacities of metal oxide surge arrester Components

The thermal capacity represents the quantity of energy that can be stored in a particular component of the surge arrester. The heat capacity is calculated based on the following formula [77]:

$$C_{th} = C_s \cdot V \quad (5.10)$$

Where:

$C_s$  : is the specific heat capacity [ $J/(m^3 \cdot ^\circ K)$ ];

$V$  : is the volume of the component [ $m^3$ ];

Or can be expressed as follows [103]:

$$C_{th} = C_s \cdot M \quad (5.11)$$

$M$  : is the mass of component [Kg];

$C_s$  : in this case is expressed by [ $J/(kg \cdot ^\circ K)$ ];

The thermal capacity of any particular component of surge arrester considered in this study was determined as shown in Table 5.3.

**Table 5.3** Thermal capacity of metal oxide arrester components

	$D_{int}$ [mm]	$D_{out}$ [mm]	Density [ $kg \cdot m^{-3}$ ]	Specific heat capacity $C_s$ [ $J/(kg \cdot ^\circ K)$ ]	Thermal capacity $C_{th}$ [ $J/^\circ K$ ]
<b>Varistor (<math>C_{ZnO}</math>)</b>	71	/	5500	430	12278
<b>filled silicone rubber insulation material (<math>C_{Filled\ silicone}</math>)</b>	71	73	1145	1506	546
<b>fiberglass reinforced plastic (FRP) (<math>C_{FRP}</math>)</b>	73	86	2000	535	2431
<b>Silicone rubber housing (<math>C_{housing}</math>)</b>	86	148	1145	1506	16740

### 5.3.5. Heat loss from varistors elements

The quantity of electrical power losses is related to the magnitude of the current, which flows through the surge arrester, the applied voltage, as well as geometrical dimensions and properties of surge arrester material.

It can be represented by an alternating voltage source applied to the surge arrester. The whole linked to power losses in the material (heat source). For this purpose, we need to the current which crosses the arrester, and the voltage applied to its terminals.

The electrical power loss by the Joule effect in the column of ZnO varistors can be described as follows [103]:

$$P = I^2 \cdot R_{20} \cdot (1 + \alpha_{20}(T - 20)) \quad (5.12)$$

Where:

$P$  : electrical power loss [W];

$I$  : current flowing through varistors [A];

$R_{20}$  : is the resistance of the MOSA at 20 °C [ $\Omega$ ];

$\alpha_{20}$  : is the temperature coefficient [ $^{\circ}\text{K}^{-1}$ ];

$T$  : is the ambient temperature.

The electrical behavior of the surge arrester, namely its current-voltage characteristic (V-I) shown in figure 5.2, is taken into account to modeled the studied surge arrester. For this purpose, the NLRES92 model was taken from the EMTP /ATP software.

According to cross section of the surge arrester shown in figure 5.1, an appropriate electro-thermal circuit has been built by means of ATP Draw tools as illustrated in figure 5.3.

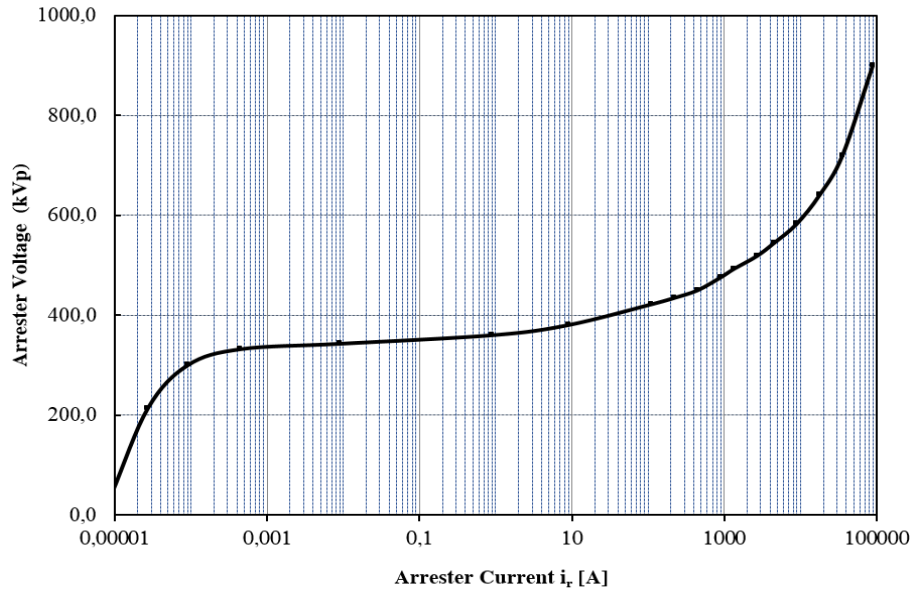


**Figure 5.2** V-I Characteristic curve for a 220 kV metal oxide surge arrester

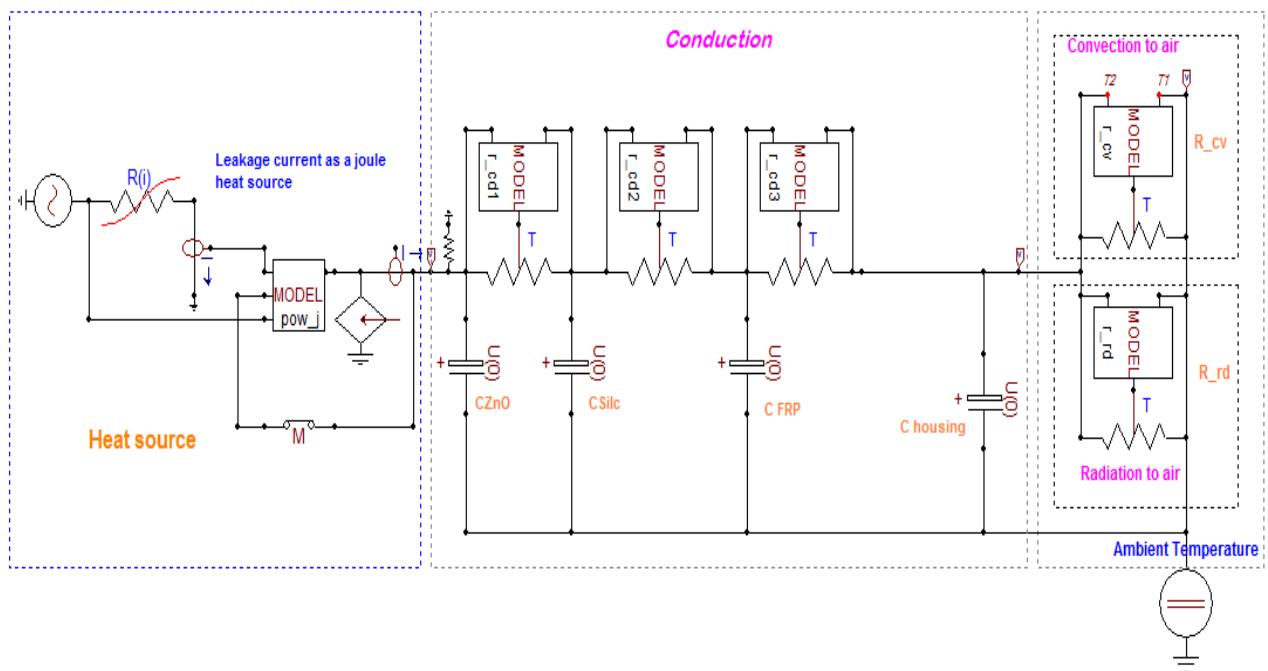


**Figure 5.3** Electro-thermal model of surge arrester

**5.4. Simulation results**

The purpose of this analysis was to estimate the temperature rise of surge arrester for different applied voltage. The proper evaluation of temperature rise would allow us to avoid the heating of the varistors and the total failure of the surge arrester.

**Table 5.4** Temperature of the studied 220 kV polymeric metal oxide surge arrester at environmental temperature of 20 °C.

Applied voltage		$0.7 \cdot U_{1mA}$	$0.8 \cdot U_{1mA}$	$0.9 \cdot U_{1mA}$
Temperature [°C]	Experimental results [21]	26.5	28.1	36.3
	Simulation results	25.1	27.75	36.4

In our electro-thermal study of surge arresters, we are confronted with two different time constants: the thermal time constant is per hours, while the time constant of electrical phenomena is only a few milliseconds. For the calculation of the thermal phenomena the step of time retained was of some tens of seconds.

#### 5.4.1. Validation of the electro-thermal model

The maximum temperature at thermal stable state under different applied voltages ratios are calculated and compared with the experimental results in Table 5.4. The surge arrester temperatures obtained by simulation are in good agreement with the experimental results.

#### 5.4.2. Study of the temperature variation of the surge arrester

The temperature of the surge arrester in steady state regime was determined for an applied voltage greater than its operating voltage, in order to better appreciate its thermal behavior. The voltage value ( $U_{1mA}$ ) when the direct current is 1 mA, is generally the important electrical parameter characterizing ZnO varistors in engineering [21, 42, 70]. For this purpose,  $U_{1mA}$  is adopted as the reference voltage.

Figure 5.4 shows the temperature variation of the MOSA during heating and cooling simulation under  $0.9 \cdot U_{1mA}$  applied voltage.

In the first phase, the surge arrester was energized by a voltage equal to  $0.9 \cdot U_{1mA}$  at an ambient temperature 20°C. The temperature of the column of varistors elements begins

to increase gradually (heating phase). The surge arrester absorbs energy which causes an increase in temperature of the ZnO elements. The leakage current flowing through the active column of the varistors generates a certain quantity of heat, and subsequently raises its temperature.

After a few minutes, the temperature of the varistors reach its steady-state phase, and which becomes finally equal to  $T = 36.4\text{ }^{\circ}\text{C}$  as shown in figure 5.4. A heat produced in ZnO varistors column is transferred directly to the environment by conduction across the thin silicon rubber layer, FRP cylinder, then to the housing. As well, the outer surface of the arrester housing dissipates heat by radiation and free convection to the environment.

In this case, the electrical power loss and the heat dissipation of the surge arrester are equilibrated.

At the same time, the heat dissipated by the varistors will heat the surge arrester housing (the heating phase) and the temperature of the silicone housing increases to  $25\text{ }^{\circ}\text{C}$ .

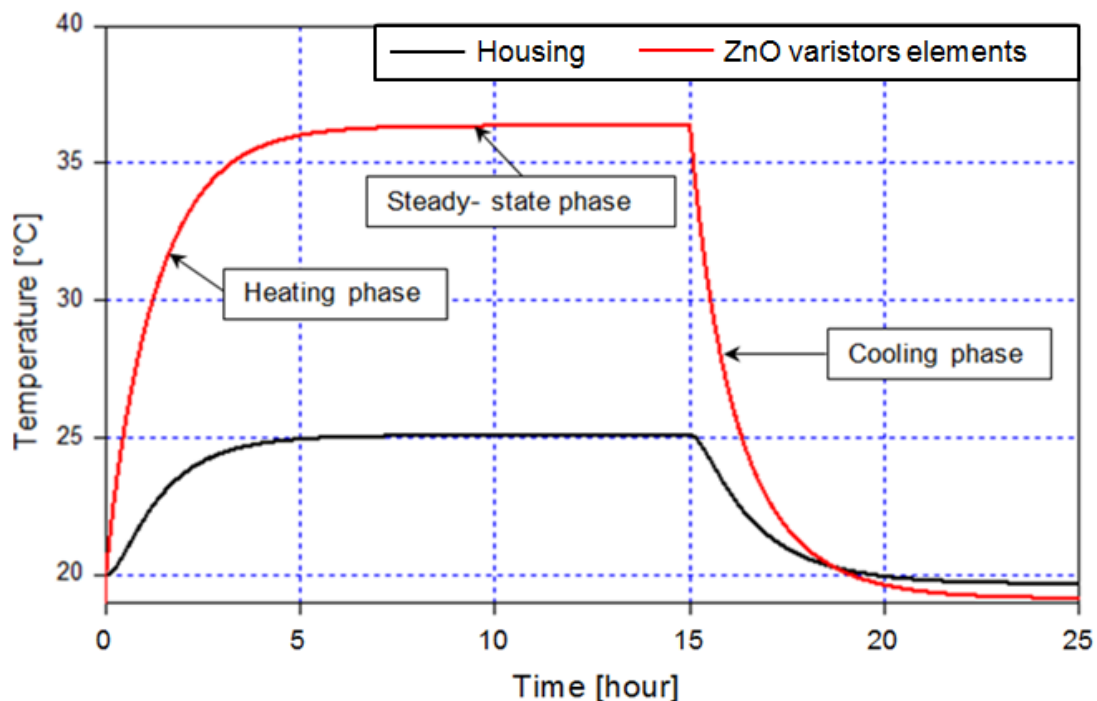


**Figure 5.4** Temperature variation of the MOSA during heating and cooling simulation under  $0.9 \cdot U_{1mA}$  applied voltage

The difference between the temperature of varistors and the environmental temperature is small (11.3 °C).

In the case of cooling phase where the applied voltage has been interrupted, the surge arrester begins to cool slowly until to ambient temperature 20°C (Cooling phase).

During the heating phase, the surge arrester presents a low thermal resistance, and reaches its stable value in steady-state phase. The thermal resistances ensures good cooling of the varistors elements by means of conduction in the arrester, convection ( $R_{cv}$ ) and radiation ( $R_{rd}$ ) to the environment as shown in figure 5.5.

In the cooling phase, the thermal resistance returns to increase when the temperature of surge arrester decreases. Therefore, the insufficient heat dissipation can cause the higher varistors temperature [25].

#### 5.4.2.1. Cooling under voltage

The cooling of the surge arrester without voltage has been studied as the first scenario. Then, we will study its cooling under voltage.

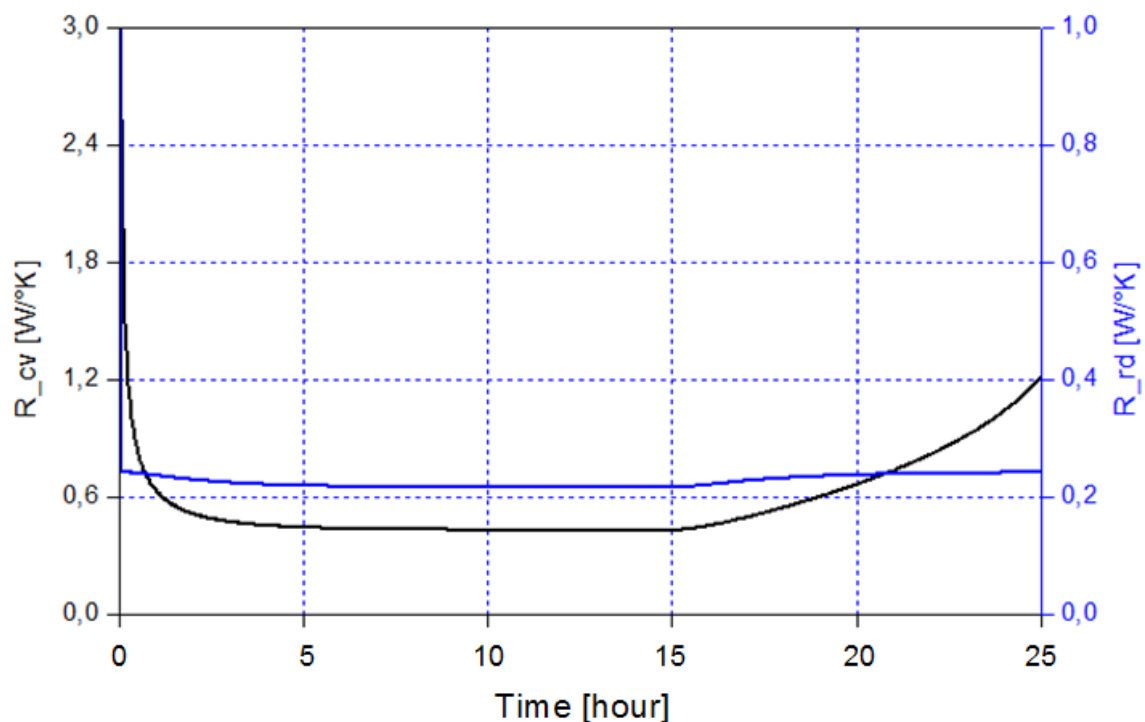


**Figure 5.5** Thermal resistances variation during simulation process.

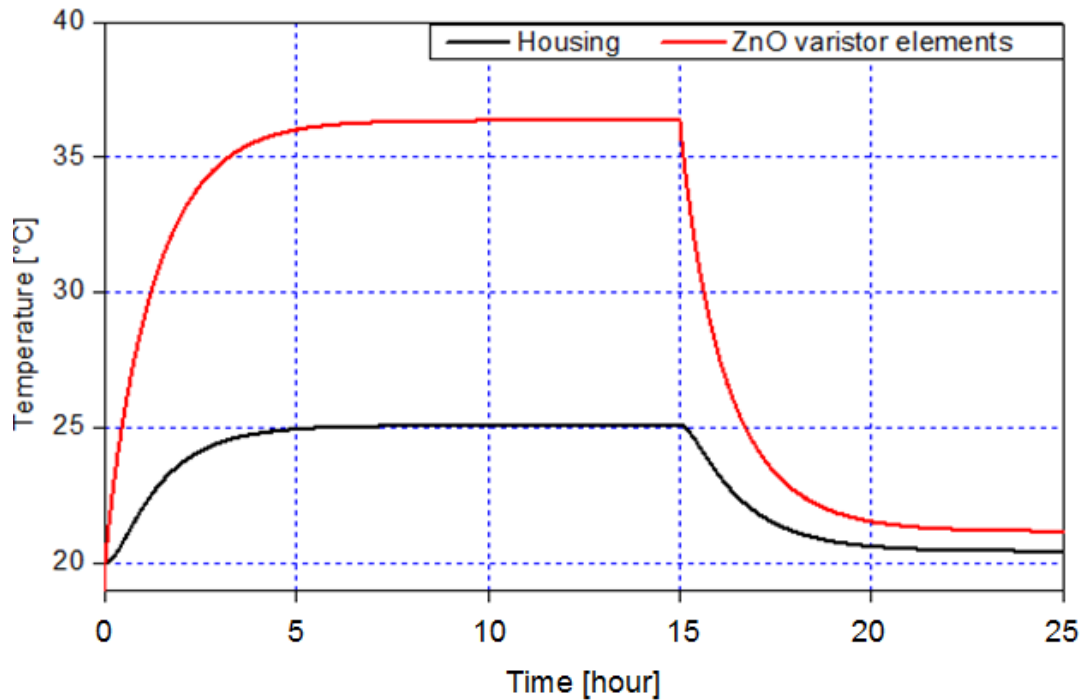


**Figure 5.6** Temperature variation of the MOSA during heating simulation under  $0.9 \cdot U_{1mA}$  applied voltage, and cooling under operating voltage

In the first time, the surge arrester was energized by a  $0.9 \cdot U_{1mA}$  voltage. After the arrester temperature reaches its stable state, we allow the surge arrester cool under maximum operating voltage (MCOV). Simulation results are shown in figure 5.6.

In this case, the temperature distribution obtained is very similar to that of free cooling (Fig. 5.4). The application of the permanent operating voltage causes a slight heating of the surge arrester.

Consequently, the heat dissipation throughout the surge arrester is realized as indicated for natural cooling. This is due to the greater amount of heat dissipated by thermal conductance.

### 5.4.3. Effect of applied voltage on temperature

The applied voltage ratio is altered from 0.7 to 0.99 in order to better assess its effect on temperature variation. The variation of the temperature of the varistors elements with the applied voltage is plotted in figure 5.7.

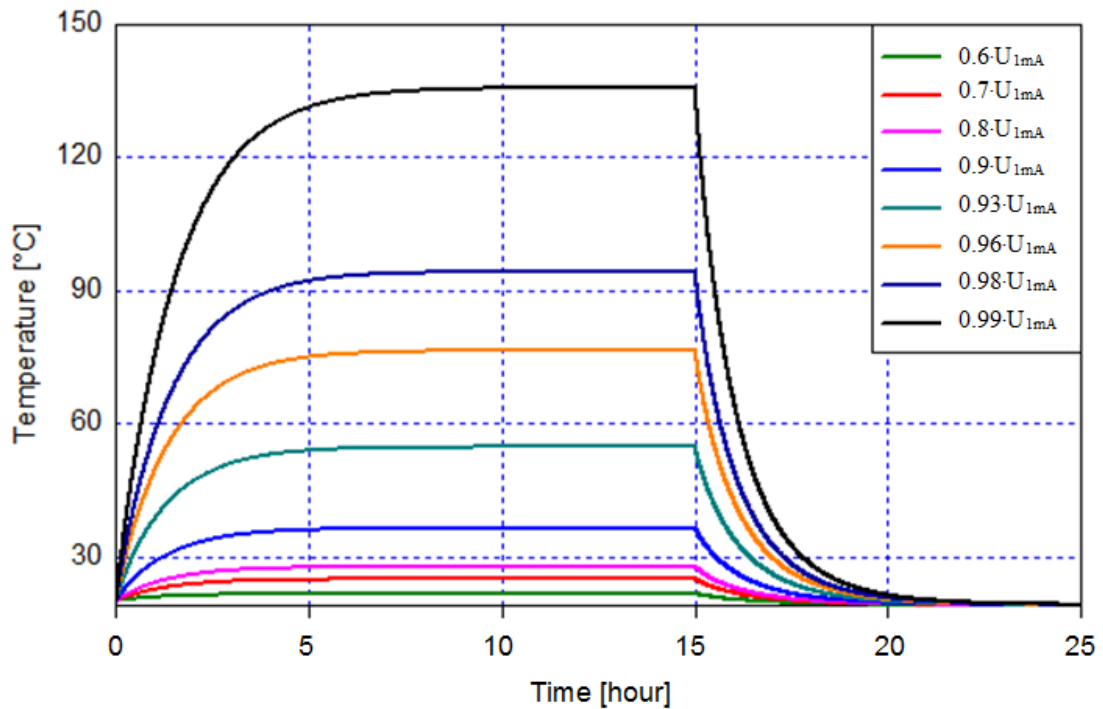


**Figure 5.7** Temperature variation of the varistors elements simulation under different applied voltage

From this figure, it can be seen that the temperature of the varistors increases as the applied voltage increases. The increase in the applied voltage causes the increase in the leakage current crossing the active column of the varistors and subsequently it's heating.

We can also notice that the temperature variation with the voltage becomes significant as one approaches the applied threshold voltage ( $0.9 \cdot U_{1mA}$ ). Indeed, the passage of the voltage of 0.9 to 0.93 (up to  $0.99 \cdot U_{1mA}$ ) results in a greater increase of temperature than the passage from 0.8 to 0.9.

#### 5.4.4. Effect of applied voltage on power loss

Figure 5.8 illustrates the power loss variation of the varistors elements as a function of voltage applied ratio. As see in this figure, the power losses increase slowly with the applied voltage ratio when is less than 0.85. But when the applied voltage ratio is greater than 0.9, the power losses increase quickly, and the values of power losses were large too.

The applied voltage ratio to the surge arrester would not be permitted to exceed  $0.9 \cdot U_{1mA}$  when it operating in power system [21], and this to prevent the overheating of the surge arrester and subsequently its total failure.

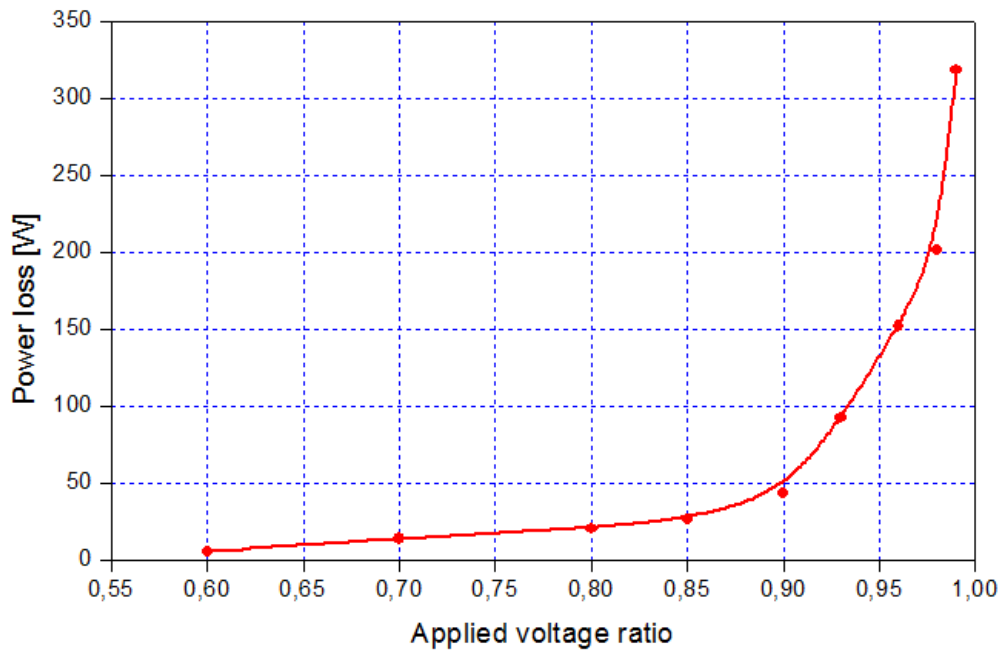


**Figure 5.8** Power loss variation as a function of applied voltage ratio at 20 °C

The power balance, lost by the Joule effect and thermally evacuated determines the upper and lower limit temperatures and the limit voltage. Exceeding the limit voltage causing thermal runaway.

#### 5.4.5. Effect of ambient temperature on the varistors temperature variation

The temperature of the varistors in permanent regime was determined for an applied voltage equal to  $0.9 \cdot U$  at different ambient temperatures.

Figure 5.9 shows the varistors temperature variation at different ambient temperatures ( $T_a$ ). The ambient temperature is chosen according to the permissible values by the manufacturer [21]. From this figure, it can be seen that the temperature of the environment directly influences the heating of the varistors. As the ambient temperature increases, the temperature of the varistors also increases, and this can lead to the failure of the surge arrester.

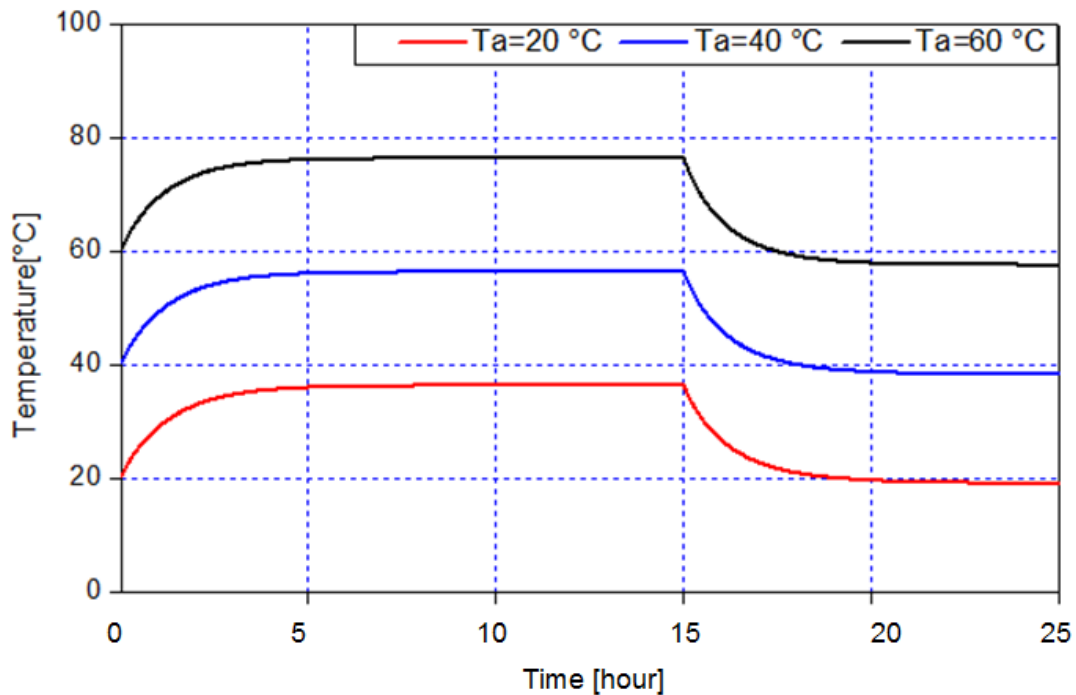


**Figure 5.9** Varistors temperature at different ambient temperatures

## 5.5. Conclusion

An electro-thermal model based on thermal network method (TNM) has been adopted in this chapter. The approach is based on the similarity between the electrical and thermal parameters. Power loss as a heat source has been estimated and applied to electro-thermal model of MOSA. Then, the equivalent circuit which composed of heat source, thermal resistances and capacitances, has been implemented in the ATP / EMTP simulation software. The behavior of the surge arresters in a permanent regime was solved by simulation, using a model which takes into consideration all the characteristics of the materials used and their dimensions, as well as thermal phenomena (conduction, convection, and radiation). The knowledge of the temperature evolution according to the incremented voltage, allows us to avoid the successive heating of the surge arrester and its failure by thermal runaway. Therefore, the specified temperature limits cannot be exceeded.

# **CHAPTER 6**

## **GENERAL CONCLUSIONS**

---

---

# Chapter 06

---

## GENERAL CONCLUSIONS

---

### 6.1 .Conclusions

This work aims to study and analyze the failure of metal oxide surge arresters. The study of the behavior of metal oxide surge arresters in steady state requires, an evaluation of the electric field constraints in the column of varistors, and on the other hand, to identify the temperature of arresters because it affects the varistors and therefore its failure. The high electric stress near the high voltage (HV) electrode in the upper part of the metal oxide surge arrester causing ageing and degradation of the varistors subjected to this constraint, and subsequently cause its total failure.

The first part of this thesis is aimed to improve the distribution of the potential and the electric field along a 220 kV polymeric surge arrester by optimizing the design of the grading ring. 3D finite element method was used to calculate the potential distribution and electric field distribution of the 220 kV surge arrester. Hence, a 220 kV metal oxide surge arrester has been successfully modeled by using Comsol Multiphysics software. The effects of grading ring parameters were analyzed. The optimal design of the grading ring such as positions of grading ring from HV electrode (H), grading ring radius (R) and grading ring tube thickness (T) was achieved by minimizing the electric field along the active column of varistors using 3D-FEM combined with the experimental design methodology of Taguchi and the BAT algorithm.

We used an experimental design methodology based on model L9 of Taguchi. Taguchi design was employed based on MINITAB software to find the objective function. Bat algorithm has been implemented using JAVA Script software to optimize the grading ring parameters.

The obtained results show that using of an optimal design of a single grading ring, the electric field distribution along the studied surge arrester has been improved. Then the optimized parameters were verified by 3D-FEM. A good agreement has been reached between the results of this last and the Bat algorithm.

In this work, the installation of an additional grading ring was proposed. For this purpose, an optimal design of double ring has been realized. The obtained simulation results in this case showed that the potential distribution was improved and made as uniform as possible, and the electric field was reduced by 53% to avoid damaging the varistors.

Metal oxide surge arresters are subjected to continuous operating voltage and transient voltages. The leakage current increases as the temperature of the arrester block increases. Therefore, the surge arrester condition can be evaluated by knowing the surge arrester temperature. Aspects related to thermal phenomena of metal oxide surge arrester are becoming very important due to the fact that they guarantee the correct operation of arrester.

In the second part of this work, the problem was solved by developing an equivalent electric model of thermal phenomena, which takes into account all the non-linearities including those due to convection and radiation.

This step allowed us to develop an equivalent electro-thermal model for the surge arrester made up of heat sources, thermal resistances and capacitances, whose parameters were identified, and then implemented in the ATP / EMTP software. A thermal model has been developed for modeling of arresters under various conditions of applied voltage, heating or cooling. The advantage of this model is that it saves a lot of time compared to the finite element method (FEM).

It is evident from various simulations of this last part of the work that, the specified temperature limits cannot be exceeded. Knowing the temperature of the varistors is an important factor when monitoring the condition of the surge arrester. Thus, the thermal behavior of MOSA is a very important factor in order to predict the reliability and performance of the installed surge arrester in its working environment.

## 6.2. Recommendations

As a perspective of this present work, we propose:

- To make certain the validity of the proposed approach to improve grading ring parameters, it is desired, as a future work, to introduce the experimental verification which is very important in this kind of research work.
- Study of the thermal behavior of surge arresters taking into account the degradation and aging of varistors.
- Optimization of the metal spacers dimensions and location which play an important role when cooling the surge arrester.

## References

- [1] A. Haddad and D. Warne, *Advances in High Voltage Engineering: IET Power and Energy Series 40*. London, United Kingdom: The Institution of Engineering and Technology, 2007.
- [2] M. ADJABI, “Analyse des parafoudres à Oxyde de Zinc dans les réseaux électriques à haute tension,” PHD thesis, University of BADJI MOKHTAR -ANNABA-, 2007.
- [3] N. Alti, “Contribution à l’étude de performances électriques des parafoudres synthétiques sous tension alternative,” Memory of magister, University of Ferhat Abbas SETIF-1-, 2012.
- [4] S. A. Halim, “Design and Evaluation of Metal Oxide Surge Arrester Parameters for Lightning Overvoltages Faculty of Engineering,” MALAYA KUALA LUMPUR, 2016.
- [5] G. R. S. Lira, E. G. Costa, and C. W. D. Almeida, “Self-organizing maps applied to monitoring and diagnosis of ZnO surge arresters,” in *2010 IEEE/PES Transmission and Distribution Conference and Exposition: Latin America, T and D-LA 2010*, 2011, pp. 659–664, doi: 10.1109/TDC-LA.2010.5762952.
- [6] M. N. Velani and S. C. Vora, “Stability predictions of zinc oxide surge arrester by employing finite element solutions,” in *Proceedings of 2019 International Conference on High Voltage Engineering and Technology, ICHVET 2019*, 2019, pp. 1–6, doi: 10.1109/ICHVET.2019.8724129.
- [7] C. Zhang, H. Xing, P. Li, C. Li, D. Lv, and S. Yang, “An experimental study of the failure mode of ZnO varistors under multiple lightning strokes,” *Electron.*, vol. 8, no. 2, 2019, doi: 10.3390/electronics8020172.
- [8] A. Zahedi, “Effect of dry band on performance of uhv surge arrester and leakage current monitoring, using new developed model,” in *Proceedings of the 4th International Conference on Properties and Applications of Dielectric Materials*, 1994, vol. 2, pp. 880–883, doi: 10.1109/icpadm.1994.414152.
- [9] M. R. Aghaebrahimi, M. Ghayedi, R. Shariatinasab, and R. Gholami, “A more uniform electric field distribution on surge arresters through the optimal design of spacer and fiber glass layer,” *Res. J. Appl. Sci. Eng. Technol.*, vol. 5, no. 13, pp. 3604–3609, 2013, doi: 10.19026/rjaset.5.4496.

## References

- [10] M. Kanya Kumari, R. S. Shivakumara Aradhya, B. Rajaiyya, and S. Kondalarao, "Design of grading ring for 624KV gapless zinc oxide surge arrester," *Proc. IEEE Int. Conf. Prop. Appl. Dielectr. Mater.*, 2012, doi: 10.1109/ICPADM.2012.6318998.
- [11] U. Kumar and V. Mogaveera, "Voltage distribution studies on ZnO arresters," *IEE Proc. Gener. Transm. Distrib.*, vol. 149, no. 4, pp. 457–462, 2002, doi: 10.1049/ip-gtd:20020346.
- [12] *INTERNATIONAL STANDARD IEC 60099-4; Surge arresters –Part4: Metal-oxide surge arresters without gaps for a.c. systems*, no. Second edition. International Electrotechnical Commission (IEC), 2004.
- [13] M. Khodsuz and M. Mirzaie, "Analysis of grading ring design parameters and heat sink numbers effect on voltage distribution and leakage current in metal oxide surge arrester," *Iran. J. Electr. Electron. Eng.*, vol. 10, no. 2, pp. 152–158, 2014.
- [14] C. Zhang, J. J. Kester, C. W. Daley, and S. J. Rigby, "Electric field analysis of high voltage apparatus using finite element method," 2010. doi: 10.1109/CEIDP.2010.5723955.
- [15] M. M. Kanubhai, "Analysis of Surge Arrester using FEM," *Int. J. Adv. Eng. Res. Dev.*, vol. 2, no. 5, pp. 1011–1016, 2015.
- [16] J. He, J. Hu, S. Gu, B. Zhang, and R. Zeng, "Analysis and improvement of potential distribution of 1000-kV ultra-high-voltage metal-oxide arrester," *IEEE Trans. Power Deliv.*, vol. 24, no. 3, pp. 1225–1233, 2009, doi: 10.1109/TPWRD.2009.2014034.
- [17] B. Vahidi, R. Shariati, N. J. S. Moghani, and K. Raahemifar, "Effects of Grading Rings and Spacers on Potential Distribution of ZnO Arrester," in *WSEAS Proceeding of International Conference on Power Systems and Electromagnetic Compatibility, Izmir, Turkey*, 2004, pp. 4–6.
- [18] J. He, R. Zeng, and S. Chen, "Potential Distribution Analysis of Suspended-Type Metal-Oxide Surge Arresters," *IEEE Trans. Power Deliv.*, vol. 18, no. 4, pp. 1214–1220, 2003.
- [19] A. Dlamini, P. Bokoro, and W. Doorsamy, "The effect of thermal transient on the leakage current of metal oxide arresters," *2020 Int. SAUPEC/RobMech/PRASA Conf. SAUPEC/RobMech/PRASA 2020*, pp. 4–8, 2020, doi:

## References

- 10.1109/SAUPEC/RobMech/PRASA48453.2020.9040952.
- [20] M. M. S. SERVIN, “Etude du Comportement Electrique et Thermique de Parafoudres à ZnO,” PHD thesis, ECOLE CENTRALE DE LYON, 1988.
- [21] J. He, R. Zeng, S. Chen, and Y. Tu, “Thermal characteristics of high voltage whole-solid-insulated polymeric ZnO surge arrester,” *IEEE Trans. Power Deliv.*, vol. 18, no. 4, pp. 1221–1227, 2003, doi: 10.1109/TPWRD.2003.817492.
- [22] A. F. Andrade, E. G. Costa, J. M. B. Fernandes, H. M. M. Alves, and C. R. C. Amorim Filho, “Thermal behaviour analysis in a porcelain-housed ZnO surge arrester by computer simulations and thermography,” *High Voltage-IET*, vol. 4, no. 3, pp. 173–177, 2019, doi: 10.1049/hve.2019.0048.
- [23] Y. Spack-Leigsnering, E. Gjonaj, H. De Gersem, T. Weiland, M. Giessel, and V. Hinrichsen, “Multi-rate time integration for coupled electrical and thermal modeling of surge arresters,” in *Proceedings of the 2015 International Conference on Electromagnetics in Advanced Applications, ICEAA 2015*, 2015, no. 1, pp. 264–267, doi: 10.1109/ICEAA.2015.7297116.
- [24] F. Denz, “Modeling and Simulation of Varistors,” PDH thesis, Technical University of Darmstadt, 2014.
- [25] J. He, J. Lin, W. Liu, H. Wang, Y. Liao, and S. Li, “Structure-dominated failure of surge arresters by successive impulses,” *IEEE Trans. Power Deliv.*, vol. 32, no. 4, pp. 1907–1914, 2017, doi: 10.1109/TPWRD.2016.2597191.
- [26] J. L. He and J. Hu, “Discussions on nonuniformity of energy absorption capabilities of ZnO varistors,” *IEEE Trans. Power Deliv.*, vol. 22, no. 3, pp. 1523–1532, 2007, doi: 10.1109/TPWRD.2007.899801.
- [27] V. Hinrichsen and M. N. Tuzcek, “Surge arresters for insulation coordination in UHV power systems-related problems and solutions,” *Elektrotechnik und Informationstechnik*, vol. 129, no. 5, pp. 326–331, 2012, doi: 10.1007/s00502-012-0032-1.
- [28] V. Hinrichsen, *Metal-Oxide Surge Arresters in High-Voltage Power Systems-Fundamentals*, 3rd editio. Berlin, Germany: Siemens AG, 2012.
- [29] B. Johnnerfelt, M. Mobedjina, and L. Stenstrom, “Design and Testing of Polymer-

## References

- Housed Surge Arresters,” in *the GCC CIGRÉ 9th Symposium., Abu Dhabi, October 28-29, 1998*, no. October 28-29, pp. 1–19.
- [30] K. Steinfeld, R. Göhler, and A. Largaespada Fredersdorff, “Rating and design of metal-oxide surge arresters for high voltage AC systems,” *Proceedings. Int. Conf. Power Syst. Technol.*, vol. 3, pp. 1416–1421, 2002, doi: 10.1109/ICPST.2002.1067763.
- [31] Working Group-A3.17, “MO Surge Arresters Stresses and Test Procedures,” *Cigré technical brochure n°544*, no. August. pp. 1–148, 2013.
- [32] Siemens, “Surge Arrester Design Comparison: Tube and Cage Designs versus Wrap Design.” Siemens AG, Power Transmission and Distribution, Berlin, Germany., pp. 1–4.
- [33] kai Steinfeld, “Design of MO Surge Arresters with Polymeric Housings, High Voltage Surge Arrester.” Siemens, Power Transmission and Distribution., pp. 1–14, 2004.
- [34] TOSHIBA, “Gas Insulated Surge Arresters.” TOSHIBA ENERGY SYSTEMS & SOLUTIONS CORPORATION, pp. 1–11, 2009.
- [35] Novizon and Z. Abdul-Malek, “Electrical and temperature correlation to monitor fault condition of ZnO surge arrester,” in *Proceedings of 3rd International Conference on Information Technology, Computer, and Electrical Engineering(ICITACEE) Oct 19-21st, Semarang, Indonesia, 2016*, pp. 182–186, doi: 10.1109/ICITACEE.2016.7892436.
- [36] P. N. Bokoro, “Degradation Analysis of Metal Oxide Varistors under Harmonic Distortion Conditions,” doctoral thesis, University of the Witwatersrand, Johannesburg, 2016.
- [37] A. BAYADI, “Contribution à l’étude des performances des parafoudres à base d’oxyde de zinc soumis à des contraintes transitoires rapides dans les systèmes électriques,” thèse de doctorat, Université FERHAT Abbas Sétif, 2005.
- [38] E. T. Wanderley Neto, E. G. da Costa, and M. J. A. Maia, “Artificial neural networks used for ZnO arresters diagnosis,” *IEEE Trans. Power Deliv.*, vol. 24, no. 3, pp. 1390–1395, 2009, doi: 10.1109/TPWRD.2009.2013402.

## References

- [39] N. A. A. Latiff, H. A. Illias, A. H. A. Bakar, and S. Z. A. Dabbak, "Measurement and modelling of leakage current behaviour in ZnO surge arresters under various applied voltage amplitudes and pollution conditions," *Energies*, vol. 11, no. 4, 2018, doi: 10.3390/en11040875.
- [40] Z. Abdul-Malek, A. H. Khavari, C. L. Wooi, M. Moradi, and A. Naderipour, "A review of modeling ageing behavior and condition monitoring of zinc Oxide Surge Arrester," in *2015 IEEE Student Conference on Research and Development, SCORED 2015*, 2015, pp. 733–738, doi: 10.1109/SCORED.2015.7449435.
- [41] M. Bartkowiak, M. G. Comber, and G. D. Mahan, "Influence of Nonuniformity of ZnO Varistors on Their Energy Absorption Capability," *IEEE Trans. Power Deliv.*, vol. 16, no. 04, pp. 591–598, 2001, doi: 10.1109/MPER.2001.4311480.
- [42] S. T. Li, J. Q. He, J. J. Lin, H. Wang, W. F. Liu, and Y. L. Liao, "Electrical-Thermal Failure of Metal-Oxide Arrester by Successive Impulses," *IEEE Trans. Power Deliv.*, vol. 31, no. 6, pp. 2538–2545, 2016, doi: 10.1109/TPWRD.2015.2506785.
- [43] M. Bartkowiak, M. G. Comber, and G. D. Mahan, "Failure modes and energy absorption capability of ZnO varistors," *IEEE Trans. Power Deliv.*, vol. 14, no. 1, pp. 152–162, 1999, doi: 10.1109/61.736708.
- [44] K. Feser, "Behaviour of Zinc Oxide Surge Arresters Under Pollution," *IEFE Trans. Power Deliv.*, vol. 6, no. 2, pp. 688–695, 1991.
- [45] M. Khodsuz and M. Mirzaie, "Evaluation of ultraviolet ageing, pollution and varistor degradation effects on harmonic contents of surge arrester leakage current," *IET Sci. Meas. Technol.*, vol. 9, no. 8, pp. 979–986, 2015, doi: 10.1049/iet-smt.2014.0372.
- [46] K. Chrzan, Z. Pohl, S. Grzybowski, and W. Köhler, "Pollution performance of 110 kV metal oxide arresters," *IEEE Trans. Power Deliv.*, vol. 12, no. 2, pp. 728–733, 1997, doi: 10.1109/61.584358.
- [47] R. P. Singh and T. V. P. Singh, "Influence of pollution on the performance of metal oxide surge arresters," in *Canadian Conference on Electrical and Computer Engineering*, 2002, pp. 224–229, doi: 10.1109/CCECE.2002.1015206.
- [48] I. A. Metwally, "Performance of distribution-class surge arresters under dry and artificial pollution conditions," *Electr. Eng.*, vol. 93, no. 1, pp. 55–62, 2011, doi:

## References

- 10.1007/s00202-010-0193-z.
- [49] F. Tighilt, A. Bayadi, and A. M. Haddad, "Voltage distribution on ZnO polymeric arrester under pollution conditions," in *45th International Universities Power Engineering Conference UPEC2010*, 2010, pp. 1–5.
- [50] N. Alti and A. BAYADI, "Behaviour of the Polymeric Surge Arrester under Pollution taking into account the Presence of Dry Bands," in *THE 9th INTERNATIONAL CONFERENCE ON ELECTRICAL ENGINEERING And FIRST WORKSHOP ON ROBOTICS AND CONTROLS, CEE 2016, BATNA*, 2016, pp. 1–5.
- [51] W. Thipprasert and E. Chaidee, "Metal Oxide Surge Arresters Modelling in Temporary Overvoltage Conditions," *Int. J. Electron. Electr. Eng.*, vol. 4, no. 2, pp. 146–150, 2016, doi: 10.18178/ijeee.4.2.146-150.
- [52] K. L. Wong, "Electromagnetic emission based monitoring technique for polymer ZnO surge arresters," *IEEE Trans. Dielectr. Electr. Insul.*, vol. 13, no. 1, pp. 181–190, 2006, doi: 10.1109/TDEI.2006.1593416.
- [53] K. L. Chrzan and J. Gielniak, "Voltage distribution along metal oxide surge arresters," in *XIIIth International Symposium on High Voltage Engineering, Netherlands*, 2003, pp. 1–4.
- [54] A. Nadjim and A. Bayadi, "Behaviour of the Metal Oxide Surge Arrester under Pollution," in *9th National Conference on High Voltage, CNHT 2013, Laghouat*, 2013, pp. 1–5.
- [55] M. Khodsuz, M. Mirzaie, and S. Seyyedbarzegar, "Metal oxide surge arrester condition monitoring based on analysis of leakage current components," *Int. J. Electr. Power Energy Syst.*, vol. 66, pp. 188–193, 2015, doi: 10.1016/j.ijepes.2014.10.052.
- [56] M. Khodsuz and M. Mirzaie, "Harmonics ratios of resistive leakage current as metal oxide surge arresters diagnostic tools," *MEASUREMENT*, vol. 70, pp. 148–155, 2015, doi: 10.1016/j.measurement.2015.03.048.
- [57] Z. Xu, L. Zhao, A. Ding, and F. Lü, "A Current Orthogonality Method to Extract Resistive Leakage Current of MOSA," *IEEE Trans. Power Deliv.*, vol. 28, no. 1, pp. 93–101, 2013.
- [58] C. M. V. A. C. A and S. L Ekonomou, I F Gonos I A, "Measurement of the resistive

## References

- leakage current in surge arresters under artificial rain test and impulse voltage subjection,” *IET Sci. Meas. Technol.*, vol. 3, no. 03, pp. 256–262, 2009, doi: 10.1049/iet-smt.
- [59] K. C. Agrawal, “Chapter 18: Surge arresters: applications and selection,” in *Electrical Power Engineering Reference & Applications Handbook*, 2007, pp. 681–719.
- [60] K. Mokhtari, M. C. A. Mirzaie, and M. Shahabi, “Leakage Current Analysis of Polymer and Porcelain Housed Metal Oxide Surge Arresters in Humid Ambient Conditions,” *Iran. J. Electr. Electron. Eng.*, vol. 11, no. 1, pp. 79–85, 2015.
- [61] M. Khodsuz and M. Mirzaie, “A Modified Time-Delay Addition Method to Extract Resistive Leakage Current of MOSA,” *J. Inst. Eng. Ser. B*, vol. 97, no. 4, pp. 445–451, 2016, doi: 10.1007/s40031-015-0207-3.
- [62] C. Heinrich and V. Hinrichsen, “Diagnostics and Monitoring of Metal-Oxide Surge Arresters in High-Voltage Networks — Comparison of Existing and Newly Developed Procedures,” *IEEE Trans. Power Deliv.*, vol. 16, no. 1, pp. 138–143, 2001.
- [63] Z. Abdul-malek, “A New Method to Extract the Resistive Component of the Metal Oxide Surge Arrester Leakage Current,” in *2nd IEEE International Conference on Power and Energy (PECon 08), December 1-3, 2008, Johor Baharu, Malaysia*, 2008, pp. 399–402.
- [64] D. A. Silva, R. C. De Jesus, and J. Pissolato, “Partial discharge activity in distribution MOSAs due to internal moisture,” in *2015 International Symposium on Lightning Protection (XIII SIPDA), Balneário Camboriú, Brazil*, pp. 94–98.
- [65] W. A. M. Ursine, J. L. Silvino, L. G. Fonseca, and R. M. De Andrade, “Metal- Oxide Surge Arrester ’ s Leakage Current Analysis and Thermography,” in *2013 International Symposium on Lightning Protection (XII SIPDA), Belo Horizonte, , Brazil.*, pp. 297–303.
- [66] S. Likitha, M. Kanyakumari, J. P. P, S. A. R. S, and N. Vasudev, “Estimation of Critical Resistive Leakage Current of Polymer Housed ZnO Surge Arrester by Electro-Thermal Modelling,” *J. Electr. Syst. Inf. Technol.*, vol. 5, no. 3, 2016, doi: 10.1016/j.jesit.2016.12.010.
- [67] J. Lu, P. Xie, Z. Fang, and J. Hu, “Electro-Thermal Modeling of Metal-Oxide Arrester

## References

- under Power Frequency Applied Voltages,” *Energies*, vol. 11, no. 6, pp. 1–13, 2018, doi: 10.3390/en11061610.
- [68] M. V. Lat, “Thermal properties of metal oxide surge arresters,” *IEEE Trans. Power Appar. Syst.*, vol. PAS-102, no. 7, pp. 2194–2202, 1983, doi: 10.1109/TPAS.1983.318207.
- [69] M. Ali, M. Sanaye-pasand, S. Member, and S. Bahari, “Preventing Transformer Energizing Resonant Overvoltages Using Surge Arrester Temperature Rise Index and Controlled Closing Method,” *IEEE Trans. Power Deliv.*, vol. 28, no. 2, pp. 998–1006, 2013.
- [70] S. M. Seyyedbarzegar and M. Mirzaie, “Thermal balance diagram modelling of surge arrester for thermal stability analysis considering ZnO varistor degradation effect,” *IET Gener. Transm. Distrib.*, vol. 10, no. 07, pp. 1570–1581, 2016, doi: 10.1049/iet-gtd.2015.0728.
- [71] S. Tominaga, Y. Shibuya, Y. Fujiwara, M. Imataki, and T. Nitta, “Stability and Long Term Degradation of Metal Oxide Surge Arresters,” *IEEE Trans. Power Appar. Syst.*, vol. PAS-99, no. 4, pp. 1548–1556, 1980.
- [72] K. G. Schmidt, *VDI Heat Atlas*, 2nd Editio. Berlin: Springer-Verlag Berlin Heidelberg, 2010.
- [73] W. M. Rohsenow and J. R. Hartnett, *Handbook of heat transfer*, 3rd editio. The McGraw-Hill Companies, 1998.
- [74] S. M. Seyyedbarzegar and M. Mirzaie, “Heat transfer analysis of metal oxide surge arrester under power frequency applied voltage,” *Energy*, vol. 93, pp. 141–153, 2015, doi: 10.1016/j.energy.2015.09.031.
- [75] A. Petit, X. D. Do, and G. St-Jean, “An experimental method to determine the electro-thermal model parameters of metal oxide surge arresters,” *IEEE Trans. Power Deliv.*, vol. 6, no. 2, pp. 715–721, 1991, doi: 10.1109/61.131131.
- [76] J. C. Juan F. Lara, Montenegro, “identification-of-electrothermal-model-parameters forMetal - Oxide Surge Arresters Using Auto Regressive Technics,” in *Proceedings of the Twenty-Seventh Southeastern Symposium on System Theory, SSST 1995.*, 1995, pp. 2–6.

## References

- [77] I. Vernica, P. T. Jensen, H. Wang, F. Iannuzzo, S. Otto, and F. Blaabjerg, "Loss and thermal modeling of metal oxide varistors (MOV) under standard current surge mission profile," in *2019 IEEE Energy Conversion Congress and Exposition, ECCE 2019, Baltimore, MD, USA, 2019*, pp. 7113–7117, doi: 10.1109/ECCE.2019.8913287.
- [78] G. Alame, N., Melik, "Axial Voltage and Gradient distribution of Metal Oxide Surge arresters," in *Proceedings of the 3rd International Conference on Properties and Applications of Dielectric Materials. Tokyo, Japan., 1991*, pp. 1149–1151.
- [79] H. Akkal, C. Volat, and M. Farzaneh, "Improving Electrical Performance of EHV Post Station Insulators under Severe Icing Conditions Using Modified Grading Rings," *IEEE Trans. Dielectr. Electr. Insul.*, vol. 20, no. 1, pp. 221–228, 2013.
- [80] D. Schmidhäusler, S. Schöps, and M. Clemens, "Reduction of Linear Subdomains for Non-Linear Electro-Quasistatic Field Simulations," *IEEE Trans. Magn.*, vol. 49, no. 5, pp. 1669–1672, 2013.
- [81] H. Terrab and A. Kara, "Parameters design optimization of 230 kV corona ring based on electric field analysis and response surface methodology," *Electr. Power Syst. Res.*, vol. 163, pp. 782–788, 2018, doi: 10.1016/j.epsr.2017.06.002.
- [82] J. Li, Z. Peng, and X. Yang, "Potential calculation and grading ring design for ceramic insulators in 1000 kV UHV substations," *IEEE Trans. Dielectr. Electr. Insul.*, vol. 19, no. 2, pp. 723–732, 2012, doi: 10.1109/TDEI.2012.6180268.
- [83] E. Akbari, M. Mirzaie, M. B. Asadpoor, and A. Rahimnejad, "Effects of disc insulator type and corona ring on electric field and voltage distribution over 230-kV insulator string by numerical method," *Iran. J. Electr. Electron. Eng.*, vol. 9, no. 1, pp. 58–66, 2013.
- [84] D. Nie, H. Zhang, Z. Chen, X. Shen, and Z. Du, "Optimization design of grading ring and electrical field analysis of 800 kV UHVDC Wall wall bushing," *IEEE Trans. Dielectr. Electr. Insul.*, vol. 20, no. 4, pp. 1361–1368, 2013, doi: 10.1109/TDEI.2013.6571457.
- [85] S. Zhang, Z. Peng, L. Peng, and H. Wang, "Optimization of corona ring structure for UHV composite insulator using finite element method and PSO algorithm," in *2013 IEEE International Conference on Solid Dielectrics(ICSD), Bologna, Italy, June 30 –*

## References

- July 4, 2013, pp. 210–213, doi: 10.1109/ICSD.2013.6619660.
- [86] B. M’Hamdi, M. Tegar, and A. Mekhaldi, “Optimal design of corona ring on HV composite insulator using PSO approach with dynamic population size,” *IEEE Trans. Dielectr. Electr. Insul.*, vol. 23, no. 2, pp. 1048–1057, 2016, doi: 10.1109/TDEI.2015.005383.
- [87] “High voltage surge arresters buyer’s guide,” *ABB, Sweden, edition 14*. pp. 1–126, 2018.
- [88] “Surge Arresters IEC Line Discharge Classes 2, 3, 4 & 5,” *Hubbell power systems, 204*. AIKEN, SC: OHIO BRASS, pp. 1–48, 2015.
- [89] “High-voltage surge arresters, Product guide,” *siemens.com/energy/arrester*. Siemens AG, Berlin, Germany., pp. 1–112, 2018.
- [90] A. Patrick, “Sécurité électrique - Habilitation,” <https://sitelec.org/cours/abati/habilitation.htm>, (2001), Accessed August 20, 2019. .
- [91] N. Alti, A. Bayadi, and K. Belhouchet, “Grading ring parameters optimization for 220 kV metal-oxide arrester using 3D-FEM method and bat algorithm,” *IET Sci Meas Technol*, vol. 15, no. 1, pp. 14–24, 2021, doi: 10.1049/smt2.12002.
- [92] H. A. Illias, S. Abd Halim, A. H. Abu Bakar, and H. Mokhlis, “Determination of surge arrester discharge energy using finite element analysis method,” *IET Sci. Meas. Technol.*, vol. 9, no. 6, pp. 693–701, 2015, doi: 10.1049/iet-smt.2014.0240.
- [93] K. Krishnaiah and P. Shahabudeen, *Applied Design of Experiments and TAGUCHI METHODS*. PHI Learning Private Limited, New Delhi, 2012.
- [94] S. Athreya and Y. D. Venkatesh, “Application Of Taguchi Method For Optimization Of Process Parameters In Improving The Surface Roughness Of Lathe Facing Operation,” *Int. Ref. J. Eng. Sci.*, vol. 1, no. 3, pp. 13–19, 2012.
- [95] A. Saravanakumar, S. C. Karthikeyan, B. Dhamotharan, and V. G. Kumar, “Optimization of CNC Turning Parameters on Aluminum Alloy 6063 using TaguchiRobust Design,” *Mater. Today Proc.*, vol. 5, no. 2, pp. 8290–8298, 2018, doi: 10.1016/j.matpr.2017.11.520.
- [96] K. I. Yaakob, M. Ishak, M. M. Quazi, and M. N. M. Salleh, “Optimizing the pulse wave mode low power fibre laser welding parameters of 22Mnb5 boron steel using

## References

- response surface methodology,” *MEASUREMENT*, vol. 135, pp. 452–466, 2019, doi: 10.1016/j.measurement.2018.10.035.
- [97] X. S. Yang, “A new metaheuristic Bat-inspired Algorithm (NISCO 2010),” *Springer-Verlag*, vol. 284, pp. 65–74, 2010, doi: 10.1007/978-3-642-12538-6\_6.
- [98] A. Chakri, R. Khelif, M. Benouaret, and X. S. Yang, “New directional bat algorithm for continuous optimization problems,” *Expert Syst. Appl.*, vol. 69, no. 1, pp. 159–175, 2017, doi: 10.1016/j.eswa.2016.10.050.
- [99] W. Kongkaew, “Bat algorithm in discrete optimization: A review of recent applications,” *Songklanakarin J. Sci. Technol.*, vol. 39, no. 5, pp. 641–650, 2017, doi: 10.14456/sjst-psu.2017.79.
- [100] X. S. Yang and A. H. Gandomi, “Bat algorithm: A novel approach for global engineering optimization,” *Eng. Comput.*, vol. 29, no. 5, pp. 464–483, 2012, doi: 10.1108/02644401211235834.
- [101] S. Yilmaz and E. U. Kucuksille, “Improved Bat Algorithm (IBA) on Continuous Optimization Problems,” *Lect. Notes Softw. Eng.*, vol. 1, no. 3, pp. 279–283, 2013, doi: 10.7763/lmse.2013.v1.61.
- [102] L. A. M. D’Angelo, Y. Späck-Leigsnering, and H. De Gerssem, “Electroquasistatic quasi-3D finite element simulation of a graded surge arrester,” *Int. J. Numer. Model. Electron. Networks, Devices Fields*, vol. 33, no. 5, pp. 1–13, 2020, doi: 10.1002/jnm.2575.
- [103] M. Stosur, M. Szewczyk, K. Sowa, P. Dawidowski, and P. Balcerek, “Thermal behaviour analyses of gas-insulated switchgear compartment using thermal network method,” *IET Gener. Transm. Distrib.*, vol. 10, no. 12, pp. 2833–2841, 2016, doi: 10.1049/iet-gtd.2015.0489.

## ملخص:

يهدف الجزء الأول من هذه الرسالة إلى تحسين توزيع الجهد والمجال الكهربائي على طول مانعة الصواعق البوليميرية 220 كيلو فولط عن طريق تحسين تصميم حلقة تدرج المجال الكهربائي. تم اختيار طريقة مدمجة تعتمد على طريقة العناصر المنتهية ثلاثية الأبعاد وتصميم تاجوتشي من أجل الحصول على دالة الهدف. يتم تحقيق التصميم الأمثل لحلقة تدرج المجال الكهربائي من خلال تقليل المجال الكهربائي على طول العمود النشط للمتغيرات باستخدام عدد أقل من عمليات المحاكاة بناءً على تصميم تاجوتشي وخوارزمية الخفايش. باستخدام التصميم الأمثل للحلقة الواحدة، يتم تقليل المجال الكهربائي بنسبة 42% في الجزء العلوي من مانعة الصواعق 220 كيلو فولط. بعد ذلك، تم اقتراح تركيب حلقة إضافية في الجزء العلوي من مانعة الصواعق من أجل الحصول على توزيع أفضل للجهد والمجال الكهربائي على طول العمود النشط. هذه الحلقة الإضافية المقترحة لها بعد هندسي كبير مقارنة بالحلقة الأولى. تظهر نتائج المحاكاة أنه باستخدام التصميم الأمثل للحلقات المزدوجة، يمكن جعل توزيع الجهد منتظماً قدر الإمكان ويتم تقليل المجال الكهربائي بنسبة 53% لتجنب تلف المتغيرات.

يتعلق الجزء الثاني من الأطروحة بالنمذجة الكهرو حرارية لموانع الصواعق أكسيد المعادن التي تسمح بالحصول على تغير درجة حرارة مانع الصواعق ZnO المدروس. لهذا الغرض، تم اشتقاق نموذج كهربائي حراري مكون من مصادر الحرارة، السعات، والمقاومات. تم تنفيذ الدائرة المكافئة لهذا النموذج في برنامج ATP / EMTP من أجل محاكاة درجات الحرارة الداخلية للمتغيرات ودرجات الحرارة الخارجية لغللاف مانع الصواعق، وتم الحصول على نتائج مرضية. سيسمح لنا التقييم المناسب لدرجة الحرارة بمراقبة حالة مانعة الصواعق وكذلك تجنب فشلها.

**كلمات مفتاحية:** مانعة الصواعق البوليميرية، حلقة تدرج المجال الكهربائي، المجال الكهربائي، طريقة العناصر المنتهية ثلاثية الأبعاد، تصميم تاجوتشي، خوارزمية الخفايش، النمذجة الكهروحرارية، ATP / EMTP، درجة الحرارة.

## **Abstract:**

The first part of this thesis is aimed to improve the distribution of the potential and the electric field along a 220 kV polymeric surge arrester by optimizing the design of the grading ring. A combined method based on 3D-FEM and Taguchi design is opted in order to obtain the objective function. The optimal design of grading ring is achieved by minimizing the electric field along the active column of varistors using a reduced number of simulations based on the Taguchi design and a bat algorithm. By the use of an optimal design of the single ring, the electric field is reduced by 42% in the top of the 220 kV metal oxide surge arrester. Then, it was proposed to install an additional ring at the top of the metal oxide surge arrester in order to obtain a better distribution of the potential and the electric field along the active column. This proposed additional ring has a large geometric dimension compared to the first ring. Simulation results show that using an optimal design of double rings, the potential distribution can be made as uniform as possible and the electric field is reduced by 53% to avoid damage of varistors.

The second part of the thesis concerns the electro-thermal modeling of metal oxide surge arresters which allows the temperature variation of the studied ZnO surge arrester. For this purpose, an electro-thermal model formed of heat source, capacitances, and resistances was derived. The equivalent circuit of this model has been implemented in the ATP / EMTP software in order to simulate the internal temperatures of the varistors and the external temperatures of the surge arrester housing, and satisfactory results have been obtained. The suitable evaluation of the temperature would allow us to monitor the condition of the surge arrester as well as to avoid its failure.

**Key Words:** Polymeric surge arrester, grading ring, electric field, 3D FEM, Taguchi design, Bat algorithm, electro-thermal modeling, ATP / EMTP, temperature.

## **Résumé:**

La première partie de cette thèse vise à améliorer la distribution du potentiel et du champ électrique le long d'un parafoudre 220 kV en polymère en optimisant la conception de l'anneau de garde. Une méthode combinée basée sur 3D-FEM et la conception de Taguchi est choisie afin d'obtenir la fonction objective. La conception optimale de l'anneau de garde est obtenue en minimisant le champ électrique le long de la colonne active de varistances en utilisant un nombre réduit de simulations basées sur la conception de Taguchi et un algorithme de chauve-souris. Par l'utilisation d'une conception optimale de l'anneau unique, le champ électrique est réduit de 42% dans la partie supérieure du parafoudre à oxyde métallique 220 kV. Ensuite, il a été proposé d'installer un anneau supplémentaire en haut du parafoudre à oxyde métallique afin d'obtenir une meilleure distribution du potentiel et du champ électrique le long de la colonne active. Cet anneau supplémentaire proposé a une grande dimension géométrique par rapport au premier anneau. Les résultats de simulation montrent qu'en utilisant une conception optimale de doubles anneaux, la distribution du potentiel peut être rendue aussi uniforme que possible et le champ électrique est réduit de 53% pour éviter d'endommager les varistances.

La deuxième partie de la thèse concerne la modélisation électrothermique des parafoudres à oxyde métallique qui permet d'obtenir la variation de la température du parafoudre ZnO étudié. À cet effet, un modèle électrothermique formé de source de chaleur, de capacités, et de résistances a été dérivé. Le circuit équivalent de ce modèle a été implémenté dans le logiciel ATP / EMTP afin de simuler les températures internes des varistances et les températures externes de l'enveloppe du parafoudre, et des résultats satisfaisants ont été obtenus. L'évaluation convenable de la température nous permettrait de surveiller l'état du parafoudre et d'éviter sa défaillance.

**Mots clés:** Parafoudre en polymère, anneau de garde, champ électrique, 3D-FEM, conception de Taguchi, algorithme de Bat, modélisation électrothermique, ATP / EMTP, température.